Rate-dependent Buckling and Creasing Mechanics of Elastic and Viscoelastic Films under Compression

by

Xianheng Guan

Bachelor of Science in Mechanical Engineering,
University of Michigan - Shanghai Jiao Tong University Joint Institute, 2014

Master of Science in Mechanical Engineering
University of Pittsburgh, 2016

Submitted to the Graduate Faculty of the

Swanson School of Engineering in partial fulfillment

of the requirements for the degree of

Doctor of Philosophy

University of Pittsburgh

2022

UNIVERSITY OF PITTSBURGH

SWANSON SCHOOL OF ENGINEERING

This dissertation was presented

by

Xianheng Guan

It was defended on

May 9, 2022

and approved by

Qihan Liu, PhD, Assistant Professor, Department of Mechanical Engineering and Material Science

Patrick Smolinski, PhD, Associate Professor, Department of Mechanical Engineering and Material Science

Spandan Maiti, PhD, Assistant Professor, Department of Bioengineering

Leu Paul, PhD, Associate Professor, Department of Industrial Engineering

Dissertation Director: Sachin Velankar, PhD, Professor, Department of Chemical & Petroleum Engineering, Department of Mechanical Engineering and Materials Science

Rate-dependent Buckling and Creasing Mechanics of Elastic and Viscoelastic Films under Compression

Xianheng Guan, PhD

University of Pittsburgh, 2022

This thesis examines two situations in the buckling of thin films subjected to compression: the buckling of elastic thin films attached to viscous substrates, and the free-surface creasing of a viscoelastic liquid.

When a thin film on a layer viscous liquid is compressed steadily at a fixed rate, two distinct buckling modes are observed: roughly-sinusoidal, global wrinkling, and formation of highly-localized ridges well-separated by more-or-less flat regions. Although both buckling modes have been reported previously, there is no understanding of ridge localization. Further, the quantitative aspects of how parameters such as loading rate and liquid substrate thickness influence the buckling process are also unknown. With our experiments and simulations, ridge localization can be understood as buckling phenomenon starting with wrinkles emerging in the form of wave packets with a longer length scale modulation which is rate-dependent. The size of these wave packets captures the dependence of inter-ridge on the compression rate and the liquid layer thickness observed far from threshold in experiment and simulation. Further, the effects of end-relaxation on the buckling behavior for relatively short films were also examined by simulations.

It is well-known that the free surface of an elastic material develops sharp cusp-like creases when compressed beyond a certain critical strain. Here we examine a viscoelastic fluid under similar compression. Experiments show that a viscoelastic liquid undergoes a similar, but rate-

dependent, creasing instability such that the strain required for creasing increases as rate decreases. A model is developed wherein the creasing criterion known previously for neo-Hookean elastic solids is applied to the elastic portion of the deformation of a viscoelastic liquid. Using the upper-convected Maxwell model for viscoelasticity, we derive an analytical criterion for viscoelastic creasing which is in good agreement with experiments. It predicts that the strain for creasing increases with decreasing Weissenberg number, and creasing is not possible below a critical Weissenberg number.

Table of Contents

List of Figures

Acknowledgements

It is with great pride that I present my Ph.D. dissertation. When preparing for it, I have received a huge amount of support and assistance.

I would first like to thank my supervisor, Professor Sachin Velankar, whose continuous guidance and encouragement helped me a lot in these years. It would be impossible for me to complete this dissertation without your help. Your insightful idea and great passion for science will always guide me in the future.

I would like to thank Professor Qihan Liu, Professor Enrique Cerda and Professor Luka Pocivavsek for your relentless help and insight comments for research. I would also like to thank Dr. Nhung Nguyen for solving my research questions about simulations.

I would like to thank my colleagues Likhitha Reddipalli, Anantha Padmanabha Sarma and Eshwar Hamesh for your wonderful collaboration and nice experiments. Besides I would like to thank my colleagues Dylan Butler for your great help to build up experimental jigs and the user manual.

Finally, I would like to thank my parents, Chen Pinying and Guan Wei, for their encouragement and full support. Also, I would like to thank my friends/ future scholars, Luna Yang and Yuxin Wang in Pittsburgh for their encouragement.

1.0 Introduction

When a compressive load is applied on both ends of a short beam, the beam fails when the load applied is beyond the compressive yield strength. A long beam however buckles into a roughly sinusoidal deformed shape before failure occurs. The critical load to induce buckling, the critical bending moment, and the deformed shape of beam can be predicted by Euler column buckling theory[1-3]. A column under uniaxial compression buckles at the longest wavelength specified by constraints. Another simple example is compressing a piece of paper laying flat on smooth table by pushing on its ends. A sinusoidal-shape deformation with a single hump can be observed indicating that the wavelength has the longest possible value, which spans the two ends being pushed.

However, buckling becomes more complicated if the film is bonded to a compliant support. An example is the uniaxial compression of a thin film floating on the surface of liquid. The thin film still prefers to buckle at the longest wavelength if possible. However, the liquid layer prefers to maintain a flat surface due to gravity. Thus there is a competition between the elastic energy of the film and the gravitational potential energy of the liquid, and buckling occurs at a smaller length scale as compared with the buckling of an unsupported column. Specifically, the film develops numerous uniform wrinkles at a wavelength which is independent of the film length[4].

The buckling mechanics of thin films on compliant substrates has been studied widely in the recent years[5-16]. One well-studied case is the one from the previous paragraph: a thin film floating on a substrate buckles into different patterns under uniaxial compression. Distinct

buckling modes can be observed under various conditions. When the substrate is viscous liquid, which is of interest to Chapter 3 to 5, wrinkles are induced under uniaxial compression and turn into ridges with high amplitude when compressed more[10] (Fig. 1.1). When the substrate is inviscid rather than viscous, wrinkles and ridges can also be observed[11-13]. When film is floating on a spherical liquid drop and buckling is induced by tension[14,15], crumples appear as another form of localized buckling. When the substrate is elastic and soft, films also buckle into wrinkles and sometimes localized into high ridges or period-doubling wrinkles[5-9]. Films bonded to rigid elastic substrate can also buckle due to delamination. Buckling delamination and sliding-folding delamination can be observed under compression or thermal swelling[16] and creasing can also be observed if film and substrate are tightly bonded and have same material properties[17-27], which will be discussed in Chapter 6. Some of these buckling modes are shown in Fig 1.1 to Fig 1.4.

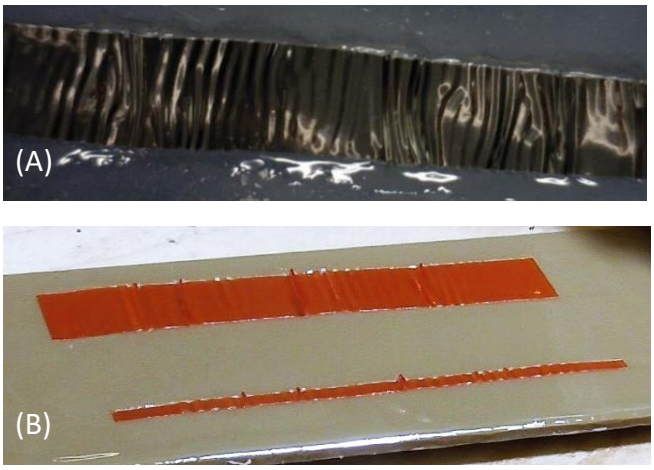

Figure 1.1: Buckling modes of film bonded on viscous liquid (A) wrinkles observed by Chatterjee[10] (B) localized ridges observed in crude hand experiments done by undergraduate researchers Anantha Sarma and Eshwar Hamesh in the Velankar research group.

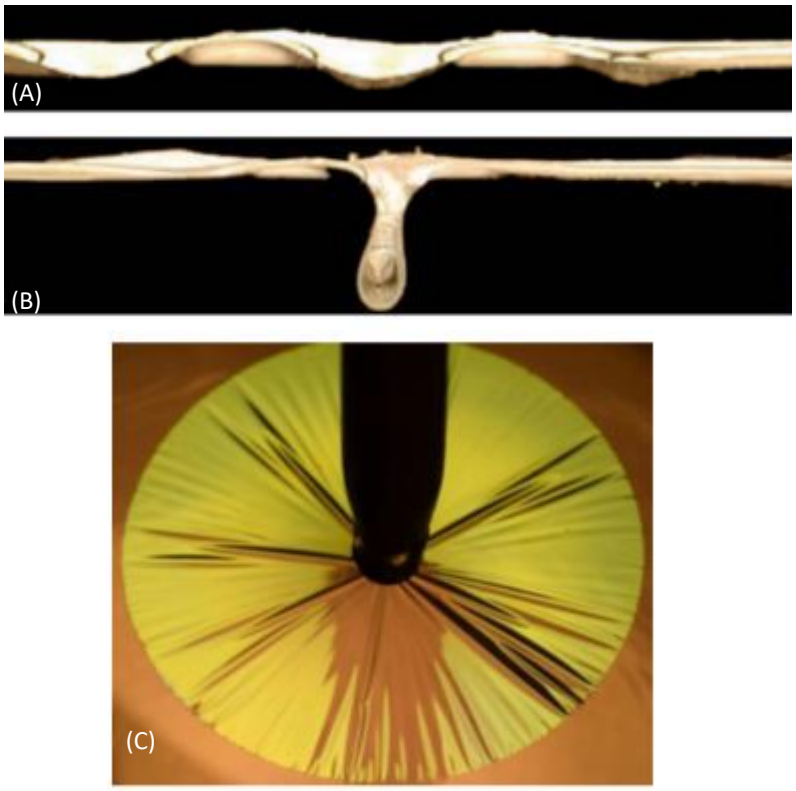

Figure 1.2: Buckling modes of film bonded on inviscid liquid[28] (A) wrinkles (B) folds (C) crumples[29]. Figure reproduced from citation 28 with permission from the Royal Society of Chemistry and figure reproduced from citation 29 with permission from American Physical Society.

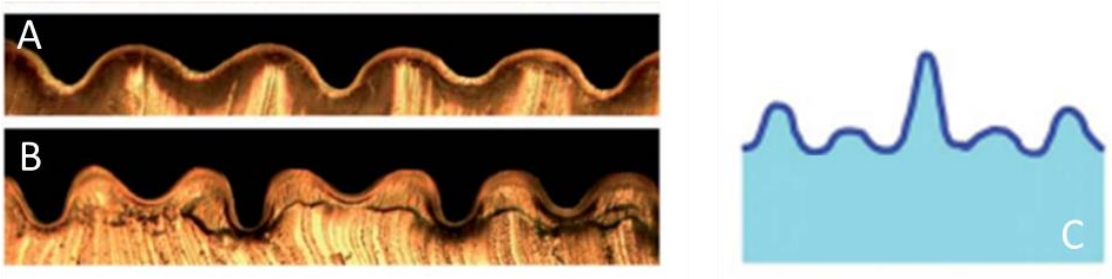

Figure 1.3: Buckling modes[28] of film bonded on soft elastic substrate (A) wrinkles (B) double-period wrinkles (C) ridges[30]. Figure reproduced from citation 28 and 30 with permission from the Royal Society of Chemistry.

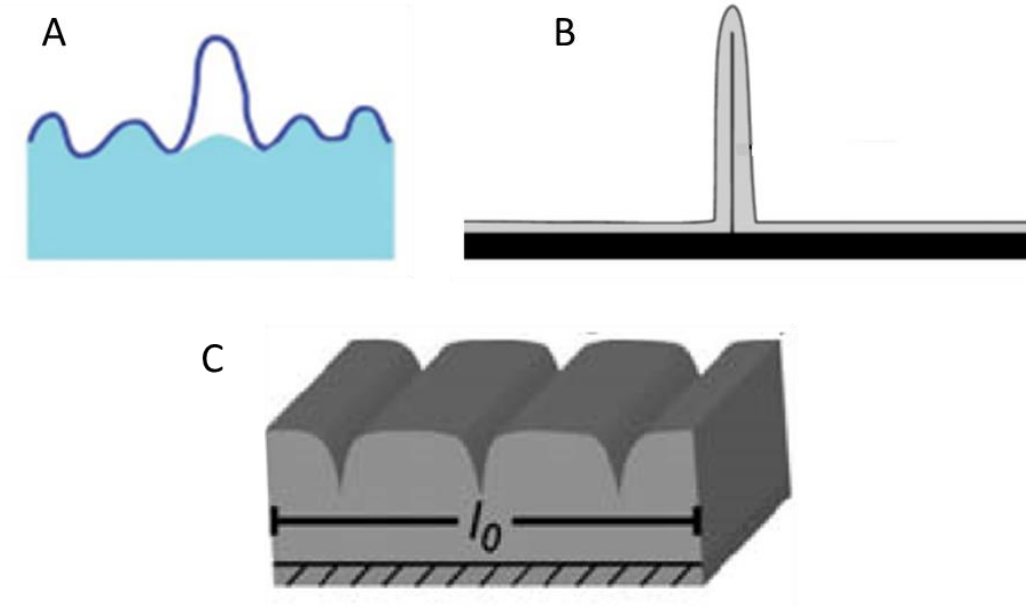

Figure 1.4: buckling modes of a film when a strain mismatch with respect to a substrate forces compressive stress in the film (A) delaminated buckles[30] (B) sliding-folding buckles[31] (C) creasing[22]. Figure reproduced from citation 10 with permission from American Chemical Society and Figure reproduced from citation 22 with permission from Royal Society of Chemistry.

1.1 Overview

This thesis includes two topics in the area of compression-induced instabilities. The first one is ridge localization of thin film on viscous liquid and the second one is about viscoelastic liquid creasing. Below I provide a brief overview of each of these topics.

1.1.1 Ridge localization of thin film on viscous liquid

The ridge localization of thin film on soft solid substrate or inviscid liquid are fully discussed in recent 20 years. However, ridge localization on viscous supports are rarely mentioned. To our knowledge, a previous paper published from our laboratory[10] is the only article that mentions ridge localization on viscous substrates. Yet, even that article focused on uniform wrinkling, and did not examine ridge formation in detail. Accordingly, there is no understanding of why ridges appear and the conditions under which they appear.

While ridge formation on elastic substrates can be understood based on energy minimization principles[28,32], viscous substrates dissipate energy, which makes the energy minimization method unavailable. Therefore we cannot understand ridge formation just based on existing literature on elastic and inviscid substrates. Thus, a central goal of this thesis was to conduct new experiments and simulations to get a deeper understanding of the underlying mechanisms. In Chapter 3, the experimental setup and result of film buckling mechanics will be discussed in detail. Simulation results and a more detailed analysis of film buckling mechanics will be introduced in Chapter 4 and 5. Specifically, Chapter 4 will focus on identifying the conditions under which films of finite length show wrinkles vs ridges, and Chapter 5 will then examine infinite-length conditions and obtain details of development of interridge distance and wavelength.

1.1.2 Viscoelastic creasing mechanics

It is well-known that an elastomeric material forms cusp-shaped, self-contacting buckles when compressed to a large extent[17-27,33]. Such buckles are called creases and understood as free

surface buckling instability. Past research has focused on understanding creasing in elastic systems. However, creases can also be observed on the surface of viscoelastic liquids when compressive strain is sufficiently high. However, as may be expected, such creasing is rate-dependent: a viscoelastic liquid will not crease under low-rate compression. This phenomenon has never been explored in the literature and not at all understood quantitatively. Chapter 6 describes the experiments and theory of viscoelastic creasing and identifies the conditions under which viscoelastic liquid under compression will creases at its free surface.

2.0 Background

In this chapter, I will review past research on buckling of thin films bonded to compliant surfaces as a background for Chapters 3, 4, and 5. The background literature on free surface creasing is reviewed in Chapter 6.

The buckling mechanics of thin films has been heavily studied in the recent 20 years. The most well-studied cases are that of a thin film floating on a liquid, or thin film bonded to a soft elastic substrate. Both situations buckle into different patterns under compression or thermal swelling[2,11-13,29,34-41]. Much of the research has focused on the evolution of buckling mode and give a prediction of wavelength, evolution of amplitude with strain, and changes in mode.

2.1 Buckling of thin films on viscous layer

The most well-studied cases are that of rectilinear compression of a thin elastic film floating on an inviscid liquid[42], or thin film bonded to a soft elastic substrate[5-9,32,34,42-45]. Both situations buckle into different patterns under compression or thermal swelling. Much of the research has focused on the evolution of buckling mode and give a prediction of wavelength, evolution of amplitude with strain, and changes in mode[7,34,42].

When a thin film floating on inviscid substrate is compressed, it first buckles into uniform and global wrinkles. If the compression increases, wrinkles might evolve to localized, high amplitude folds with nearly flat region among the folds. This process of evolution is called

wrinkle-to-fold transition[34,42,46]. Other methods to induce it has also been discussed by researchers, such as placing a drop on the film[14,47] or lifting the center of film[11-13]. Beyond wrinkles, more complex patterns have also been observed. When elastic thin film floating on liquid is placed under biaxial compression, highly localized patterns which called crumples[10,11] appear. When the substrate is elastic rather than liquid, wrinkles undergo a post-buckling transition into period-doubling behavior [5-9]. Considering adhesion energy between film and substrate, delamination is also one of the possible buckling modes. Also, highly localized mountain ridges were observed by Cao and Hutchinson[48] when soft elastic substrate was highly prestreched. Similar ridges can also be induced when there is a large mismatch of Young's modulus of film and substrate[36] even when the substrate prestretch is modest.

However, none of the above experimental, theoretical, or computational studies of wrinkling on viscous supports mention ridge localization which will be introduced in next paragraph in detail. To our knowledge, Chatterjee et al[10] is the only article that definitively mentions ridge localization of elastic films on viscous substrates. There is no earlier research about how such long-wavelength buckling modes develop, the role of fluid viscosity, whether the process is rate-dependent, or whether ridges have a preferred spacing. This motivated our research to gain a deeper understanding of the ridge localization.

In our research of films on viscous supports that follows in Chapters 3-5, two distinct buckling modes can be identified and here we define them clearly. As in the previous literature on elastic systems, the wrinkling mode corresponds to roughly sinusoidal buckles appearing uniformly all along the film. In contrast, the ridges are more localized with large amplitude, and separated by nearly flat regions. The folding modes on energy-conserving substrates can have distinct buckling patterns. Depending on the properties of material, ridges may take on the form

of can be deep furrows in liquid substrate, or on period-doubled wrinkles on elastic substrates, or high mountain ridges on elastic substrate. To determine the buckling mode appearing under specific conditions, energy minimization theory has been applied[7]. The buckling of thin film floating on energy-conserving substrate can be understood as the competition between bending energy of film and elastic strain energy of substrate. A buckling mode with lower total system energy should always be more favorable[7,20,22,32,49]. Further, wrinkle wavelength and critical buckling strain can also be predicted by the energy method[7].

However, the problem is entirely different if the liquid support is viscous, and hence fully energy-dissipative. Two experiments of thin film buckling on viscous layer are shown in Fig 2.1. In both cases, a rubber strip with B15 liquid layer (details provided in Chapter 3) is firstly prestretched and held. Then an elastic film is bonded to the surface of the liquid layer. Finally, the rubber strip is released at a controlled rate and the film buckles into different buckling patterns. It is noteworthy that the patterns can show wrinkles or localized ridges. In these experiments, the viscous liquid substrate is completely energy-dissipative and the previous methods, such as finding the equilibrium state with lowest total system energy[3,4,7], cannot solve this problem. Thus, the basic model of this problem is no longer a competition between energies. Instead, the buckling can be understood as the strain applied to the film drives the buckling, whereas the viscous layer slows it down. Thus, the viscous stresses in the liquid film should be taken into consideration rather than the elastic energy of liquid support because the viscous liquid will dissipate mechanical energy. Since buckle development takes time, compression rate effects (which are clearly evident in Fig 2.1) must be accounted for.

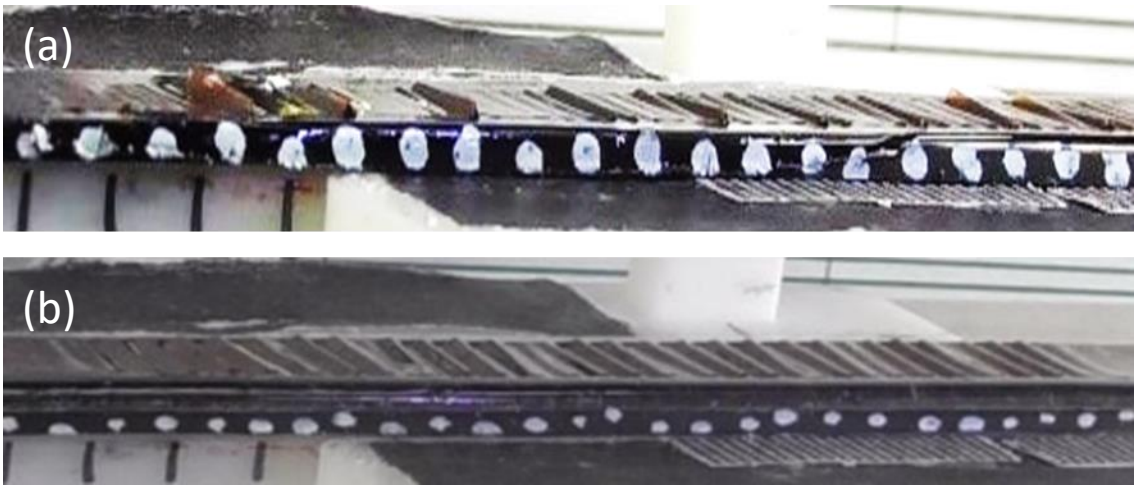

Figure 2.1: Buckling experiment with (a) $0.053\ s^{-1}$ compression rate and 0.19mm liquid thickness (b) $0.053\ s^{-1}$ compression rate and 1.52mm liquid thickness, this is conducted by undergraduate researchers Anantha Sarma and Eshwar Hamesh in the Velankar research group

A simpler scenario of a film under prestrain (rather than continuous compression) was provided by Sridhar and Suo in 2001[50].A film of thickness h under a compressive strain ϵ_0 is placed on the surface of initially-solid substrate. Then the solid substrate is melted into a viscous liquid by heating. After that, the compressive stress can be relieved by bucking accompanied by fluid flow. Sridhar and Suo conducted a linear stability of this situation and calculated the growth rate for wrinkling as a function of wavenumber k. The normalized growth rate as a function of dimensionless wave number hk is shown with different thickness ratios of substrate to the film. There is a critical wavenumber k_c such that that any wavenumber smaller than k_c will not be stable. In other words, any wrinkle with a wavelength larger than $\frac{2\pi}{k_c}$ will grow, whereas wrinkles with wavelength smaller than $\frac{2\pi}{k_c}$ will not grow. There is also a wavenumber k_m with the maximum instability rate, which corresponds to the fastest growing wavelengths. This can also be explained qualitatively: wrinkles with sufficiently long wavelength should be more favorable because they have lower strain energy for bending. However, long wavelength wrinkles need

longer time to evolve and hence grow slowly. Sridhar and Suo showed that both hk_c and hk_m are proportional to the prestrain $\sqrt{\epsilon_0}$, and increase as the substrate becomes thinner. It is notable that unlike on a solid substrate, there is no critical strain for buckling; lower prestrains induce buckles at larger wavelength. Instead, buckling is a time-dependent process.

3.0 Experiment Observation in Film Buckling Problem

Portions of this chapter are included in a manuscript by Xianheng Guan, Anantha P. Sarma, Eshwar Hamesh, Junyu Yang, Nhung Nguyen, Enrique Cerda, Luka Pocivavsek, Sachin Velankar, Compression-induced buckling of thin films bonded to viscous substrates: Uniform wrinkles vs localized ridges, submitted to International Journal of Solids and Structures, submitted March 2022

While the basic phenomena of wrinkling and ridge localization can be illustrated easily by experiments, controlled experiments required careful selection of materials and geometry. Although we have conducted experiments in the wrinkle regime previously[51], for studying ridge localization, significant changes are needed. Of the many changes, two are worthy of detailed comment. First, previous experiments used a fluid of viscosity of about 1400 Pa.s, whereas here a fluid of far higher viscosity (see next paragraph) was used. This offers several fundamental and operational advantages as described in Appendix A. Second, due to the relatively low viscosity used previously, the liquid was simply poured onto the rubber substrate, allowed to self-level under gravity, and the film was gently placed on the liquid surface. Those procedures are not viable for the high viscosity fluid here; instead the film was applied onto a pre-stretched liquid substrate as per the procedure described below.

3.1 Materials and methods

Materials: Butyl rubber strips of 1.58 mm thickness were cut to a width of either 1 inch (25.4 mm) or 0.5 inch (12.7 mm). The liquid used was BASF Oppanol B15, which is polyisobutylene (PIB) of molecular weight of roughly 85 kg/mol as quoted by the manufacturer. The rheological characteristics of this fluid are shown in Fig. 6.2. The complex viscosity at low frequency is roughly 10^6 Pa.s, with modest shear thinning. In most of the experiments, the rates applied were on the order of 0.01 s^{-1} and shear thinning effects, although present, may be modest. The highest rates in our experiments were roughly 0.09 s^{-1} and shear thinning may be somewhat significant for these experiments. The fluid is also viscoelastic as judged by the significant magnitude of the storage modulus G' as compared to the loss modulus G''. At the conditions typical of most of the experiments (rates on the order of 0.01 s^{-1} and strains of a few percent), we may estimate the stress contributions as follows: The fluid stresses attributable to viscous forces are on the order of $(viscosity) \times (rate) \sim 10^6 \times 0.01 \sim 10^4\ Pa$. The stresses attributable to elastic forces are on the order of $(modulus) \times (strain) \sim 10^4 \times 0.05 \sim 500\ Pa$. This suggests that most of the phenomena are due to viscosity, and hence a purely viscous Newtonian fluid would show the same phenomena, at least qualitatively. Indeed crude experiments conducted with an approximately Newtonian fluid show all the qualitative features noted in the careful experiments with Oppanol B15 PIB. Further, as will be shown in this chapter, ridges appear at low rates, not high. This gives further confidence that the central interest of this research – localization of buckles – is primarily a Newtonian fluid effect.

The films used in the experiments were polyester shimstock film purchased from McMaster-Carr Supply Co. with a film thickness of h =25.4 micron.

Sample preparation: A long worm-like cylinder of polyisobutylene of the desired mass and length (~130 mm) was placed lengthwise on the rubber strip. The PIB was then covered with a sheet of silicone rubber, pressed in a compression molding machine with the desired spacers to regulate the final compressed thickness, and silicone rubber layer removed.

The experimental setup illustrated in Fig. 3.1 consists of clamping the rubber strip, already covered with the liquid layer, between grips which attach the strip onto the surface of cylindrical drums of diameter 44 mm. The stress-free length of the rubber strip between the grips was 180 mm. The drums were then counter-rotated to stretch the rubber strip to about 130% of its original length. After waiting for several minutes to allow relaxation of any stresses in the liquid layer, the film of length $2L = 100$ mm was applied on the liquid surface taking care to avoid air blisters. The drums were then counter-rotated at the desired circumferential velocity (henceforth denoted the clamp velocity) to allow the rubber strip to recover to ~120% of its original length. Further, the central portion of the rubber strip rests on a lubricated flat surface which was raised a few mm with respect to the drums. This forces the rubber strip to remain flat, i.e. avoid tension-buckling.

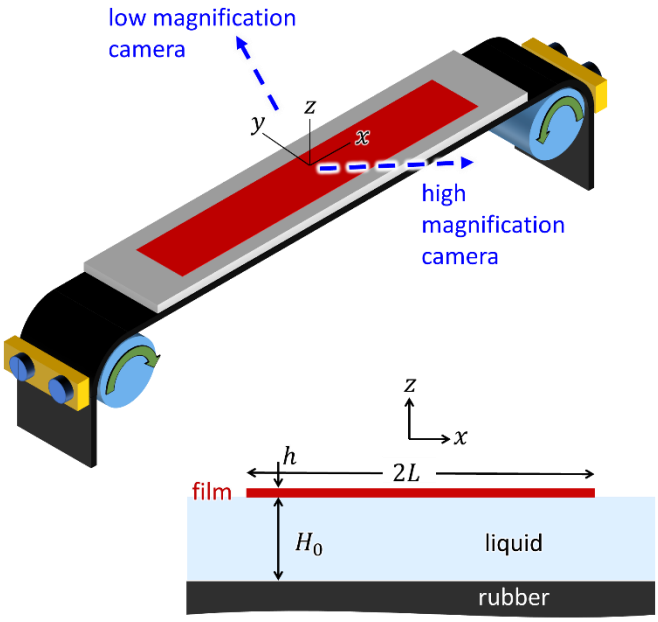

Figure 3.1: Schematic of the experiment. Note that the low-magnification camera views the film at a steep angle, whereas the high-magnification camera at a shallow angle. Bottom right: cross-sectional view defining the geometric parameters. This schematic is not to scale; in fact $2L$ is far larger than the other dimensions.

Imaging and image analysis: The film was visualized at two different magnifications using two cameras. The conversion from image pixels to mm was calibrated by images of 1 mm thick slabs placed at the exact location of the samples. Visualizing the details of ridge formation is complicated by the fact that the location of the ridge is unpredictable, and the film compression is often too rapid to allow adjusting the camera position during the experiment. Moreover the ridges are often well-spaced and hence the high magnification camera would sometimes see only a few ridges. All figures in this chapter are frames extracted from the higher magnification videos, which allow details of the ridge amplitude to be evaluated.

In the experimental setup, the local strain within the sample cannot be controlled directly. It is only possible to control the rotational speed, and hence the circumferential velocity, of the drums that permit retraction of the rubber. Since viscous stresses are proportional to the strain rate, it is critical to know the actual strain rate experienced by the rubber underneath the film. This rate was measured by digital image correlation analysis. The camera-facing edge of the rubber strip was marked with ink spots, and the Blender software was used to extract the displacement of these spots with time.

These early experiments guided us in formulating two key questions. First: Does the width of the film play a role in ridge localization? For example, films with width comparable to the liquid thickness or to the wavelength may behave differently than much wider films. Further, the edge may affect buckling, e.g. due to effects such as liquid recession. Ridges may even initiate at the edges similar to how buckle delamination of films often initiates at edges[52,53]. In contrast, if width effects are modest, one may regard the situation as a 2D problem, greatly facilitating any theoretical or computational development. We conducted systematic experiments addressing this first question and identified conditions under which effects of sample width are modest, and a 2D approximation may be justifiable. Here we turn to the second question of how the two main parameters, compression rate and liquid layer thickness, affect wrinkling vs ridge localization.

Here we turn to the second question of how the two main parameters, compression rate and liquid layer thickness, affect wrinkling vs ridge localization.

3.2 Qualitative aspects of wrinkling vs ridge localization

Experiments were conducted at clamp velocities ranging from 0.1 to 10 mm/s, at liquid layer thicknesses H_0 ranging from 0.25 mm to 1.59 mm. Two series of experiments are conducted: one varying rate at fixed $H_0 = 0.25\ mm$, and another varying H_0 at fixed clamp velocity of 10 mm/s, which is shown in Compression.mp4. The immediate qualitative conclusion from these videos is that low speeds and low liquid layer thicknesses both promote ridge localization. This section uses frames from these videos to discuss some qualitative aspects of wrinkling and ridge localization.

To illustrate the extreme situations of wrinkling and ridge localization, Fig..2 shows a sequence of frames extracted from two selected videos. Fig.2A exemplifies the wrinkling situation which is more common at relatively large liquid layer thickness and rate. Upon being compressed from a flat stat, at a strain of roughly 0.02, buckles with a few-mm wavelength appear across the entire film surface and grow steadily up to the end of the compression. In some experiments, more complex phenomena may appear, e.g. coalescence of two neighboring peaks into a single one. Nevertheless, at the end of the compression process, the film has more-or-less uniform buckles everywhere.

Fig..2B, exemplifies the situation of ridge localization which is more common at relatively small liquid layer thickness and rate. Even at the earliest stage when buckles first appear, they are not uniform across the surface; instead they appear in “packets” of relatively large amplitude, separated by regions which have wrinkles of much smaller amplitude. With increasing strain, one or two buckles grow much more than the others, whereas some of the surrounding buckles grow much less or even reduce in amplitude. Fig..2B also shows that

occasionally, a buckle may delaminate from the liquid layer altogether. We presume this is due to some preexisting defect at the liquid-film interface. Yet, such delamination does not appear to interfere with the evolution of neighboring buckles. By the end of the compression process, the film has tall buckles separated by regions that are more-or-less flat.

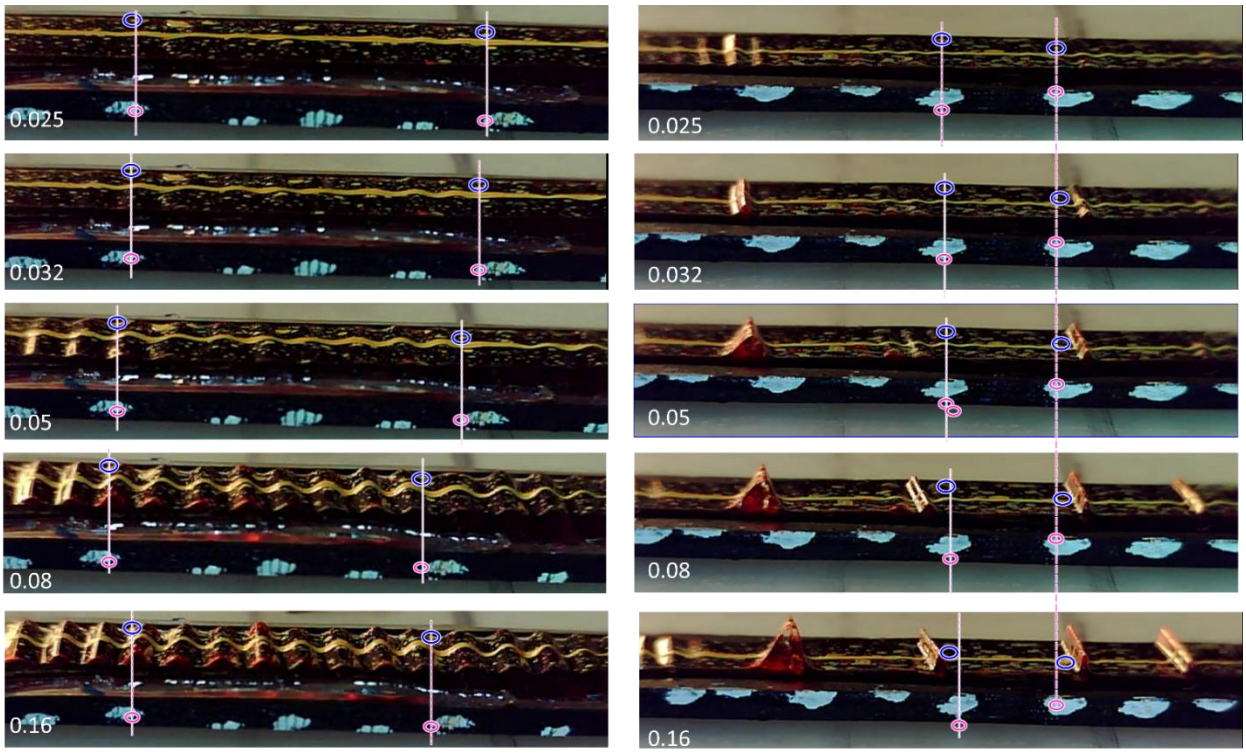

Figure 3.2 : Wrinkles (left) or localized ridges (right) developing under continuous compression. A. $H_0 = 1.5\ mm$, $\dot{\epsilon} = 0.064$, corresponding to each clamp moving at 10 mm/s. B. $H_0 = 0.25\ mm$, $\dot{\epsilon} = 0.0192$, corresponding to each clamp moving at 3 mm/s. The numbers in each image correspond to the strain ϵ in the rubber. The small arrows highlight complementary markers in the film and in the rubber layer.

Experiments across the range of H_0 and rate values show that this packet-like emergence of buckles becomes more pronounced as H_0 or rate reduces. Indeed at the lowest rate and thickness examined (corresponding to $H_0 = 0.25\ mm$, rate of $6.4 \times 10^{-3}\ s^{-1}$), ridges appears with little evidence of neighboring wrinkles suggesting that the film transitions directly from a flat state to localized ridges.

Close examination of the videos reveals a striking difference between the displacement of the paint markers, viz. that the paint markers undergo significant horizontal motion with respect to the rubber strip when ridges appear. Indeed, we had expected since simulations conducted prior to the experiments had already indicated this possibility. To illustrate this, Fig.2 compares markers on the film and on the rubber strip that are at the same horizontal position initially. The small pink ovals denote some well-defined small features on the rubber strip, and the dashed vertical pink lines are centered on these pink ovals. The blue ovals denote well-defined paint markers on the film surface. These are selected to be precisely above the pink markers in the top images. In Fig..2A, the blue and pink markers remain approximately coincident along the horizontal direction throughout the experiment, i.e. material points on the film and material points in the rubber strip do not separate significantly along the x-direction. In Fig. 2B however, there is significant relative motion: material points on the film near the fold "slide" towards the fold over distances that appear to be far larger than H_0. Such sliding requires shear flow in the film and will be discussed further later.

While this research is only focused on buckling behavior *during* compression, the films can undergo significant changes under quiescent conditions as well as illustrated in Fig. 3.3. This film was compressed under conditions corresponding to weak localization. Accordingly, the initial state is almost homogeneously wrinkled, although some peaks are narrower and taller than

others. However within 20 s under quiescent conditions, some of the wrinkles flattened significantly whereas others grew into localized ridges. This evolution continued so that at 180 s, tall ridges well-separated by much flatter regions are clearly evident. Yet, the formation of a localized ridge is not an irreversible process. For example, the small red arrows mark two ridges that first grew and then reduced in amplitude. In contrast, the small blue arrows mark a ridge that grew continuously under quiescent conditions. This ridge reorganization occurs over a long time and it is possible that gravity plays a significant role in this process.

To gauge the effect gravity, a small cylinder of the B15 fluid, roughly 2 mm in diameter (somewhat larger than the dimensions of a ridge), was placed on the surface of a 0.25 mm thick layer of B15. This cylinder was video-recorded as it sagged under gravity. There was little visible change in the cylinder height over 30 minutes. Thus we conclude that gravity does not affect the quiescent evolution of buckles in Fig. 3.3. These observations of quiescent evolution not only show that wrinkles can change into localized ridges, but further that these films prefer an ever-increasing degree of localization, and hence any particular ridge may eventually lose amplitude to a neighboring ridge.

Figure 3.3: Evolution of buckles under quiescent conditions. The top image corresponds to a nearly-homogeneous state of a sample with $H_0 = 0.8\,mm$ created by compressing at $\dot{\epsilon} = 0.064$, corresponding to each clamp moving at 10 mm/s. The numbers correspond to the time in seconds after the end of compression (QuiescentBehavior.mp4).

3.3 Displacement of material points

We now turn to a more localized view of the buckling process, focusing not on averages, but on narrow regions that span only a few buckles. Our video imaging was optimized for viewing relatively large areas of film to quantify interridge distances, and not for measuring buckle amplitudes. Specifically, imaging several ridges requires capturing film lengths of about 40 mm, whereas even the highest buckle amplitudes are 100-fold smaller. Moreover, since the liquid layer extends beyond the film edge in the width direction, a view along the y-direction –

which would be suitable for capturing ridge amplitudes – is not possible since the troughs may become invisible as they get "buried" under the surface of the adjacent liquid. Nevertheless, with a shallow view angle, and by tracking markers on the film surface, we can approximately quantify the displacement of material points on the film with respect to the rubber strip. This can quantify buckle amplitudes as well as the horizontal motion of the film mentioned in Section 3.2.

Fig. 3.4 performs this quantification for two experiments corresponding respectively to wrinkling (left column of Fig. 3.4) and ridge localization (right column of Fig. 3.4). For this quantification, we track marker pairs: one marker on the film and an immediately-adjacent ink mark along the edge of the rubber (see Fig. 3.4A and B). The difference between the displacements of these two markers, dubbed *separation* in the rest of this section, approximates the relative motion of material points in the film relative to underlying material points in the rubber substrate. Note in the absence of buckling, vertical separation between a pair of markers would increase due to the incompressibility of the rubber and of the liquid layer.

Fig. 3.4A corresponds to the development of a roughly homogeneous wrinkled state, and we track five markers which eventually become three adjacent peaks and two intermediate troughs in the homogeneously-wrinkled region. The spatial trajectories (Fig. 3.4C) show approximately vertical motion of the peaks, whereas the troughs show little displacement. When examined as a function of strain, the vertical separation of the markers (Fig. 3.4G) shows behavior typical of a wrinkling transition wherein all markers move in tandem up to buckling, followed by a sharp increase in the separation at the peaks and a decrease in the separation at the troughs. Further, over most of the experimental time, the horizontal separation of the marker pairs (Fig. 3.4E) remains small with no sharp changes with strain.

Fig. 3.4B corresponds to ridge formation. Of the five markers, one eventually becomes the peak of a ridge, two become neighboring peaks, and two become the intermediate troughs. Fig. 3.4D shows a sharp difference with respect to Fig. 3.4D: the peak of the ridge moves almost vertically with respect to the rubber, whereas the neighboring markers have predominantly horizontal motion towards the central marker. Examining the strain dependence, at small strain, all five markers move in concert, with the horizontal separation remaining near zero. Buckles first become visible at a strain of roughly 0.02, indicated by the small vertical arrows in Fig. 6F and H. At a strain of roughly 0.03, the vertical separation of the central marker starts increasing rapidly (Fig. 3.4H). Simultaneously, all the markers start moving horizontally (Fig. 3.4F).

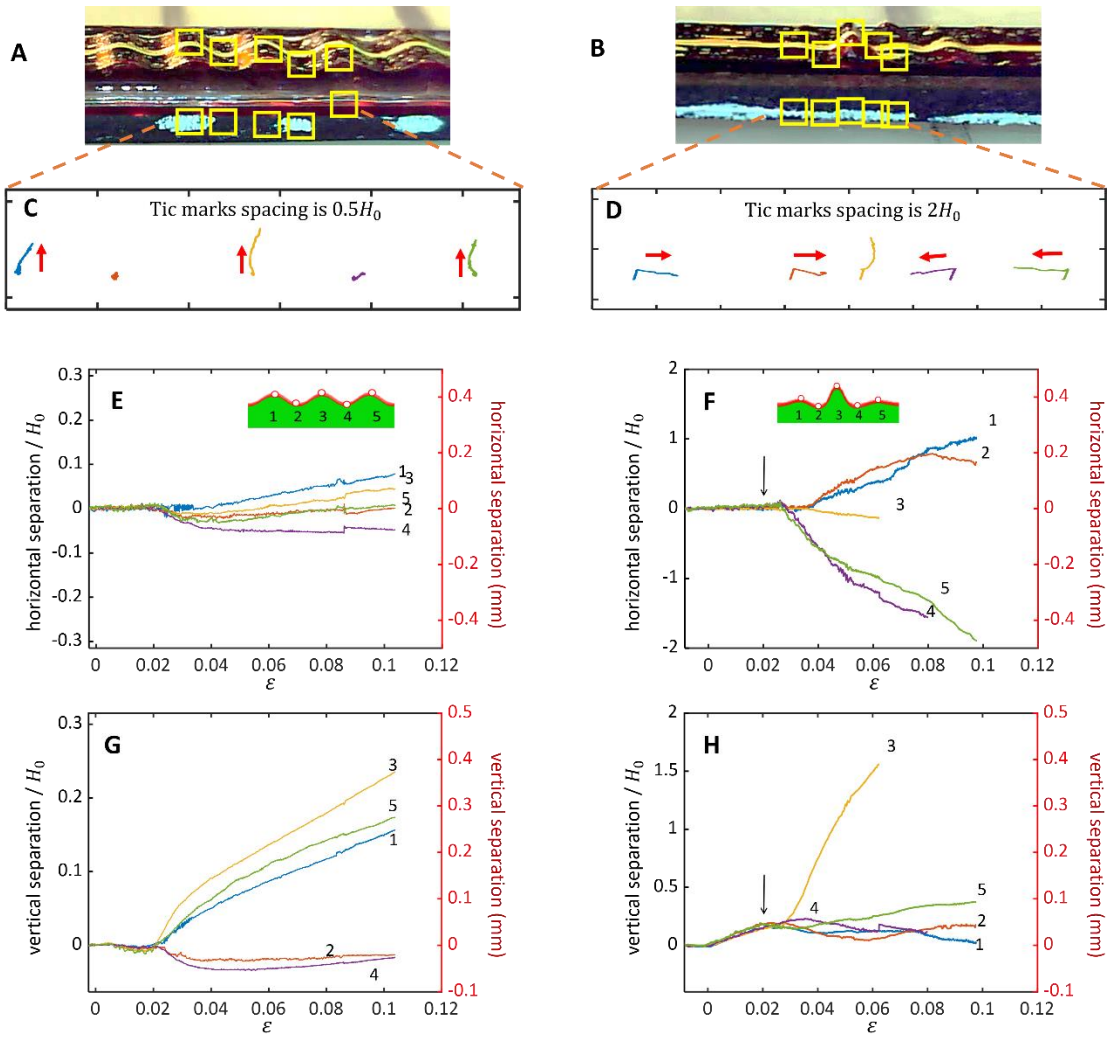

Figure 3.4: Quantification of motion of material points in wrinkling experiment (left column), and localization ridge experiment (right column). A&B: Regions of interest selected for estimating separations. The yellow boxes indicate the material locations that are tracked. C&D: Spatial trajectories of marker separations (see text). E&F: Horizontal separation (see text for definition) vs strain, and G&H: Vertical separation vs strain. In F and H, the small vertical arrows indicate the first appearance of visible buckles.

The differences between wrinkling and localized ridge are much more stark when recast in non-dimensional terms, which corresponds to the left y-axes in Figs. 3.4E-H. The non-dimensional amplitude of the ridge is almost 4-times larger than of the wrinkles. Further, the

ratio of the horizontal separation to H_0 is a measure of the local shear strain in the fluid, and a comparison of Fig. 3.4E vs G shows that this shear strain is at least an order of magnitude larger in the localization ridge situation. Further, the markers near the central peak in Fig. 3.4F show a shear strain of as much as 1.5 strain units, which is over 10-fold larger than the applied compressive strain. By implication, the shear rate in the liquid is also 10-fold larger than the applied compression rate.

3.4 Discussion of experiments

To summarize the central experimental observations, the Section 3.1 pointed out that the film width and the film edge both play a complex role in the entire process. Yet, for film widths that are not too narrow, one may simplify and treat the situation as approximately 2D – at least in the sense that ridges appear qualitatively independent of film width. The experiments of Section 3.1, which were then conducted under these pseudo-2D conditions, show that ridge localization is favored by low liquid layer thickness and by low strain rate. Sections 3.2 then quantify the videos. We acknowledge that these experiments were not designed to quantify buckle profiles, and the displacements of material points may not be quantitatively accurate. Nevertheless, two observations can be made with confidence, first that interridge distances reduce as rate or liquid thickness increases, and second that the film undergoes significant horizontal motion coincident with ridge development. Indeed both observations are qualitatively obvious even by viewing the videos.

We now speculate on the mechanics of ridge localization. Section 3.1 noted that even samples that show uniform wrinkles during compression evolve into localized ridges after the compression is stopped. This suggests that localized ridges provide a lower energy state than uniformly-distributed wrinkles. Yet, the fact that wrinkles appear under rapid compression suggests that ridges are kinetically limited. At the outset of this research, one goal was to identify the strain for a wrinkle-to-ridge transition. However these results suggest rather than a transition from wrinkles to ridges, it may be better to regard wrinkling and localization ridges as processes that compete against each other. Both relax the elastic energy, but ridge formation is slower, presumably because forming well-spaced ridges requires displacing the film (and the underlying fluid) over relatively large distances. This is not due to any unique characteristics of ridges, but common to *any* instability in which viscosity plays a retarding role, e.g. capillary instabilities of viscous threads[54], spinodal decomposition in the bulk[55], spinodal dewetting of thin films[56], buckling of elastic fibers in viscous media[57], or indeed sinusoidal wrinkling of elastic films on viscous supports[50,58]. In all these cases, long-wavelength instabilities are energetically-favorable, but penalized by their slow kinetics.

As per this physical picture therefore, whether an experiment results in uniform wrinkles or localized ridges depends on the compression rate. At low rates, the film may directly buckle into localized ridges. As a ridge develops, it relieves the local compressive strain in the film, thus wrinkles can no longer form. We speculate that any pre-existing defects may accentuate the tendency to form localized ridges, and hence encourage transition directly from a flat to a folded state. As loading rate increases, ridges cannot develop sufficiently rapidly and hence the film first wrinkles, and then reorganizes into ridges during compression. At sufficiently high rates, wrinkles grow almost uniformly up to the end of the compression. The driving force for

localization persists however, and therefore after stopping compression, wrinkles gradually become non-homogeneous.

The effect of the liquid layer can be thought of in three distinct ways: gravity, incompressibility and viscosity. The first effect of the liquid, that it induces a gravitational penalty for any variation in film height, is relevant in many static loading situations. This effect is ignored here since gravitational effects are negligible at least over the timescale of the loading process. In fact Chatterjee et al had confirmed previously[10] that tilting the sample by 90° made no qualitative difference to ridge formation.

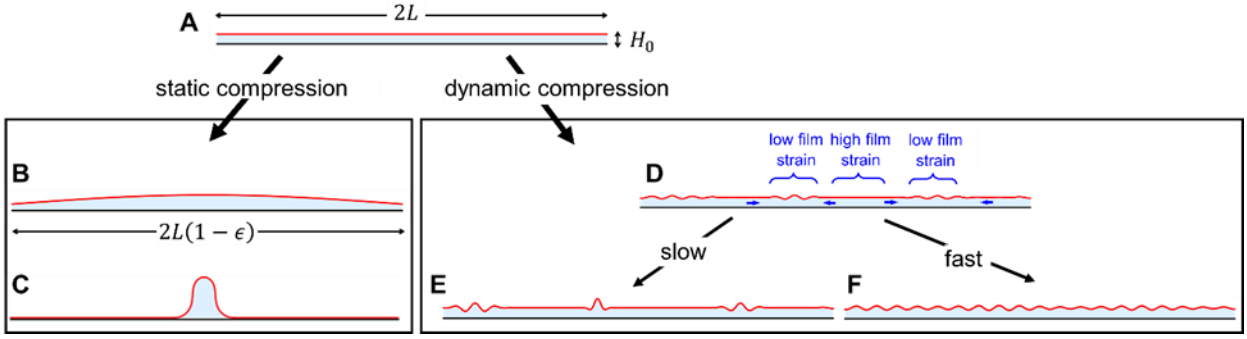

Figure 3.5: A. Schematic of an elastica (red) placed at a distance H_0 from a surface (rubber layer) shown in black. B&C. Shapes expected shape if the elastica minimizes energy at small strain (C) and at large strain (D-F) Compression at finite rate. D. Packets of buckles appear at small strain. Regions with high amplitude have lower film strain, and the corresponding strain gradient induces horizontal film motion (blue arrows). This causes the growth of localized ridges if compression is slow (E). At high compression rate, additional buckles grow between the packets giving approximately-uniform wrinkles.

The second effect is relevant to sufficiently wide films for which exchange of fluid across the edge of the film is negligible over the timescale of the compression. Accordingly the fluid imposes an incompressibility constraint so that the volume of fluid under the buckles must be

preserved. This liquid incompressibility condition shows most transparently why a localized buckle is energetically-favorable. Specifically, consider the following 2D problem posed in purely geometric terms: An elastica of length $2L$ is placed parallel to an underlying flat surface at a certain distance $H_0 \ll 2L$ as illustrated in Fig. 3.5A. The end-to-end distance of the elastica is now reduced by $\Delta = 2L\epsilon$ so that the elastica must be accommodated within the length $2L(1-\epsilon)$, while maintaining its contour length. Crucially, fluid incompressibility forces the area between the elastica and the underlying flat surface to remain at a value of $2LH_0$. At small values of strain ϵ, the two constraints (length of elastica and area under the elastica) can be satisfied by a single sinusoidal profile (Fig. 3.5B) with a wavelength spanning the system length. At small strain, the amplitude of this single sinusoid is proportional to $L\sqrt{\epsilon}$. With increasing strain, the amplitude increases until the film is forced to contact the underlying surface. It seems intuitive that in such a situation, the lowest energy state is not multiple buckles, but a single localized buckle of a shape qualitatively illustrated in Fig. 3.5C.

An unexpected result from our experiments is that buckles first appear in "packets", which then grow into ridges with no change in position. We conjecture that these packets of wrinkles add natural imperfections to the film and select the positions where ridges may develop. But ridges actually develop only if their amplitude can grow sufficiently rapidly as compared to the primary wrinkles. We therefore propose Fig. 3.5D-F as the mechanism whereby buckles grow as localized ridges or uniform wrinkles. Due to the packets at the buckle threshold (Fig. 3.5D), some regions have higher amplitude than others. Since buckling relieves compressive strain, these high-amplitude regions have lower film strain than their neighboring regions. The resulting film strain gradient induces a stress in the film that pushes the film from the low-amplitude to high-amplitude region (Fig. 3.5D), thus making the ridges taller (Fig. 3.5E).

Crucially, this horizontal motion also relieves the compressive strain in the adjacent film, thus inhibiting buckle growth in the region around the ridges. Indeed the same mechanism is active near the film ends: a gradient in film strain induces horizontal motion at the film ends (which can be captured by the shear lag model[10,59]), thus suppressing buckling near the ends. In the present situation, since ridge growth requires film motion over multiple wavelengths, it is possible only at relatively low compression rates. At high compression rate, horizontal motion is too slow to relieve compression in the neighboring regions, and hence buckles grow everywhere (Fig. 3.5) giving nearly uniform wrinkles. The driving force for localization persists however, and therefore after stopping compression, wrinkles gradually localize into ridges, and ridges localize further into fewer ridges, as shown in Fig. 3.3.

In the above physical picture, horizontal motion of the film is crucial to ridge growth, as was indeed shown in Fig. 3.2. This horizontal motion of the film is regulated by the third effect of the fluid layer, which is to retard flow between the film and the rubber strip. It is helpful to think of the film motion parallel to the rubber strip separately from the motion perpendicular to the strip. For two parallel surfaces moving perpendicular to each other at a specified rate, lubrication theory[60] states that the viscous resistance scales as H^{-3} where H is the local liquid thickness. Accordingly, for sinusoidal wrinkles of amplitude $2A$, the viscous resistance under the trough ($\sim[H_0 - A]^{-3}$) may far exceed that under the peak ($\sim[H_0 + A]^{-3}$), thus causing a large up-down asymmetry between peaks and troughs. This asymmetry is such that the liquid thickness under a peak can change readily, whereas the liquid thickness under a trough cannot. This asymmetry by itself would not induce localization; it would only cause initially-sinusoidal wrinkles to develop increasingly flat troughs as the strain increases. Ridge growth further requires long-range film motion parallel to the rubber strip. As per lubrication theory, the viscous

resistance to local parallel motion between the film and the rubber strip scales as H^{-1}, a dependence that is far less severe as compared to perpendicular motion. Thus, with the film strain gradient (previous paragraph) as the driving force, one ridge may grow rapidly by "gathering up" the contour length of neighboring ridges or wrinkles.

The physical picture proposed here will be tested in later chapters and in fact we will show that a few well-spaced ridges do indeed have lower energy than uniform wrinkles. Further, simulations confirm that for ridge formation the film undergoes large translation parallel to the rubber layer, whereas for wrinkle growth, the film motion is almost entirely perpendicular to the rubber layer.

4.0 Compression-induced Buckling of Thin Films Bonded to Viscous Substrates: Film Length Effect

Portions of this chapter are included in a manuscript by Xianheng Guan, Nhung Nguyen, Enrique Cerda, Luka Pocivavsek, Sachin Velankar, Compression-induced buckling of thin films bonded to viscous substrates: Film Length effect, to be submitted to Journal of Mechanics and Physics of Solids

When a thin elastic film such as a sheet of paper is compressed uniaxially, it readily buckles at the longest wavelength permitted by its boundary constraints. For clamped boundaries, this corresponds to a single sinusoid with a peak in the center. However if the sheet is attached to a compliant substrate, the energy needed to deform the substrate penalizes long-wavelength buckling. In such cases, buckles take on the form of sinusoidal wrinkles at a wavelength that depends on the mechanical properties and geometry of the film and the substrate, but is independent of film length[61-64]. Upon further compression, a variety of post-buckling transitions can induce buckle localization. For soft elastic substrates that are relatively thick, the buckles can undergo period-doubling wherein alternate wrinkle troughs become increasing deep and sharp[32,44,49]. For relatively thin elastic substrates that are much softer than the film, the reverse happens: alternate wrinkle peaks become much taller, and this is called ridge localization[65]. Ridges can also appear if the substrate is prestretched before attaching the film[45,49,66]. Finally, for liquid substrates under gravity where the hydrostatic pressure associated with the buckle amplitude imposes an energy penalty, an extreme form of localization can appear

where a single trough becomes increasingly deep, while the remaining film reverts to being flat. This is generally dubbed fold localization[34,39,42].

In this research, we consider buckling of elastic films bonded to viscous substrates in the geometry of a film atop a viscous layer of specified thickness, which is itself bonded to a rigid substrate. Most past research in this field has examined the situation when the film bears a compressive prestrain (Fig. 4.1A), e.g. due to a mismatch in thermal expansion coefficients, or an epitaxial mismatch when the film was originally deposited. Such a prestrain is conceptually equivalent to applying an instantaneous compressive strain ϵ_0 to the substrate at some initial time $t = 0$. In response the film instantaneously develops the same compressive strain, which then reduces with time as the film develops uniform wrinkles[11,12,14,29,32,36]. The physics of such wrinkling formation is entirely different from that in the previous paragraph because a viscous substrate cannot store energy and hence does not impose an energy penalty. Instead, the wrinkle wavelength is selected by a tradeoff between the energy of buckling (short wavelengths are energetically-unfavorable because they require large bending energy) and the kinetics of buckling (long wavelengths grow slowly because they require long-distance motion of the viscous fluid[50,58]). Thus, wrinkles appear at the wavelength corresponding to the most unstable (i.e. fastest growing) buckle mode. Linear stability analysis, with the assumption of with the assumption of lubrication flow in the liquid, can successfully predict the wavelength and the growth rate of this most unstable buckle mode. Notably, unlike the case of a soft elastic substrate, such buckles do not have a critical strain – instead wrinkles develop with time with at a wavelength that is already determined from the prestrain at $t = 0$.

Fig. 4.1A is reasonable when the compressive strain is applied rapidly before significant buckles appear. For instance, if the compression results from a mismatch in thermal expansion,

the time needed for temperature changes may be far less than the time to develop significant wrinkle amplitude, especially if the viscosity is high. Yet, this "instantaneous loading" assumption is untenable if the compression is slow, or if the compressive strain is large. In those situations, buckles may appear even while the compression is in progress, and therefore the rate of compression must affect the buckling process. In fact, dimensional analysis can be readily conducted in two limiting cases, one that is strain-controlled, and the other that is rate-controlled. In the first corresponding to Fig. 4.1A, the film is compressed at infinite rate to a strain ϵ_0. In this case, no non-dimensional combination of material properties is possible and hence the buckling mode is determined by ϵ_0 and the film geometry; material properties only affect the rate of buckle growth, not the mode. In second limit, an initially strain-free film is compressed steadily at a fixed rate $\dot{\epsilon}$. In this case the buckling mode, the critical strain for buckling, and the post-buckling evolution under continued compression, must depend on the geometry and a non-dimensional rate (viscosity)$\times \dot{\epsilon}/$(film modulus).

Unlike the many examples of buckling under the conditions of Fig. 4.1A [11,12,14,29,32,36], the rate dependence of buckling has received very little attention. A previous paper from our lab[10] examined appears to be the only published example of continuous compression in the literature. The most remarkable result from that study was that two very distinct buckling modes can appear: either roughly sinusoidal wrinkles over the entire surface, or a few tall, well-spaced ridges separated by flat regions. While that study did not focus on ridge formation, more recently we showed experimentally[67] that low compression rates favor ridge localization, whereas high compression rates favor uniform wrinkling. Despite these two studies, our understanding of rate effects in film buckling on viscous substrates remains very limited.

Yet, examining the rate-dependence of film buckling is complicated by end effects. As illustrated in Fig. 4.1C, and elucidated by Liang et al[3], a film of finite length can relax compressive strain by outwards displacement of its ends, a process that is dubbed "end-relaxation" in this research. End-relaxation competes with buckling in that both processes reduce the in-plane compressive strain, and hence the elastic energy, in the film. Thus, if end-relaxation is sufficiently rapid, the compressive strain in the film can reduce to negligible values before buckles can grow significantly, as explored by Liang et al[3] for the case of films under a prestrain. The effects of end-relaxation under steady compression have not been explored, but we anticipate that they will differ from Liang et al in some key ways. Most importantly, a film with a prestrain must eventually relax to a stress-free state. In contrast, for continuous compression, the long-term fate of the film is expected to be much more complex. For example, the film may sustain a steady buckled shape where buckles in the middle coexist with a flat region at the ends (where strain is low). Alternately, the film may have unbounded growth of wrinkles in the middle, while maintaining flat ends. Ridge formation introduces further richness, and we will show here at relatively large strains, wrinkles turn into localized ridges near the center, whereas the film ends remain flat.

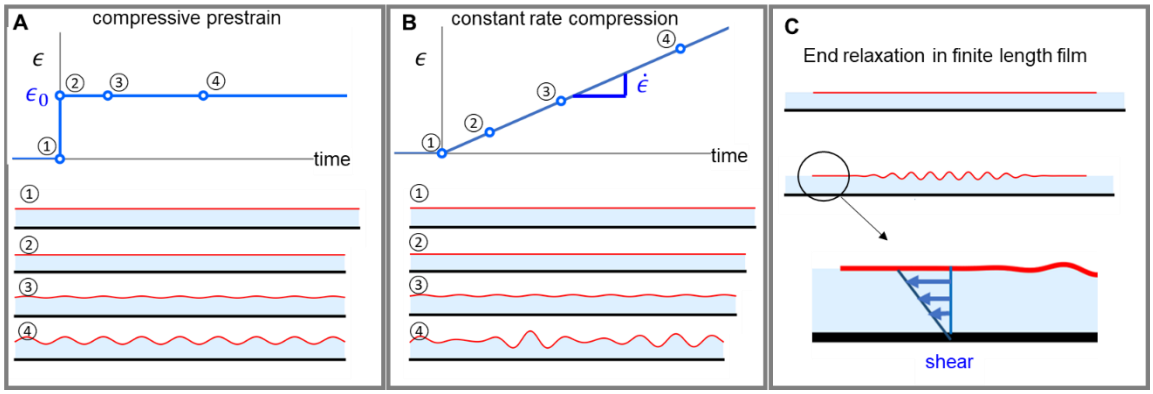

Figure 4.1: An elastic film (red) is bonded to a viscous liquid layer (blue) resting on a substrate (black). A. The black substrate is subjected to an instantaneous compressive strain ϵ_0 at $t = 0$, inducing gradual development of buckles on the film. B. The black substrate is subjected to continuous compression at a constant rate $\dot{\epsilon}$ starting from $t = 0$. Note that the lowermost schematic in B shows non-uniform buckle amplitude as noted in this research and in experiments[67]. C. A finite-length film with end-relaxation. The fluid undergoes shear flow near the film ends. The compressive strain remains low near the ends, and hence the film remains unbuckled near the ends.

The goal of this chapter is to examine the effects of end-relaxation on the buckling of films on viscous substrates by numerical simulations. This information will help guide further simulations (next chapter) in which buckling can be studied in isolation from end-relaxation effects.

One means of examining end-relaxation effects is to fix the material properties and geometry, and vary the rate of compression; as discussed above, slower rates allow more time for end-relaxation to relax compressive strain, and hence inhibit buckling. While this approach is viable, it is less convenient because experiments[67] indicate that even in very long films where end-effects become negligible, rate strongly affects the buckling process. Instead, we examine

the effects of end relaxation by keeping rate fixed, but varying film length, an approach similar to Liang et al[3]. As clarified in Section 4.1, the time required for the effects of end-relaxation to be felt at the center of the film scale with the square of the film length. Therefore, for a long film, end-relaxation only affects a narrow region near the ends, whereas end-relaxation affects the entirety of a short film.

4.1 Simulation method

Simulations were conducted for the geometry of Fig. 4.2 under plane strain conditions using ABAQUS explicit solver[2]. The simulation geometry is shown in Fig. 4.2, with a finite length along the x-direction, $2L$. The film and the rubber substrate were both modeled by neo-Hookean 1D beam elements with shear modulus G_{film} and G_{rubber}. The modulus of the film referred to in the main text is $E = 2G_{film}(1 + \nu_{film})$ where $\nu_{film} = 0.49$ to approximate incompressibility. The liquid layer was modeled as a 2D viscoelastic material with a modulus that decreases exponentially in time (see below). The meshing density of elements in all parts of the model is sufficiently high to ensure the accuracy of simulations. In all simulations, all elements are plane strain and domains are attached to each other with no slip.

The free surface of the film was set to be stress-free. The ends of the film were set to have zero force and moment. The ends of the rubber layer were translated inwards at fixed velocity v_{end}, and out-of-plane deformation of this layer was forbidden via a roller boundary condition. The modulus and thickness of the rubber was set to be much larger than of the film

ensuring that the in-plane strain, $\epsilon = \frac{end\ displacement}{rubber\ length} = \dot{\epsilon}t$, at all locations in the rubber was equal to the nominal value. Here the compressive strain ϵ and strain rate $\dot{\epsilon}$ are both taken as positive quantities. Accordingly, the compression of the rubber appears as a boundary condition on the lower surface of the liquid. Viscous forces in the liquid layer then transmitted the compression to the film, which buckled.

To model the viscous fluid layer, we use a viscoelastic material with an exponentially-decaying modulus. The time-dependent modulus is defined as $G(t) = G_0 \exp\left(-\frac{t}{\tau_v}\right)$. Accordingly, the corresponding fluid part has a viscosity $\eta = \int_0^\infty G(t)dt = G_0\tau_v$. It is expected that for the condition $\dot{\epsilon}\tau_v \ll 1$ the system is dominated by viscosity and displacements become important. To compute large displacements correctly, we use a hyperelastic material for the liquid layer. Specifically, a Neo-hookean model defined by the parameters $C_1 = G_0/2$ and $D_1 = 3(1-2\nu_0)/[(1+\nu_0)G_0]$ Since the elastic part is irrelevant for the large time behavior of the fluid, the initial modulus G_0 was set as equal to the film modulus, G_{film}. Although the fluid is incompressible, numerical instability is observed for a Poisson ratio $\nu_0 = 1/2$; hence, the Poisson ratio of the viscoelastic material was set to a safe value of ν_0 =0.475.

Fig. 4.2B shows example snapshots of simulations at three different film lengths, which will be discussed in detail later.

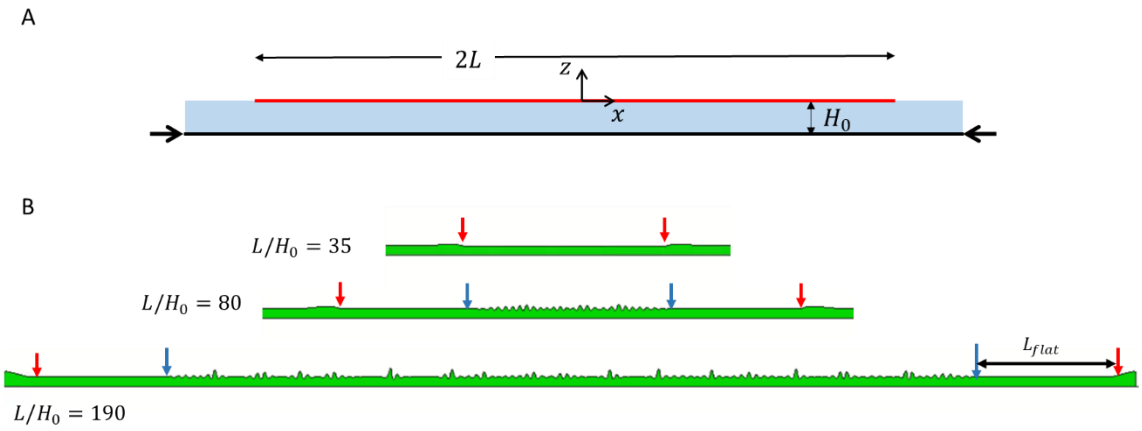

Figure 4.2: A. Schematic of "sandwich structure": red film bonded to the blue liquid substrate, which is itself bonded to black rubber layer. In the simulation, the ends of the rubber layer are translated inwards (thick black arrows) at a specified velocity. B. A snapshot of simulations with different film length showing the buckling profile (red arrows indicate the end of film and blue arrows indicate the end of buckling region) under same compressive strain of $\epsilon = 0.075$. All dimensions have been magnified by a factor of 2 in the vertical direction for clarity.

4.2 Results

4.2.1 Shear lag model prior to buckling

Before describing the simulation results, this section briefly reviews the mechanics prior to film buckling[10]. For finite films under plane strain conditions, the mechanics of the film prior to buckling can be captured by four non-dimensional parameters, the non-dimensional strain rate $\beta = (1-\nu^2)\eta\dot{\epsilon}/E$, the non-dimensional half length of the film L/H_0, the non-dimensional liquid thickness H_0/h, and the strain $\epsilon = \dot{\epsilon}t$, where E is the film modulus, ν is the Poisson ratio

of the film (set to 0.49 in the simulations), $2L$ is the length of film , η is the viscosity, H_0 is the thickness of liquid ($H_0 \ll L$). Assuming lubrication flow in the liquid layer, Chatterjee et al showed that the x-direction displacement in the film, $u(x,t)$, is given by a diffusion equation

$$\frac{du}{dt} = \frac{EH_0h}{\eta(1-\nu^2)}\frac{d^2u}{dx^2} + \dot{\epsilon}x \tag{4.1}$$

Here the quantity $\frac{EH_0h}{\eta(1-\nu^2)}$ plays the role of diffusivity, whereas the applied strain (last term on the right hand side) serves as a source term in the diffusion equation. Chatterjee et al solved for the displacement u and hence obtained the film strain $\epsilon^f = du/dx$ in the form of a series solution

$$\epsilon^f(x,t) = \frac{\beta L^2}{2hH_0}\left(1 - \frac{x^2}{L^2}\right) + \sum_{m=1}^{\infty} K_m \cos\left((2m-1)\frac{\pi}{2}\frac{x}{L}\right)\exp\left(-(2m-1)^2\frac{t}{\tau}\right) \tag{4.2}$$

where the coefficients K_m were given previously[10]. In the above equation $\tau = \frac{4L^2}{\pi^2 hH_0}\frac{\eta(1-\nu^2)}{E}$, called the shear lag time, is a characteristic diffusion timescale over which the effects of end-relaxation propagate over the distance L. In the short-time regime $t \ll \tau$, Eq. 4.2 reduces to

$$\epsilon^f(x,t) = \epsilon = \dot{\epsilon}t \quad for \quad t \ll \tau \tag{4.3}$$

over almost all the film except a narrow region at the ends where the film relaxes. This end-relaxation zone propagates towards the center over a timescale of τ, beyond which Eq. 4.2 reaches a long-time regime, which is a time-independent parabolic strain distribution

$$\epsilon^f(x,t) = \frac{\beta L^2}{2hH_0}\left(1 - \frac{x^2}{L^2}\right) \quad for \quad t \gg \tau \tag{4.4}$$

Fig. 4.3A illustrates the long and short time limits by plotting the film strain at the center (i.e. Eq. 4.2 evaluated at $x = 0$) vs the applied strain $\epsilon = \dot{\epsilon}t$. These graphs are plotted for the same three film lengths as Fig. 4.3B, and in all cases, the transition from the short to long-times occurs at $t \approx \tau$. The corresponding applied strains at the transition are simply $\dot{\epsilon}\tau = \frac{4L^2}{\pi^2 hH_0}\beta$, and are indicated by the short vertical lines in Fig. 4.3A.

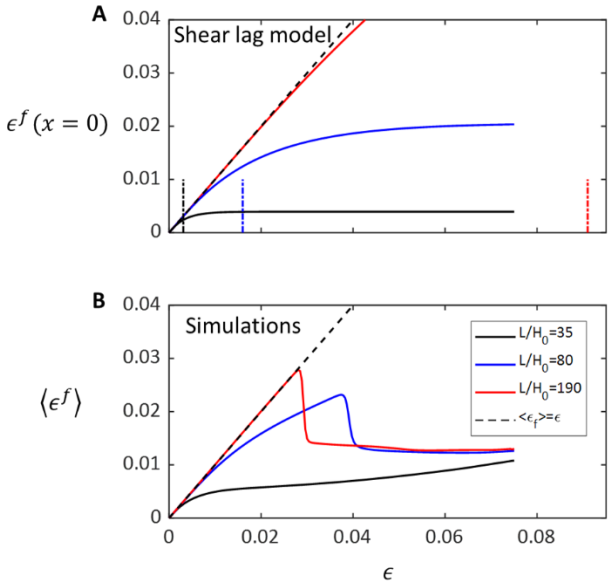

Figure 4.3: A. Prediction of shear lag model (Eq. 4.2) for the film strain at the center of the film vs strain applied on the bottom rubber layer. Vertical dot-dashed lines correspond to the strain $\dot{\epsilon}\tau$ for each of the three films (see text). B. The average strain $\langle\epsilon_f\rangle$ in the middle one-third of the film. In both graphs, dashed black line corresponds to $\langle\epsilon_f\rangle = \epsilon = \dot{\epsilon}t$.

The film may buckle at any stage during this strain evolution, and since the highest compressive strain is in the mid-section of the film (Eq. 4.4), buckles are likely to initiate at or near the center. Thus, buckles may initiate in two limiting conditions: either at $t \ll \tau$ when most

of the film is in a spatially-homogeneous strain state (Eq. 4.3), or $t \gg \tau$ when the film has reached a parabolic strain distribution (Eq. 4.4). Note that the short time regime persists for $t \ll \tau$, i.e. to $\epsilon \ll \dot{\epsilon}\tau = \frac{4L^2}{\pi^2 h H_0}\beta$, a value that increases quadratically with film length. Thus longer films are more likely to buckle while the strain state is still spatially-homogeneous. This distinction between buckling in the short vs long films will be made more clearly in the following sections.

4.2.2 Effects of film length on buckling

Fig. 4.2B shows snapshots for three different film lengths but identical $H_0/h = 9.84$, $\beta = 6.3 \times 10^{-7}$ and $\epsilon = 0.075$ chosen to illustrate three distinct behaviors. The uppermost image corresponds to a relatively short film ($L/H_0 = 35$) that does not buckle at all during compression. The middle image shows a longer film ($L/H_0 = 80$) that develops a few buckles near its center, but has large buckle-free regions near the film ends. The lowermost image shows an even longer film ($L/H_0 = 190$) that has numerous buckles near its center, but further, the buckles are clearly localized with regions of large buckle amplitude separated by regions that are nearly flat. The rest of this section analyzes in greater detail the evolution of buckles in all three cases.

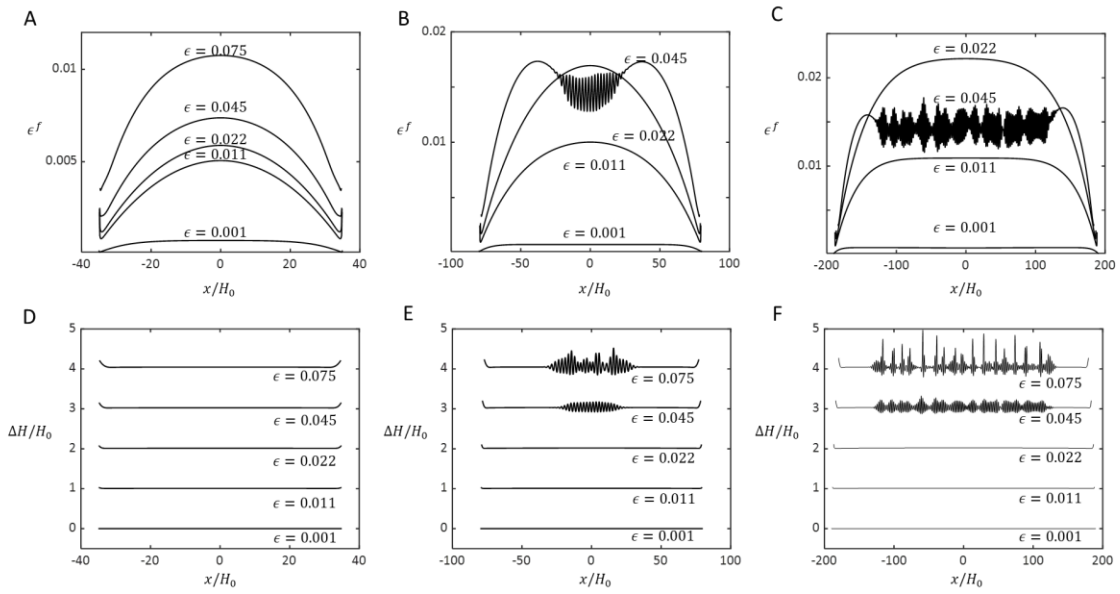

Figure 4.4: A-C Spatial profiles distribution of film strain, and D-F. spatial profiles of non-dimensional amplitude $\Delta H/H_0$ (defined in Eq. 4.9) in films with the $\Delta H/H_0$ values of 35 (left column), 80 (middle column) and 190 (right column). In the lower row of graphs, $\Delta H/H_0$ profiles at various strains have been shifted vertically with respect to the previous by one unit.

The upper row in Fig. 4.4 shows the evolution of the in-plane strain in the film, $\epsilon^f(x,t)$ during compression, whereas the lower row shows the amplitude profile normalized by the liquid thickness (the precise definition of amplitude is given in Eq. 4.9 later, but briefly H(x) is the height profile of the film, and DeltaH(x) is the amplitude profile). For the following discussion, it is also useful to have a measure strain in the film at its center. Yet, post-buckling, the strain in the film varies with position, and hence rather than using the strain at $x = 0$, instead we calculated the average film strain $\langle \epsilon^f \rangle$ in the middle one-third of the film $\left(-\frac{L}{3} < x < \frac{L}{3}\right)$, whose strain-evolution is shown in Fig. 4.3B.

At the earliest times, the evolution of film strain of all three films is similar: $\epsilon^f(x,t)$ remains independent of position near the center, whereas it reduces towards zero near the film ends. Further, the average film strain near the center equals the applied strain, i.e. $\langle\epsilon^f\rangle = \epsilon = \dot{\epsilon}t$ (Fig. 4.3B), consistent with Eq. 4.3. At later times, the behavior depends on film length.

For the shortest film with $L/H_0 = 35$, as strain increases, ϵ^f becomes position-dependent throughout the film length (Fig. 4.4A). Further, the mean value near the center is far lower than the applied strain (Fig. 4.3B). Both these are attributable to the effects of end-relaxation rapidly diffusing to the center. As a result, film strain does not rise to a sufficient level to induce buckling within the compressive strain applied in the simulations. Instead, the film (Fig. 4.4D) simply rises upwards (due to fluid incompressibility) while maintaining a nearly flat profile, except for a small upward rise near the ends consistent with experiments. Further, the film strain profile, $\epsilon^f(x,t)$ is in good agreement with Eq. 4.2 as shown in the Fig. S5.

In the other extreme, for the longest film with $L/H_0 = 190$ (Fig. 4.4E), the film strain ϵ^f increases until the film buckles. Buckling is marked by a sharp decrease in $\langle\epsilon_f\rangle$ as the film rapidly unloads its compressive stress. Prior to buckling, $\epsilon^f(x,t) \approx \epsilon$ throughout the mid-section of the film, i.e. buckling occurs from a spatially-homogeneous strain state which is not affected by end-relaxation. Near the film ends however there is a buckle-free zone because the ϵ^f remains small.

The intermediate case of $L/H_0 = 80$ (Fig. 4.4B) is similar to Fig. 4.4C in some respects: the film strain rises sufficiently to induce buckling, buckling is marked by a sharp decrease in $\langle\epsilon^f\rangle$, and there is a buckle-free zone near each end. The crucial difference however is that in Fig. 4.4B, the film strain profile $\epsilon^f(x)$ evolves to a nearly parabolic distribution before buckles

appear. Thus, for $L/H_0 = 80$ the buckling occurs from a non-homogeneous strain state, and therefore must be affected by end relaxation, whereas for $L/H_0 = 190$, the buckles are isolated from end-effects.

The discussion thus far mirrors the distinction between small, intermediate, and large lengths of film ("islands") made by Liang et al. In that case, the films bore a spatially-uniform prestrain which was relieved by end-relaxation. Small islands relaxed from their ends without buckling, analogous to Fig. 4.4A. However intermediate and large islands developed wrinkles before eventually reverting to a flat state analogous to Fig. 4.4B and C. Yet, the post-buckling behavior with continuous compression is quite different from that in Liang. As mentioned in the introduction, in the case of a fixed prestrain a film of finite length must eventually revert, by end-relaxation, to a flat, stress-free state. In contrast, Fig. 4.4 shows remarkable features. For both $L/H_0 = 80$ and $L/H_0 = 190$, after buckling, $\langle \epsilon^f \rangle$ quickly reduces to a time-invariant post-buckling plateau value which will be denoted $\langle \epsilon^f_{pb} \rangle$ in the rest of this research. I.e. increasing compression is entirely accommodated by amplitude growth, with no further compression of the film. Perhaps most remarkably, amplitude profile becomes highly localized such that some buckles become much taller than others. This non-homogeneous buckling will be dubbed the "ridge" regime henceforth, and is especially clear in the uppermost profile at $\epsilon = 0.075$ in Fig. 4.4F, and the corresponding snapshot in Fig. 4.4B.

Simulations were conducted across a wide range of film lengths for the same parameters ($\beta = 6.3 \times 10^{-7}$ and $H_0/h = 9.84$) as Fig.4.4. For each of these simulations several quantities were extracted. The critical strain in the rubber ϵ_c at the onset of buckling, and the corresponding average strain in the middle one-thirds of the film $\langle \epsilon^f_c \rangle$ can identified from the steep drop in $\langle \epsilon^f \rangle$ in plots of $\langle \epsilon^f \rangle$ vs ϵ (e.g. Fig. 4.4). Both these quantities are shown in Fig. 4.5A. The wavelength

immediately after buckles develop can be obtained from a correlation analysis of the amplitude profile, and is shown in Fig. 4.5B. Post-buckling, two quantities are reported, both at an applied strain of $\epsilon = 0.075$ (chosen arbitrarily). These are the post-buckling plateau strain $\langle \epsilon_{pb}^{f} \rangle$ (Fig. 4.5C), and the length of the buckle-free zone, L_{flat} near the film ends (Fig. 4.5D). The latter quantity is defined as the region near the film ends where the buckle amplitude (defined in Eq. 4.9 later) was less than $0.002H_0$.

Fig. 4.5A shows for the longest films, $\langle \epsilon_{c}^{f} \rangle = \epsilon_c$ whereas as film length reduces, ϵ_c increases sharply, whereas $\langle \epsilon_{c}^{f} \rangle$ reduces only slightly. Indeed the difference $\left(\epsilon_c - \langle \epsilon_{c}^{f} \rangle\right)$ is a quantitative measure of the extent to which end-relaxation affects buckling, and one may conclude that for $L/H_0 > 140$, the initiation of buckles becomes is independent of end relaxation. Fig. 4.5D shows that the buckle wavelength that appears at the buckling threshold is almost completely insensitive to L/H_0. Further, Fig. 4.5B and C show $\langle \epsilon_{pb}^{f} \rangle \approx 0.0136$ and $L_{flat} \approx 66$, also nearly independent of film length, suggesting that the post-buckling evolution is also independent of end-relaxation. Overall Fig. 4.5 indicates that for sufficiently long films (roughly $L_s > 140$), the buckling behavior of the mid-section and the relaxation near the ends are decoupled from each other, and hence both can be examined separately presuming infinite film conditions. This will be done in the following two sections.

Two other observations may be made from Fig. 4.5. First, the shortest film that develops buckles in our simulations corresponds to $L_s/H_0 = 70$ which is close to only slightly larger than L_{flat}/H_0. This suggests a simple physical picture: a length of L_{flat} near the ends cannot buckle due to end-relaxation, and for $L \approx L_{flat}$, buckling is suppressed because the entire film constitutes the buckle-free region. Second, at the buckling threshold we may draw an analogy

that the film resembles a free-standing column of length λ with clamped ends under a uniform axial load. For such a column, the buckling criterion becomes

$$\epsilon_c^{uni} = 10.45\left(\frac{h^2}{\lambda^2}\right) = 10.45\left(\frac{h^2}{H_0^2}\right)\left(\frac{H_0^2}{\lambda^2}\right) \tag{4.5}$$

where the superscript uni refers to uniform axial loading. All the simulations in this research used H_0/h=9.84. Then substituting the observed value of λ/H_0 from Fig. 4.5B yields $\epsilon_c^{uni} = 0.02$, which slightly underestimates critical strain ϵ_c^f. We propose the following interpretation: buckling initiates when the strain in the film slightly exceeds the strain that would induce buckles at a wavelength λ in a free-standing film with a uniform axial load. Post-buckling, the situation is more complex since the strain becomes highly non-uniform. Nevertheless, the film maintains an average strain $\langle\epsilon_{pb}^f\rangle$ that is only somewhat lower than ϵ_c^{uni}.

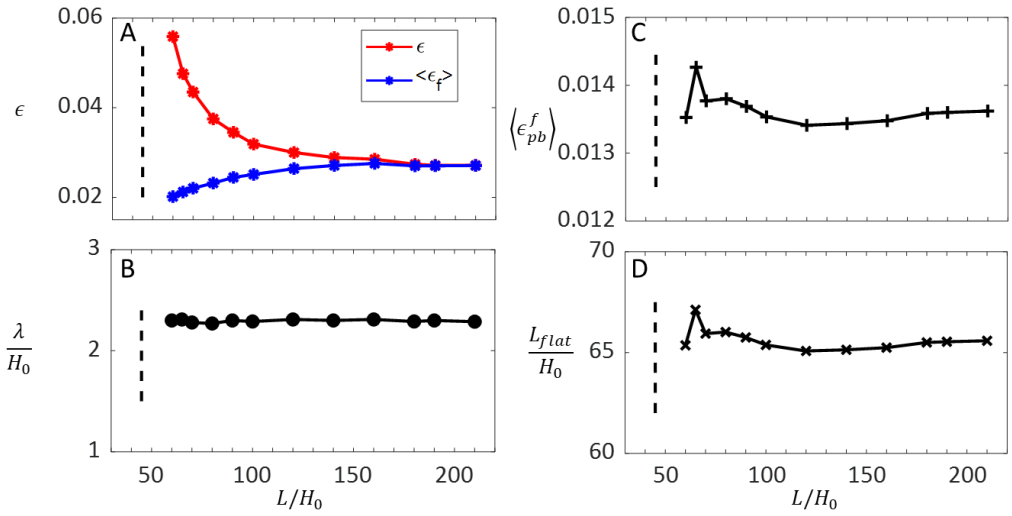

Figure 4.5: Dependence of A. strain in the rubber and the mean strain in the film at the onset of buckling, B. normalized wavelength C. strain in the film after buckling and D. normalized buckle-free length, on length of film. Vertical dashed line corresponds to $L/H_0 = 55$ at which buckles did not appear up to the strain applied in the simulations.

4.2.3 End relaxation and buckle-free length

After buckles appear, the strain in the film reduces significantly, and the shear lag model Eq. 4.2 no longer agrees with the strain profile. Nevertheless, near the film ends, the strain distribution can still be captured quantitatively by the shear lag approach. Conceptually, we may think of the buckle-free region as a flat region of the film of length L_{flat} which has strain of $\langle \epsilon_{pb}^f \rangle$ on one side, and a strain of zero at the free end. Accordingly, the strain distribution in the buckle-free region must be parabolic

$$\epsilon^f = \frac{\beta L_{flat}^2}{2hH_0}\left(1 - \frac{x^2}{L_{flat}^2}\right) \tag{4.6}$$

where the maximum strain $\frac{\beta L_{flat}^2}{2hH_0}$ is set equal to $\langle \epsilon_{pb}^f \rangle$, i.e.

$$L_{flat} = \sqrt{\frac{2hH_0 \langle \epsilon_{pb}^f \rangle}{\beta}} \tag{4.7}$$

In effect, L_{flat} "adjusts itself" to the value needed to sustain the strain $\langle \epsilon_{pb}^f \rangle$ in the buckled region. Using $\langle \epsilon_{pb}^f \rangle = 0.0135$ (obtained from Fig. 4.5B), Eq. 4.7 gives $L_{flat}/H_0 = 66$, which is in excellent agreement with Fig. 4.5C. Fig. S6 plots the near-ends film strain distribution from the simulations for L/H_0 values of 80 and 190. This shows that although Eq. 4.7 captures L_{flat}, it underestimates the film strain near the ends. Incidentally, later this this chapter, we will show that Eq. 4.7 also captures the dependence of L_{flat} on rate correctly.

One goal of this research is to identify the length beyond buckles appear, and also the length beyond which end effects can be ignored. The former is important if buckling is undesirable, whereas the latter is useful to examine fundamental questions regarding the mechanics of buckling under conditions that approximate infinite films. Eq. 4.7 now provides a simple way to estimate these lengths. In the previous section we mentioned that the post-buckling strain $\langle \epsilon_{pb}^f \rangle$ is somewhat lower than ϵ_c^{uni}. Replacing $\langle \epsilon_{pb}^f \rangle$ with ϵ_c^{uni} in Eq. 4.7 gives

$$L_{flat} = \sqrt{\frac{2hH_0\epsilon_c^{uni}}{\beta}} = \sqrt{\frac{2hH_0}{\beta}}3.23\left(\frac{h}{\lambda}\right) \tag{4.8}$$

which is expected to slightly overestimate L_{flat}. Eq. 4.8 can be applied only based on knowledge of the wavelength, which is highly insensitive to film length. Thus, for any given set of properties and rates, one may conduct a single simulation or experiment (at any film length) to

measure λ, and therefore estimate L_{flat} from Eq. 4.8. Buckling is not expected when L is less than the estimated L_{flat}, and buckling is expected to become insensitive to film length wen L is a few-fold larger than L_{flat}.

4.2.4 Uniform wrinkling vs ridge localization

As reported elsewhere[10,67] and commented on at the end of Section 4.2.2, a striking aspect of buckling on viscous substrates is that at high strain, buckles can localize to form well-spaced ridges. Qualitatively at least, ridges can be identified by two visually-obvious features. First, individual buckles or a pair of adjacent buckles becomes much taller than their neighbors, i.e. the amplitude becomes highly non-uniform across the sample. Second, the amplitudes become highly non-sinusoidal so that the peaks of ridges grow significantly whereas the troughs do not become significantly deeper. We have proposed[67] that this asymmetry of peaks vs troughs is because due to the small liquid thickness under troughs, viscous forces under the troughs are far larger than under the peaks. Thus, as buckles evolve, it becomes easier to grow peaks than deepen troughs.

The goal of this section is quantify the strain at which more-or-less uniform wrinkles transition into tall ridges. Since the transition is not an abrupt one, we must first construct a quantitative criterion to judge whether the buckled film is in a wrinkled state or ridged state based on the height of the buckles. We first define (Fig. 4.6A) the local amplitude $\Delta H(x)$ as

$$\Delta H(x) = H(x) - \frac{H_0}{1 - \dot{\epsilon} t} \tag{4.9}$$

where $H(x)$ is the local liquid height. Here the latter term on the right hand side is the change in liquid thickness expected even in the absence of buckling, i.e. without buckling, the film would simply rise upwards due to liquid incompressibility. Now we recognize that uniform wrinkles have an approximately sinusoidal profile and hence the amplitude of the peaks and the troughs is roughly equal. In contrast, as mentioned above, a signature of localized ridges is that the amplitude of the peaks far exceeds the amplitude of the troughs. Accordingly we list the amplitudes of all the peaks (ΔH_p values) and troughs (ΔH_t values) in the central one-third of the film and calculate the root-mean-square (RMS) averages:

$$p = \sqrt{\sum \left(\Delta H_p - \langle \Delta H_p \rangle \right)^2} \quad and \quad t = \sqrt{\sum \left(\Delta H_t - \langle \Delta H_t \rangle \right)^2} \tag{4.10}$$

Fig. 4.6 A and B show the strain-evolution of p/H_0 and t/H_0 in two simulations of different film length. Immediately after buckling, p and t grow in tandem, whereas upon further compression, they diverge from each other. We now set an arbitrary criterion that the film is deemed to have localized ridges if p/t exceeds some value C. The value of C must be selected such that the two key features of ridge formation mentioned above (highly non-uniform amplitude and peak-trough asymmetry) are clearly evident at $p/t = c$, but not for $p/t < c$. By examining the strain-evolution of the amplitude profiles, the value of $C = 1.3$ was found to satisfy this requirement. The benefit of this criterion is that since it uses all the peaks and troughs, it does not need manual judgements on which peaks are "sufficiently tall" to be deemed ridges.

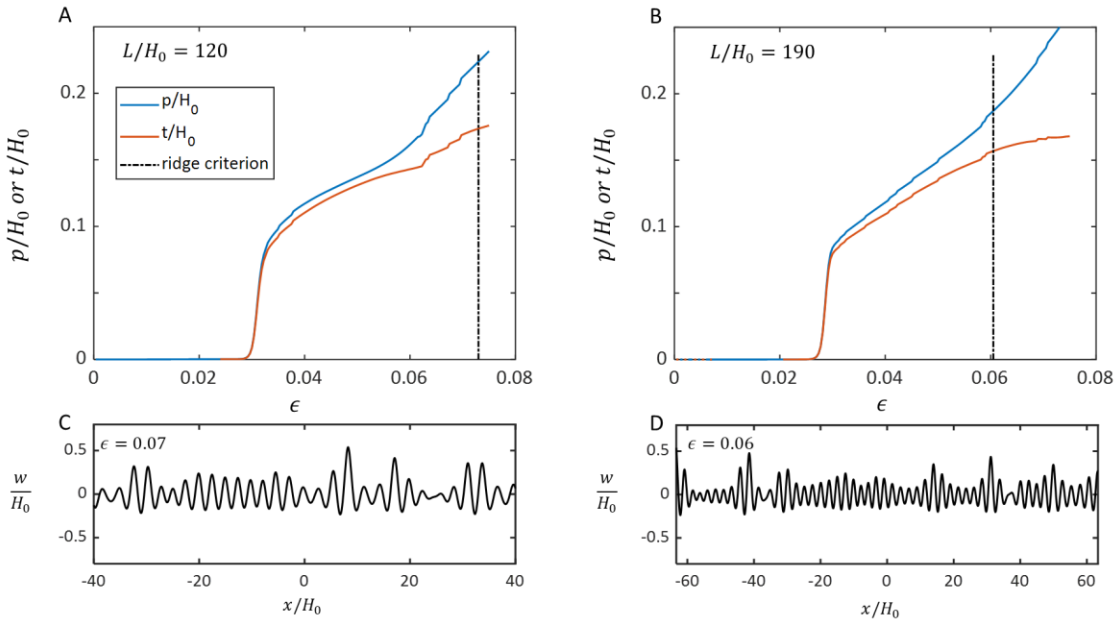

Figure 4.6: Strain-evolution of RMS of buckle peaks and troughs for films with the L/H_0 values listed at the top of each graph.

Adopting this criterion, Fig. 4.7 now constructs a state map of the regions of parameter space within which the film stays flat, wrinkles uniformly, or shows localized ridges.

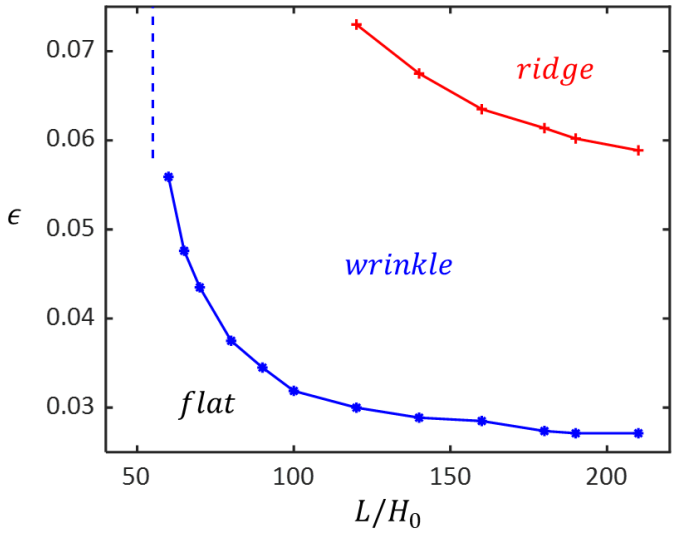

Figure 4.7: State diagram of the strains at which films of various length remain flat, develop uniform wrinkles (blue curve), or localized ridges (red curve). The vertical dashed blue line corresponds to $L/H_0 = 55$ at which buckles do not appear up to the maximum strain examined. Note that the lower curve is identical to the upper curve in Fig. 4.5A

4.2.5 Energetics of wrinkling vs ridge localization

Although Fig. 4.7 maps the strain needed for ridge localization at any given film length, it does not provide a mechanistic reason for why ridges develop, i.e. why instead of buckles growing uniformly, the amplitude becomes non-homogeneous with some buckles becoming much taller whereas others flatten. In Section 3.3 we proposed an energy-based explanation for ridge formation. Briefly, for sufficiently long films, since the liquid is incompressible, buckles must grow without changing the volume under the film. This implies that for thin liquid layers, the lowest energy state of the buckle must be a single tall ridge. However, forming such a ridge requires fluid motion over the entire length of the film, a process that becomes increasingly slow

as film length increases, and cannot occur over the timescale of compression. In contrast, sinusoidal wrinkles can form rapidly because they only require fluid motion over the scale of one wavelength. However, sinusoidal wrinkles require the entire film length to sustain a curvature, thus resulting in high bending energy. Therefore we proposed that multiple well-spaced ridges are a compromise: Since substantial portions of the film can become flat, their bending energy is lower than of sinusoidal wrinkles (although higher than a single tall ridge), but they no longer require fluid motion over the lengthscale of the entire film.

Crucially, this proposed explanation hinges on the idea that forming localized ridges offers lower energy than uniform wrinkles. In that experimental research[67], we were not able to test this quantitatively. However, simulation allow this explanation to be evaluated since the film energy can be calculated explicitly.

To compare the energy of the uniformly-wrinkled state vs a ridged state, the simulation with L/H_0 =190 (corresponding to Fig. 4.4 C&F) which is sufficiently long to approximate infinite film conditions, was selected. The critical strain for this simulation was $\epsilon_c = 0.027$, beyond which it developed wrinkles with λ/H_0=2.29. At higher strains, some of the buckles grew much more than the others to form ridges at an average interridge distance of $21H_0$. For our energy comparison, this simulation was repeated, but paused at a strain of 0.025 (below ϵ_c), and a perturbation was applied. The perturbation consisted of a 1% decrease in the modulus of the film at a spatial periodicity of either the wavelength or the interridge distance. The compression was continued with this perturbed film, and after a small additional strain, the film buckled, but along two distinct pathways. The film perturbed at a periodicity of the wavelength developed uniform wrinkles, whereas the one perturbed at a periodicity of the interridge distance developed ridges (exemplary snapshots shown in Fig. 4.8B). The benefit of the perturbation

method is that these two states were achieved with no change in mechanical properties, geometry, or compression rate.

The evolution of the energy for bending and for the in-plane compression (often dubbed stretching energy in the literature) in both states was calculated as

$$U_B = \frac{1}{2} AE \int_{-L/3}^{L/3} {\epsilon^f}^2 ds \tag{4.11}$$

$$U_S = \frac{1}{2} \frac{AB}{h} \int_{-L/3}^{L/3} \kappa^2 ds \tag{4.12}$$

where A is the cross sectional area (product of width and thickness) of the film, s is the coordinate along the film, and $B = Eh^3/12$ is the bending stiffness of the film. The curvature κ was calculated from the amplitude profile. To avoid end effects, only the middle one-third of the film was used for these calculations (specifically, the integration was conducted using the portion of the film which lay between $-L/3 < x < L/3$ at the beginning of the simulation. The results of these energy calculations are shown in Fig. 4.8 where the energy is normalized by EV_{film} where V_{film} is the volume of the film used in the integration.

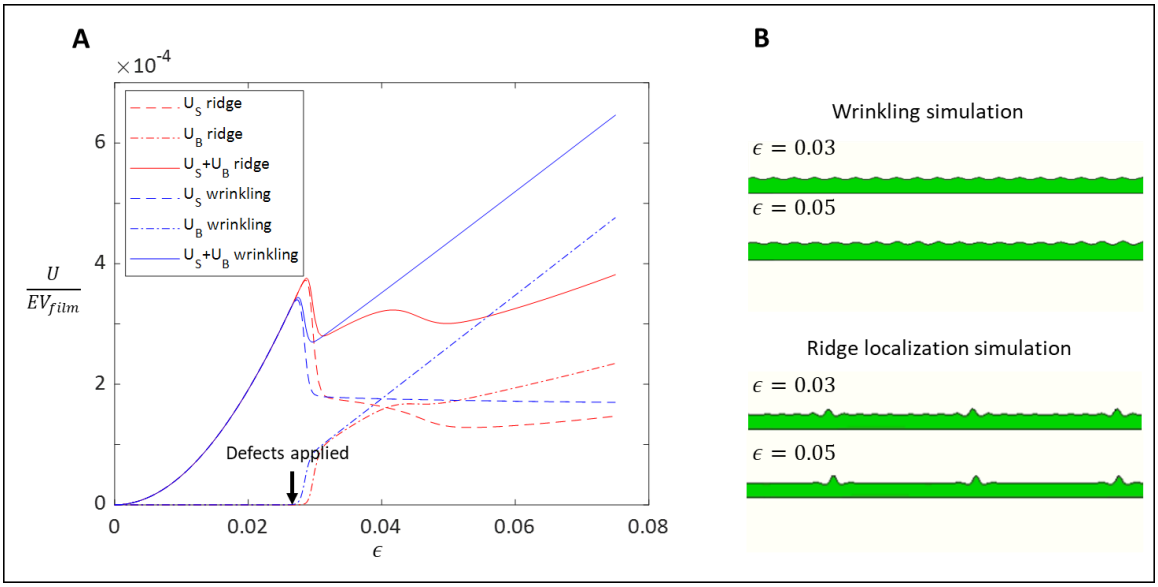

Figure 4.8: A. Evolution of elastic energy for bending, for in-plane compression, and their sum, for simulations with defects that induce the film to buckle in the wrinkle mode or the ridge mode. B. Snapshots of each simulation at different values of applied strain

Prior to buckling, the bending energy is zero, and since $\epsilon^f \approx \epsilon$ over the entire mid-section, $U_s/EV_{film} \approx \epsilon^2/2$. After buckling, U_s reduces sharply for both modes, whereas U_B rises as the film develops curvature. For both modes, U_S remains approximately constant as strain increases, with the ridged mode having a slightly lower value than the wrinkle mode. However, there is a large difference in bending energy where U_B of the wrinkle mode rises much more steeply. We propose that the relatively gentle rise in bending energy of the ridge mode is because large portions of the film separating the ridges become nearly flat. As the rubber compresses further, these flat regions do not reduce in length; instead the "excess length" is transferred to the ridge which grows in height. In an approximate sense, these flat regions between adjacent ridges behave analogous to short films which remain unbuckled due to end-relaxation. Regardless of details, the total energy of the ridge mode is much lower, thus confirming our previous explanation from Section 3.3.

4.2.6 Strain-strain rate map for wrinkles and ridges

Unlike in purely elastic systems, buckling on viscous substrates should depend on the compression rate. If film is sufficiently long, end-relaxation effect can be ignored. The buckling behavior will depend on strain and strain rate is thickness of liquid is fixed. Accordingly simulations were conducted at a variety of rates, using film lengths that were sufficient to approximate infinite length. The evolution of strain profiles resembled Fig. 5.5C and F in all cases in that buckles appeared from a homogeneous strain state when $\epsilon^f \approx \epsilon$ in the mid-section of the film.

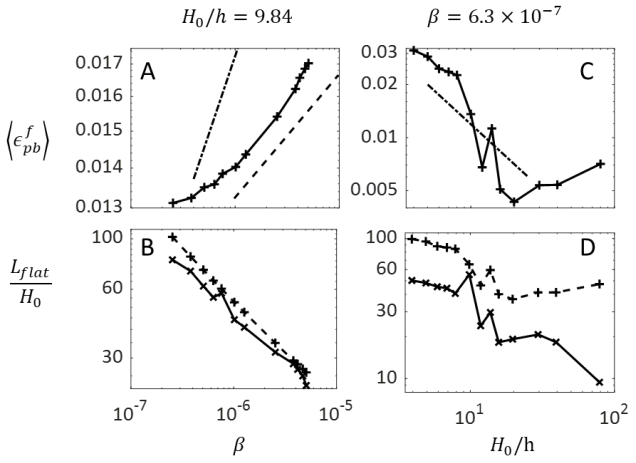

Figure 4.9: A. Effect of rate on strain after buckling, Dashed line in has a slope of 0.1 and dotted line has a slope of 0.25 for illustration. B. Effect of rate on buckle-free length. + symbols in B are calculated from Eq. 4.7. C. Effect of normalized liquid thickness on strain after buckling, The dotted line has a slope of -0.75 for illustration. D. Effect of normalized thickness on buckle-free length. + symbols are calculated from Eq. 4.7.

Fig 4.9A shows that the average film strain $\langle \epsilon^{f}_{pb} \rangle$ near the center is nearly independent of strain rate (the dependence of $\beta^{0.1}$ is shown to illustrate the weak dependence). Figure 4.9B

shows that L_{flat} is in close agreement with close agreement with Eq. 4.7 Due to the very weak dependence of $\langle \epsilon_{pb}^{f} \rangle$ on rate, L_{flat} varies approximately as $\beta^{-0.5}$, also consistent with Eq. 4.6.

Fig 4.10 shows that the average film strain $\langle \epsilon_{pb}^{f} \rangle$ near the center depends on the λ and $\langle \epsilon_{pb}^{f} \rangle$ varies approximately as λ^{-2}, which is shown in Eq. 4.5.

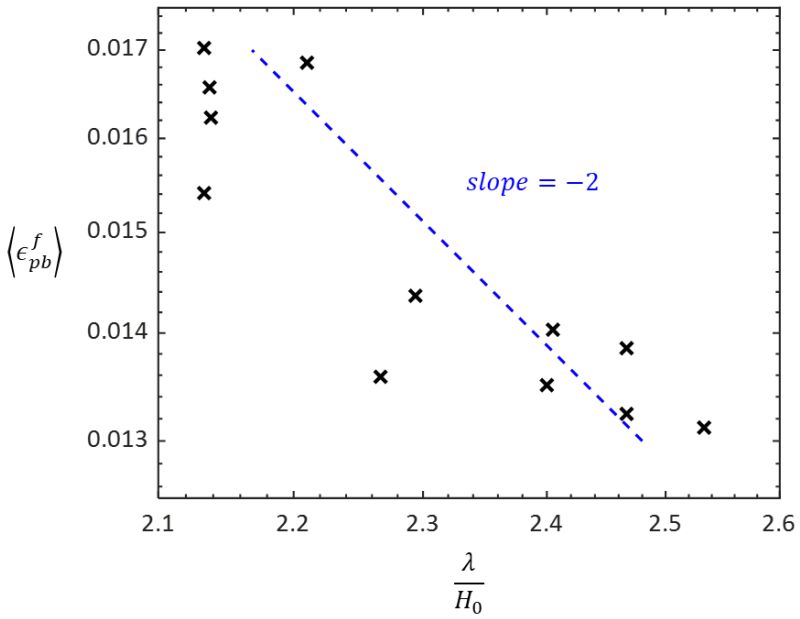

Figure 4.10: Effect of strain at steady state on wavelength. Dashed line has a slope of -2 for illustration. Note that both axes are logarithmic.

The same analysis as Fig. 4.7 was conducted on these simulations to classify the regions of the strain-strain rate parameter space within which the film remains flat, shows uniform wrinkling, or ridge localization. The resulting state map is shown in Fig. 4.11; note that this figure refers to infinite film conditions. An aspect is that ridges appear much after wrinkles, and at high rates, ridges do not appear within the strain range of simulations. In fact, in the next chapter we will show that, by using a different method to identify ridges, ridge formation is evident almost simultaneously with the buckle threshold.

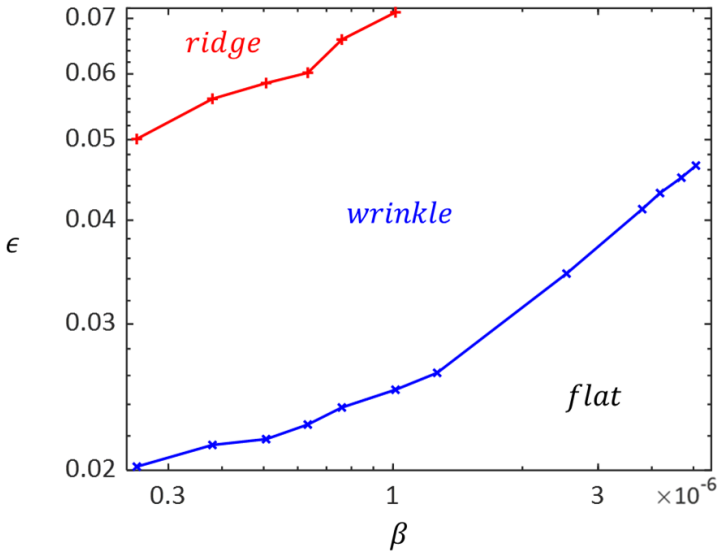

Figure 4.11: Buckling map based on strain in rubber ϵ and strain rate. The blue curve indicates the critical strain to induce buckling as the red curve indicates the critical strain to induce ridge localization.

5.0 Buckling of Long Films

Portions of this chapter are included in a manuscript by Xianheng Guan, Nhung Nguyen, Enrique Cerda, Luka Pocivavsek, Sachin Velankar, Ridge Localization Driven by Wrinkle Packets, submitted to Physical Review Letters, March 2022

The Chapter 4 clarified how film length affects buckling behavior. However, the end-effect can be ignored for sufficiently long films and film length is no longer a dominant parameter. The goal of this chapter is to find a method of quantifying wavelength and interridge distance. Further, the dependent of buckling behavior on compressive rate or liquid thickness is discussed.

The simulation method was same as described in section 4.1. For sufficiently long films under plane strain conditions, the mechanics of the film prior to buckling can be captured by three non-dimensional parameters the non-dimensional strain rate $\beta = (1-\nu^2)\eta\dot{\epsilon}/E$, the non-dimensional liquid thickness H_0/h, and the strain $\epsilon = \dot{\epsilon}t$, where E is the film modulus, ν is the Poisson ratio of the film (set to 0.475 in the simulations). The quantity $\beta^{-1} \propto E/\eta\dot{\epsilon}$ has the form of a stiffness mismatch ratio E/E_s, and plays a key role in our description. Incidentally the literature on thin film buckling sometimes uses the in-plane stiffness $Y = Eh$ and the bending stiffness $B = Eh^3/12(1-\nu^2)$ (rather than E and h) to characterize the film. In that case, the suitable non-dimensional numbers would be $\alpha = \eta\dot{\epsilon}H_0/Y$, the von Kármán number $N = \sqrt{YH_0^2/B}$, and the strain ϵ. However, our choice of using β and H_0/h offers the benefit of cleanly separating the material parameters from the geometric ones. The video file

Simulation.mp4 exemplary cases of wrinkling and ridge localization, and corresponding snapshots are shown in Fig. 5.2A and 5.2B. The first portion of the video shows that at high compression rate (large β), roughly-sinusoidal buckles grow almost uniformly. At the end of the simulation (Fig. 5.2A), there are no significant variations in buckle amplitude over the film. In contrast, at low rate (small β), as strain increases, a few buckles grow rapidly, whereas the remaining buckles grow much less or reduce in amplitude. Eventually, the film has a few tall buckles separated by regions that are more-or-less flat (Fig. 5.2B).

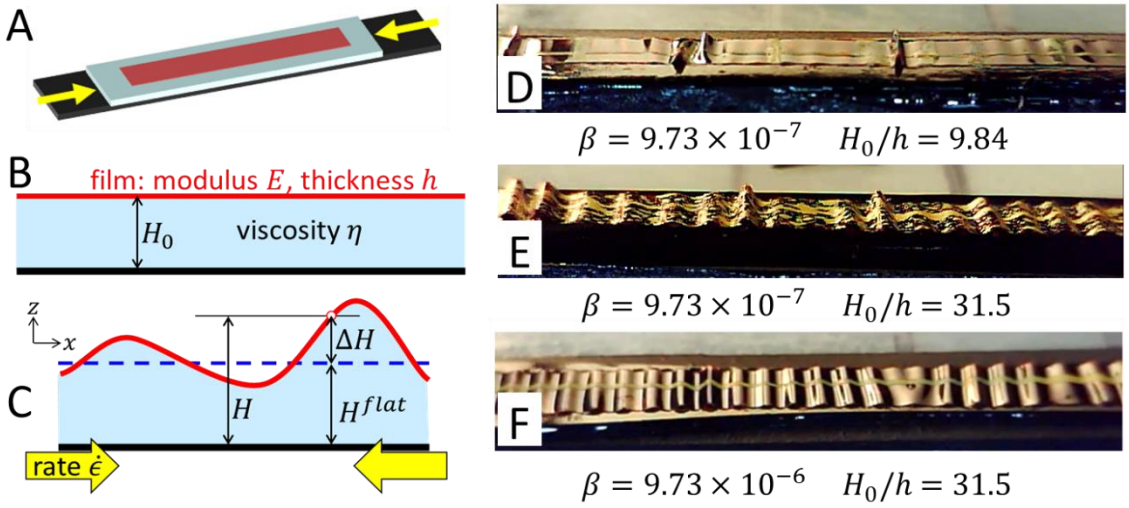

Figure 5.1: A. Schematic of the experiment. A film (orange) is attached to a viscous liquid layer coated onto a pre-stretched rubber strip. The rubber strip is allowed to relax (yellow arrows). B. 2D sketch of geometry before buckling, and C. after buckling. D-F. Experimental images where rate and liquid thickness varies.

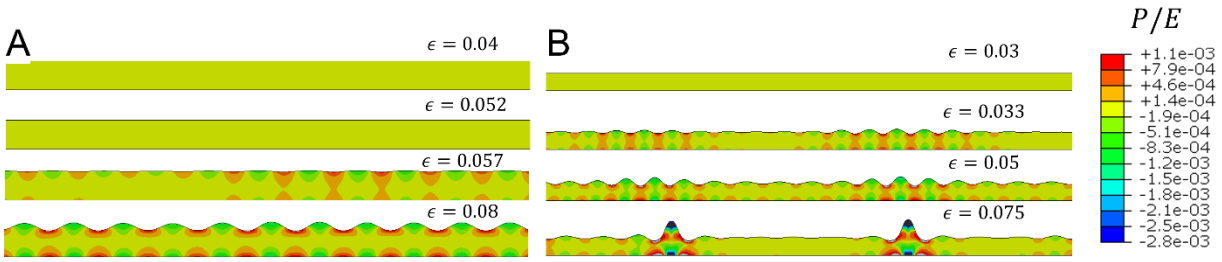

Figure 5.2: Snapshots from A. Wrinkling simulation, and B. Ridge localization simulation, taken at strain values listed on top of each image. Note that a wider region is shown for the ridge localization simulation, making the liquid layer appear thinner. In fact both have the same initial liquid thickness. The color map is the pressure reported by ABAQUS, which is simply the negative mean of the three principal stress.

For quantitative analysis of the simulations, we must isolate film motion that is specifically attributable to buckling. We characterize the film kinematics by two quantities, the x- displacement $u(x,t)$ of a material point on the film from its initial position, and the height $H(x,t)$ of the film, which is also the liquid layer thickness. If the film stayed flat without buckling, these two quantities would follow:

$$u^{flat} = -\dot{\epsilon}xt \quad ; \quad H^{flat} = \frac{H_0}{1-\dot{\epsilon}t} \tag{5.1}$$

The first equation states that x-displacement of the film matches that of the bottom rubber layer. The second is a statement of liquid incompressibility: as strain increases, the film rises to preserve liquid volume, as indicated by the dashed blue line in Fig. 5.1C. Once the film buckles, the local values of u and H deviate from Eq. 4.9, and these deviations are written in normalized form as:

$$\frac{\Delta u}{H_0} = \frac{u - u^{flat}}{H_0} \quad ; \quad \frac{\Delta H}{H_0} = \frac{H - H^{flat}}{H_0} \tag{5.2}$$

We adopt ΔH as the definition of the local buckle amplitude. The spatial gradient $\frac{d\Delta u}{dx}$ is simply the film strain ϵ^f discussed in the previous chapter. Further, the x-direction velocity of the film relative to the rubber layer is $\Delta\dot{u} = \partial_t(\Delta u)$. The importance of this relative x-velocity is explained below.

The red lines in Fig. 5.3 show the evolution of the non-dimensional amplitude profile $\Delta H/H_0$ in the same simulations as the two videos. The onset of buckling is marked by the appearance of non-zero values of $\Delta H/H_0$ at sporadic locations over the film. As expected from visual examination of the videos, at high rate, the buckled region expands until the entire film has roughly sinusoidal height variations. In contrast, at low rate, the buckles become localized so that regions of tall buckles are separated by flat regions.

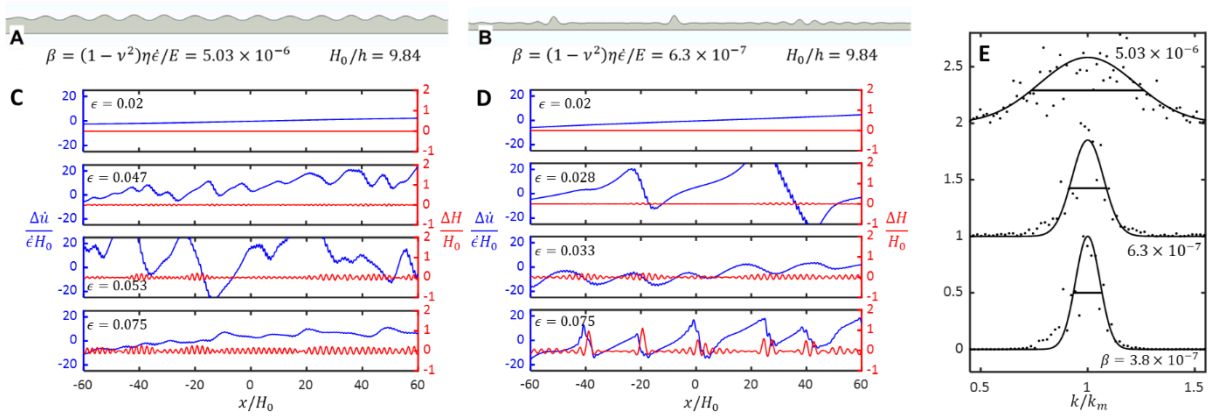

Figure 5.3: A&B: Snapshots of buckled geometry at ϵ =0.075 for the (A) wrinkling and (B) ridge localization simulations at the β and H_0/h values listed. A wider region is shown for B, making the liquid layer appear thinner. In fact, both have $H_0/h = 9.84$. C&D. Evolution of amplitude (red) and x-velocity (blue) profiles in each simulation. (E) Fourier transform of the amplitude profile at threshold and fits to gaussian (see text) where horizontal lines indicate width of the gaussian. The upper two data are moved vertically by 1 and 2 units respectively.

A major goal of this research is to quantify inter-ridge distance. But the lowest image in Fig. 5.1D indicates a complexity: ridge localizations do not necessarily comprise single tall buckles. Instead, there are often two or more adjacent buckles that are comparable to each other, but much taller than their neighbors. Should two neighboring tall buckles should count as a single localized ridge or two? This question can be resolved by examining the x-direction velocity profiles.

We found that inter-ridge distance can be identified reliably from the $\Delta\dot{u}(x)$ profiles, rather than by measuring the distance between the tallest buckles from the amplitude profiles. The blue lines in Fig. 5.3 plot these relative x-velocity profiles in non-dimensional form $\Delta\dot{u}/\dot{\epsilon}H_0$. The first remarkable observation is that in the low-rate simulation, (Fig. 5.3D), while the buckle amplitude is still modest ($\Delta H/H_0 < 0.2$), the $\Delta\dot{u}/\dot{\epsilon}H_0$ develops a long-wavelength

modulation. The modulation is such that the film moves towards locations with relatively large ΔH values; these locations "accumulate film" and grow taller, whereas neighboring regions "supply film" and themselves become flat. With increasing strain, the regions with tall ridges become increasingly narrow, and the velocity profile takes on a sawtooth shape. Yet the wavelength of the modulation and the location of the zeroes in $\Delta\dot{u}/\dot{\epsilon}H_0$ remain pinned throughout. In contrast, at high-rate (Fig. 5.3C), $\Delta\dot{u}/\dot{\epsilon}H_0$ temporarily takes on large values in the vicinity of buckles. But long-range correlations in $\Delta\dot{u}/\dot{\epsilon}H_0$ do not appear, and subsequently all the buckles increase their amplitude uniformly. Thus, the modulation in $\Delta\dot{u}/\dot{\epsilon}H_0$ is a reliable method to find interridge distances; it sidesteps the need to judge which buckles are "tall enough" to be counted as ridges. In particular, the modulation unambiguously shows that the closely spaced pairs of tall ridges evident in Fig. 5.3D constitute an indeed single buckle localization. With this insight about the modulation of x-velocity of the film, the two length scales that characterize the buckling, the wavelength λ, and the interridge distance f, can now be estimated readily which is done below.

The second remarkable observation is that the fact that $\Delta\dot{u} \neq 0$ immediately implies a shear flow in the liquid layer. What is striking is that magnitude of the shear flow far exceeds the applied compression rate. The local shear rate is roughly $\Delta\dot{u}/H \approx \Delta\dot{u}/H_0$. Thus, the quantity plotted in Fig. 5.3C and D, $\Delta\dot{u}/\dot{\epsilon}H_0$ is the ratio of the shear rate to the applied compression rate. For the ridge localization situation of Fig. 5.3D, the highest magnitudes of $\Delta\dot{u}/\dot{\epsilon}H_0$ are about 15, and these coincide with the troughs neighboring the highest amplitudes. I.e. the shear rate in the liquid adjacent to the ridge peak is roughly 15-times larger than the applied compression rate. This estimate is consistent with experiments which indicates a shear rate that is 10-fold higher

than the compression rate. For the wrinkling scenario, the highest values of $\Delta\dot{u}/\dot{\epsilon}H_0$ is 10, a smaller, but still very significant shear flow.

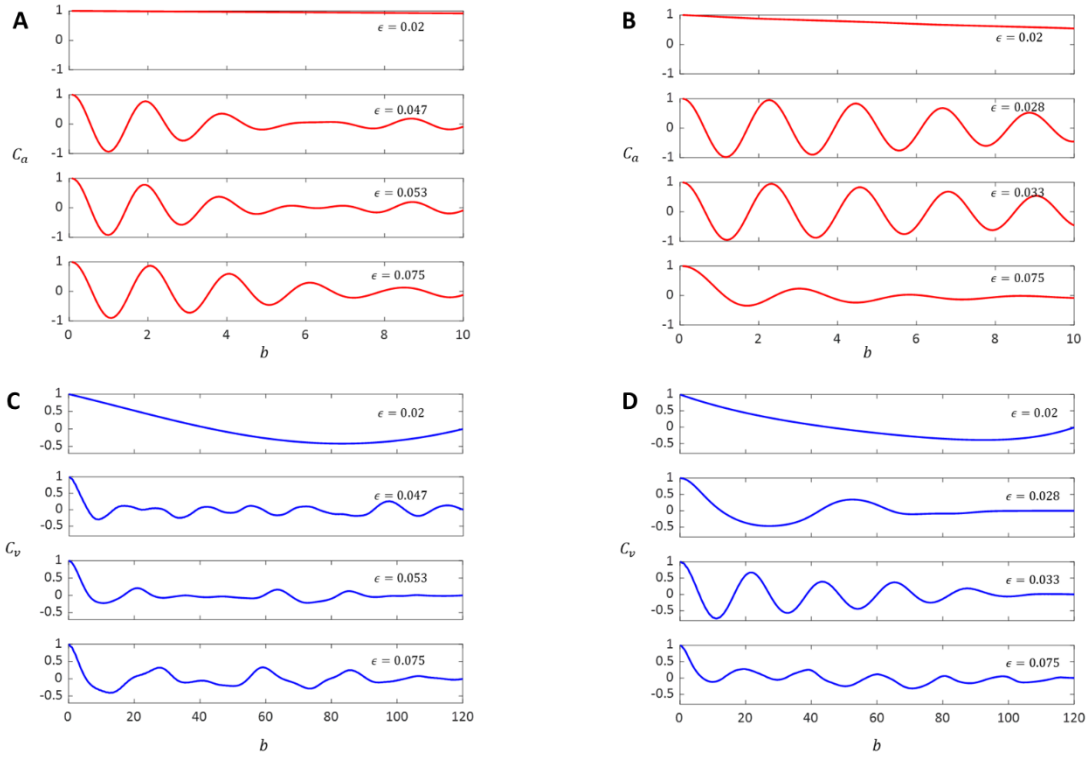

Figure 5.4: A&C: Autocorrelation function of amplitude and velocity of wrinkling simulation which is shown in Figure 5.2A. B&D: Autocorrelation function of amplitude and velocity of wrinkling simulation which is shown in Figure 5.2B.

For this, we calculate the spatial autocorrelation functions C_a for the amplitude and C_v for the velocity, which is shown in Fig. 5.4. C_a always shows a strong first peak at a non-zero distance, followed by several overtones. The location of the first peak is taken as λ. C_v shows a well-defined peak only at low β values or at low H_0/h values. The location of this peak is taken as f. For large values of β or H_0/h, the peak C_v is ill-defined, and hence f cannot be estimated reliably. Visual inspection of the amplitude profiles confirms that in such cases, the amplitude of the tallest ridges no longer dominates over all the others. Accordingly, such cases are deemed to

be in the wrinkled state, and f is not reported. Figure 5.5 shows how λ/H_0 and f/H_0 both vary with increasing rate at fixed liquid thickness (Fig. 5.5A), or with increasing liquid thickness at fixed rate (Fig. 5.5B).

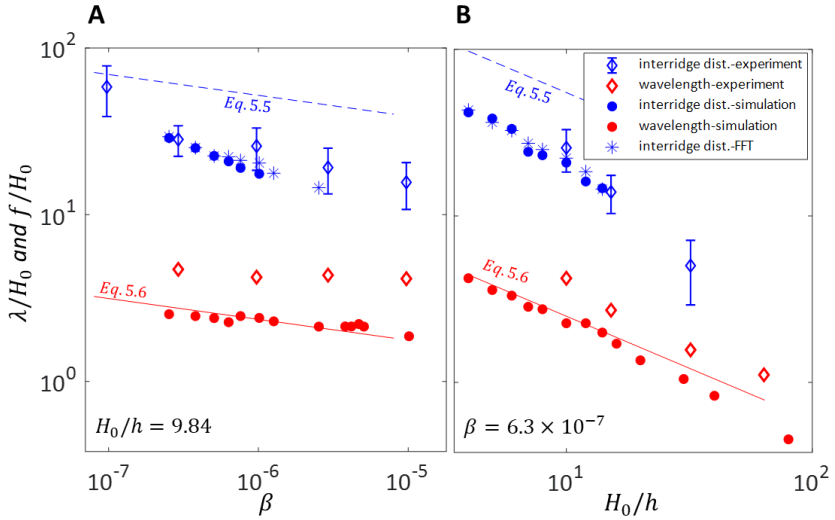

Figure 5.5: Dependence of normalized wavelength and inter-ridge distance on non-dimensional A. rate β, and B. liquid thickness H_0/h. Blue symbols correspond to inter-ridge distance, whereas red symbols to wavelength. The error bars on the experimental f values indicate the range of distances measured. Error bars on the experimental λ values are smaller than the symbols. Some simulations or experiments do not show clear wrinkles or ridges, and therefore the corresponding points do not appear.

Detailed theoretical analysis was conducted collaboratively by Prof. Cerda, University of Santiago, Chile and the lines are predictions of that theory. The theory is the perturbation analysis of Eq. 5.1 based on lubrication approximation. Then the dynamics of the film constrained to deformations in the x-z plane is captured by two given equations:

$$\partial_t u = -H^2 \partial_x p/(2\eta) + H\tau/\eta + \partial_t u^{flat} \tag{5.3}$$

$$\partial_t H = \partial_x[H^3 \partial_x p/(3\eta) - H^2 \tau/(2\eta)] - \partial_x(\partial_t u^{flat})H \tag{5.4}$$

In the analysis, the criterion of instability is that the amplitude of the perturbation must grow by a certain factor, which is the initial unknown perturbations of the system. This certain factor can be determined by fitting simulations. The final predictions[68] for wavelength and interridge distance are as follows,

$$\lambda_c \approx 2\pi H_0 c_2 S_0^{-\frac{1}{8}} (1-v^2)^{-\frac{3}{8}} \beta^{-\frac{1}{8}} \left(\frac{H_0}{h}\right)^{-\frac{5}{8}} \tag{5.5}$$

$$\frac{f}{\lambda} = \left(\frac{96 S_0}{\pi^2}\right)^{-\frac{1}{2}} \tag{5.6}$$

These two equations are shown as straight lines in Fig. 5.5 above. $c_2 = 2^{-\frac{7}{8}} 3^{-\frac{1}{4}} = 0.41$ and $S_0 = 70$.

From the autocorrelation function of amplitude and velocity shown in Fig. 5.4A, a new criterion judging the critical strain to induce ridge localization is proposed. Ridge localization can be captured if the peak C_v is well-defined, vice versa. Then Fig. 4.11, which is the buckling map based on strain rate and strain, can be redrawn with new criterion. The advantage of new criterion is that velocity modulation can be captured even earlier than the localized in amplitude plot.

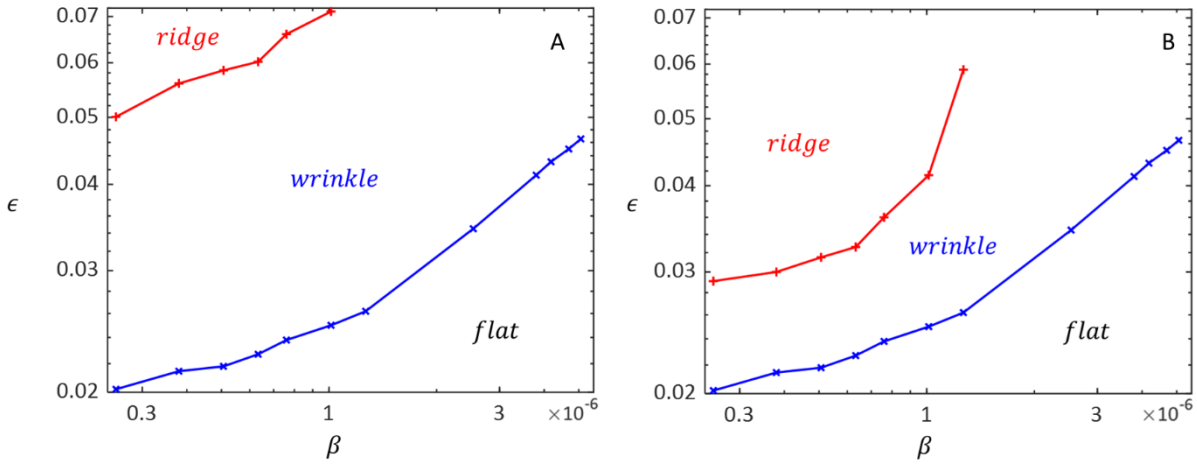

Figure 5.6: Buckling map based on strain in rubber ϵ and strain rate. The blue curve indicates the critical strain to induce buckling as the red curve indicates the critical strain to induce ridge localization. A. p/t criterion, which is same as Fig 4.11. B. velocity modulation criterion.

Finally, we turn to a Lagrangian view of buckles focusing on the motion of material points, i.e. individual nodes of the mesh, and more specifically on how their local motion gives either wrinkles or localized ridges. The time-trajectory (u, H) from ABAQUS tracks the motion of each node in lab coordinates. From this, Eq. 5.2 gives the spatial-trajectory of $(\Delta u, \Delta H)$. The corresponding nodal trajectories $(\Delta u, \Delta H)$, normalized by H_0, are shown in Fig. 5.7. For this plot, a three wavelengths-wide region of film was selected in each simulation. In the wrinkling case Fig. 5.7A, the trajectories are almost sinusoidal with all displacements being nearly vertical. Once a certain node becomes a peak or a trough early during the buckling process, it remains that way. In sharp contrast, Fig. 5.7B shows individual nodes moving towards the central fold with the x- and z-direction displacements being comparable in magnitude. Therefore nodes near the main peak follow highly complex paths, for example, two nodes are highlighted which first become a peak and then a trough, or vice versa. Indeed there are even material points that traverse across the trough (i.e. start on the left of a trough and move to the right of it or vice

versa) while the thickness of the liquid under trough remains at nearly constant height. This further strengthens the schematic picture of Fig. 3.5 that peaks can grow due to lateral motion of the film, without needing much change of the liquid height in the neighborhood of the peak.

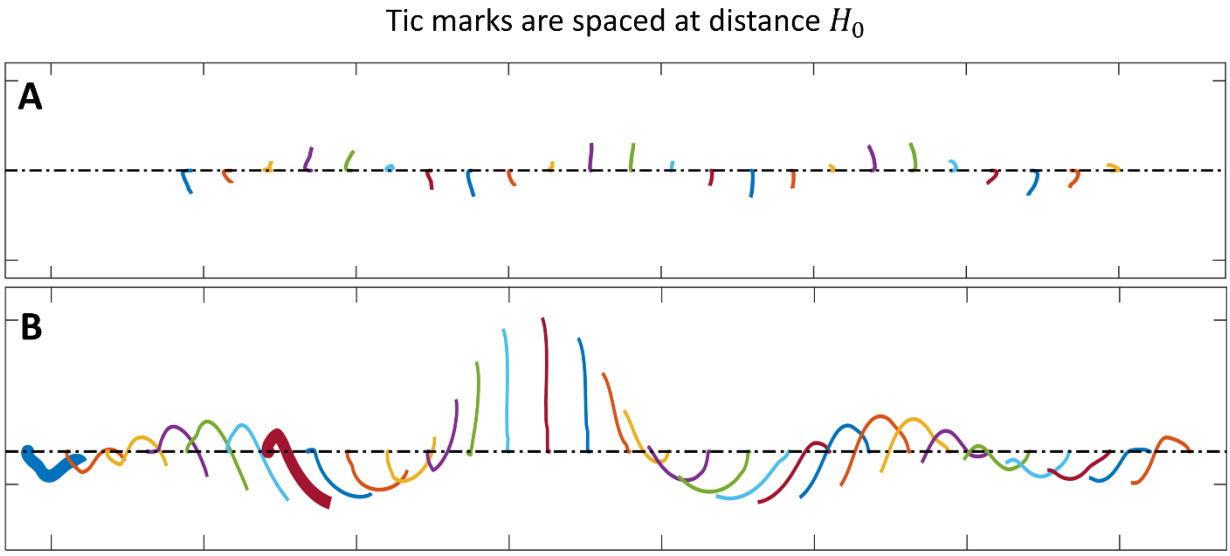

Figure 5.7: Trajectories of material points in the film for A. Wrinkling simulation, and B. Ridge localization simulation. Each line is a trajectory of $\left(\frac{\Delta u}{H_0}, \frac{\Delta H}{H_0}\right)$. The regions selected correspond to roughly three wavelengths in each case. The dot-dashed line passes through the initial position of each node. The two thick trajectories in B show nodes that first become troughs and then peaks, or vice versa.

To summarize, the simulations capture the experimental trends well. Yet, they also bring up several complexities that are not obvious experimentally. (1) Fig. 5.2 shows large pressure gradients along both, the x-direction as well as the thickness direction. (2) The negative pressure under the ridge peaks might serve to make the ridge regions narrower and contribute to high local curvature. (3) In the ridge localization simulation, material points in the film undergo large x-direction motion, with respect to the substrate with a long-wavelength modulation which tracks

ridge localization. (4) Under the troughs neighboring the ridge peaks, the shear deformation is at least an order of magnitude larger than the applied compressive deformation. Some or all of these complexities may be essential ingredients of even a minimal theoretical model. In particular, the last item suggests that motion of the film parallel to the surface is accommodated readily by shear flow in the liquid layer. This may justify a theoretical approach wherein viscous stresses associated with squeezing flow are included, but those associated with shearing are ignored.

6.0 Rate-dependent Creasing of a Viscoelastic Liquid

Portions of this chapter are included in a manuscript by Xianheng Guan, Likhitha Reddipalli, Dylan Butler, Qihan Liu, Sachin Velankar, Rate-dependent creasing of a viscoelastic liquid, submitted to Extreme Mechanics Letters, accepted in May 2022

A homogenous block of rubber, gel, or many other soft elastic materials, shows surface creases under severe compression[17-27,33]. An initially smooth free surface develops sharp cusp-like, self-contacting features once a certain critical strain is exceeded. In contrast, viscous liquids do not show such an instability, and the free surface remains flat under compression, at least as long as viscous effects dominate over any inertial effects. This research is concerned with the intermediate case of viscoelastic materials which have both solid-like and liquid-like characteristics. We quantify viscoelastic creasing by experiment, and establish a theoretical model for the crease forming conditions.

The first theoretical analysis of the compression-induced instability of the free surface of neo-Hookean materials was conducted by Biot[33]. The onset of elastic instability was taken as the strain at which Rayleigh surface wave speed becomes zero. This linear stability analysis predicted that the surface should wrinkle at a compressive strain of $\epsilon_{wrinkle} = 0.46$ under plane strain conditions. However, experiments showed that localized creases, rather than uniform wrinkles, appear at a much lower critical strain $\epsilon_{crease} = 0.35$ [17,18,20]. This value has been reproduced by simulations of a crease, which can be infinitesimal in size but involves a singular strain field around the crease tip [21,38,66,69,70]. Cai et al[19] and Liu et al[21] examined the role of

surface tension in the creasing process. Since creasing distorts the free surface, it increases the surface area as compared to the area expected if the surface remained flat under compression. Accordingly, surface tension penalizes creasing, thereby creating a nucleation barrier for the initiation of creases[18,20]. When surface tension is taken into account, creases can appear at any strain between $\epsilon_{wrinkle}$ and ϵ_{crease}. Defects of sizes larger than the elastocapillary length tend to reduce the creasing strain to values near ϵ_{crease}[21]. In contrast, defects that are small relative to the elastocapillary length become smoothed out due to surface tension and do not induce creasing until the strain approaches $\epsilon_{wrinkle}$. The values of $\epsilon_{wrinkle}$ and ϵ_{crease} depend on the dimensionless ratio γ/GH. Here γ is the surface tension, G is the shear modulus, γ/G is known as the elastocapillary length, and H is the sample thickness. The values $\epsilon_{wrinkle} = 0.46$ and $\epsilon_{crease} = 0.35$ cited above correspond to samples that are much thicker than the elastocapillary length ($\gamma/GH \ll 1$). Further details of creasing in elastic materials, including the effects of geometric variables, inhomogeneity of material properties, and more complex material constitutive behavior have been examined by many researchers[71-79].

Moving beyond purely elastic effects, the role of inelastic deformation was examined by Yang et al. who showed that a material capable of permanent deformation requires a higher strain to develop creases[24]. The role of viscoelasticity, the topic of this research, has not been examined previously.

Intuitively one may expect that the free surface of a viscoelastic liquid should show creasing, but only if the compression rate is sufficiently high that the fluid deformation is substantially elastic in nature. On the other hand, at rates that are sufficiently low that the liquid can relax elastic stresses almost completely, creases are not expected. In fact, such a rate-dependent creasing instability can be demonstrated readily with Silly Putty™, a familiar

viscoelastic fluid (Fig. 6.1). At high deformation rates, Silly Putty behaves as an elastomer, for example, bouncing like a ball when dropped onto a surface, or snapping like a rubber band if stretched rapidly. However Silly Putty flows like a viscous liquid at low loading rate, for example spreading into a puddle when left undisturbed on a horizontal surface. In fact, all materials have viscoelastic properties, although the timescales of viscoelasticity are often too short or too long for observation. Silly Putty is convenient because it has a relaxation time of a few seconds, thus, viscoelastic creasing can be illustrated with crude "hand" experiments as shown in the supplementary video file (Hand experiment.mp4). For the illustrative experiment of Fig. 6.1, a long cylinder of Silly Putty was laid onto a strip of silicone rubber and allowed to relax and spread under gravity into a long puddle with a smooth surface typical of a liquid. The rubber strip was then stretched, held for roughly 30 s to allow stress relaxation of the Silly Putty, and then unloaded. If unloaded slowly, the free surface of the Silly Putty remains nearly flat with only weak distortions. Rapid unloading caused the free surface to develop deep self-contacting furrows that strongly resemble creases in elastomers.

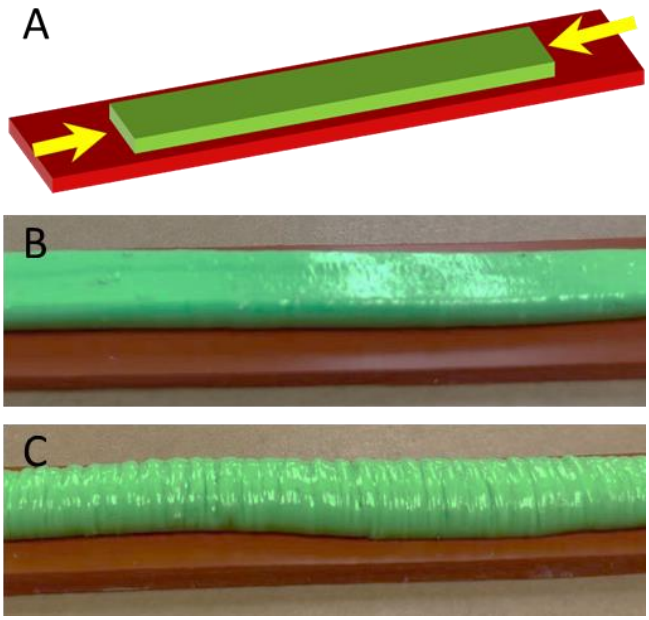

Figure 6.1: Creases in Silly induced by compression of the rubber sheet supporting it.

A. 3D schematic of the hand experiment. Images after compression at B. low rate C. high rate.

6.1 Experimental results

Creasing is known to be highly sensitive to defects[48]. Most formulations of Silly Putty are believed to contain particles, which may act as defects, and hence Silly Putty is less suitable for experiments. Therefore, experiments were conducted on Oppanol B15, a polyisobutylene of molecular weight of roughly 75 kg/mol (as per the manufacturer, BASF). Fig. 6.2 shows the oscillatory moduli of the fluid measured in the linear viscoelastic region using an Anton Paar MCR-302 rheometer in a 25 mm parallel plate geometry. As may be expected for a polydisperse molten polymer, the relaxation spans several decades in frequency. To a first approximation, the crossover between the storage modulus G' and the loss modulus G'' marks the transition between

solid-like and liquid-like behavior. This crossover appears at a frequency of 0.20 rad/s, corresponding to a timescale of 5.0 s.

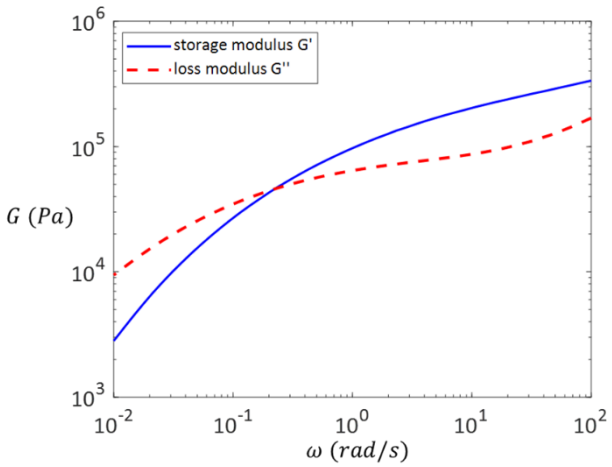

Figure 6.2: The oscillatory moduli of the viscoelastic liquid Oppanol B15.

The PIB was placed onto a silicone rubber (Sylgard 184) substrate and allowed to spread under gravity at 45℃ to obtain a thick sheet of PIB. A sample of several mm dimension was cut from this sheet. Since adhesion between PIB and silicone rubber is very weak, this cut piece could be peeled off readily, weighed, and then immediately placed onto a strip of natural rubber. It was then further allowed to spread for 8 hours at 65℃ into a layer of thickness ~1 mm. The rubber strip was then mounted onto the stretching/compression apparatus. At no point during this procedure did the free surface touch any other surface, thus avoiding any defects at the free surface which may affect the creasing.

The stretching/compression apparatus, shown schematically in Fig. 6.3, consists of two counter-rotating cylinders to whose surface the rubber strip was clamped. The rubber strip was folded along its long direction so that the surface of the sample faced sideways (Fig. 6.3A and B). This allowed an unimpeded sideview of the free surface using a downward-pointed camera. Despite the fact that the free surface of the sample is vertical, the sample undergoes negligible

flow during the experiment owing to its high viscosity. Moreover, in the middle section, the radius of curvature of the rubber strip is at least 10-fold larger than the sample thickness. Rotation of the cylinders was controlled by two stepper motors. The cylinders were rotated manually until the rubber strip was slightly taut. The cylinders were then rotated by the motors so that the strip was stretched between the cylinders, thus forcing the PIB viscoelastic liquid to stretch as well. The system was then held for at least 5 min. This initial state serves as the relaxed state for the fluid. The cylinders were then permitted to counterrotate, allowing the rubber strip to recoil, and therefore compressing the viscoelastic fluid layer. The circumferential velocity of the cylinders ranged from 0.13 mm/s to 120 mm/s. Since the distance between the cylinders is fixed, the nominal compression rate is simply the ratio of the circumferential velocity of each cylinder to half of the distance between the cylinders. In all cases, at the end of the compression, the rubber strip remained in tension to avoid it from going slack. Further, the adhesion of PIB to natural rubber is relatively strong, and hence the PIB did not delaminate in these experiments. The strain was measured by tracking marker particles placed on the rubber surface. This strain rate was found to be within a few percent of the nominal strain rate obtained from the ratio of the cylinder surface velocity to the inter-cylinder distance. The compressive strain during this step, and the corresponding compression rate, were the two parameters varied experimentally.

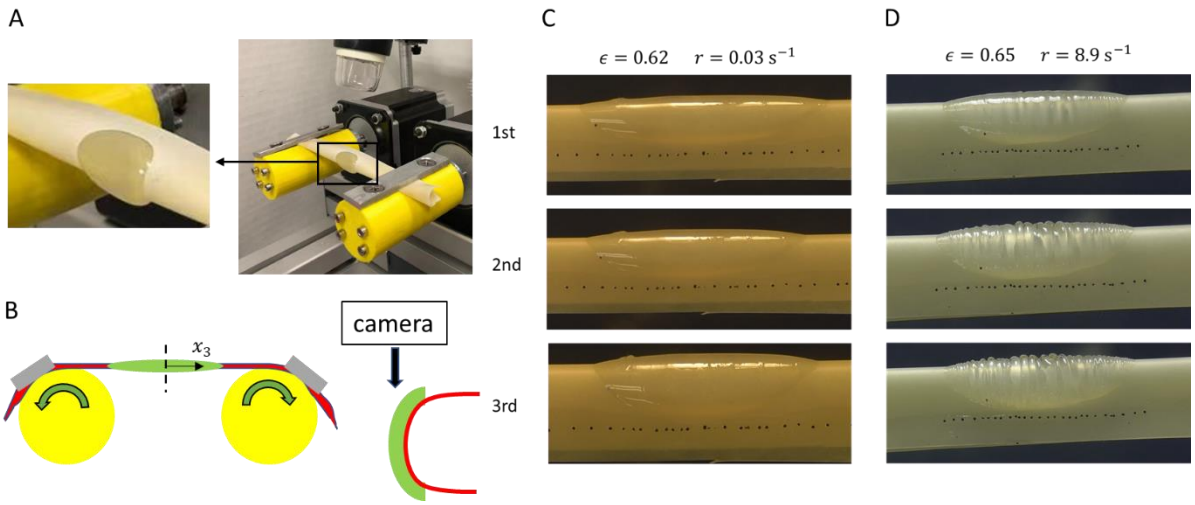

Figure 6.3. A. The stretching/compression apparatus. The magnified image on the left shows the sample more clearly. B. Schematic of the setup. The right hand cartoon illustrates a cross-section of showing how the free surface of the sample is curved, allowing a clear view of the free surface. C. Images of the samples after low rate compression, and D. after high rate compression. From top to bottom, samples were subjected to one, two, or three compression cycles respectively. This set of experiments is done with the help from undergraduate researcher Likhitha Reddipalli in our group.

Figs. 6.3C and 6.3D show the appearance of the sample after releasing at low and high strain rates respectively. The surface remains nearly flat when unloaded at a low rate, but becomes distorted after a high rate unloading. Yet, the creases in the top image of Fig. 6.3D are not as sharp as seen in typical elastic systems after stretching and compressing[22], and hence it is difficult to judge whether the sample is creased or not. To enable a clearer classification between creased and flat states, we therefore applied three stretching-compression cycles with a 5 min duration between cycles, and a strain rate of $0.044s^{-1}$ during stretching. Creasing is a localized surface instability and sensitive to defects[22]. Therefore, the slight distortions generated during the first cycle act as defects in the next cycle, and the depth of crease increases rapidly. Note that the

5 min waiting time far exceeds the ~5 s timescale for the crossover in Fig. 2, and hence erases memory of past cycles; multiple cycles only serve to amplify the creases. While the rate dependence of the instability is clear even after the first compression (top images in Fig. 6.3 C vs D), three cycles allow a more unambiguous determination of whether the surface is stable to compression or not. Incidentally cyclic tension/compression can lead to a different kind of stripe pattern comprising alternate peaks and troughs aligned perpendicular to the tension/compression direction[80]. Although those stripe patterns were visually somewhat similar to Fig. 6.1 B, their phenomenology and mechanism was entirely different. In that case the materials were not viscoelastic liquids, but plastic liquids with a yielding behavior; stripe formation was driven by strain localization in the troughs; residual stress between cycles was crucial to the phenomenon; and rate of deformation affected the stripe formation only weakly.

Experiments such as in Fig. 6.3 allow creating the map (Fig. 6.4) of creased vs flat states as the strain ϵ and strain rate r is changed. In samples marked as “creased”, the free surface has relatively sharp creases at many locations along the surface after three cycles. In samples marked as “flat”, the free surface remains nearly flat after three cycles. Additional experiments conducted at strains lower than the blue circles in Fig. 6.4 also showed a flat state and are not shown in Fig. 6.4.

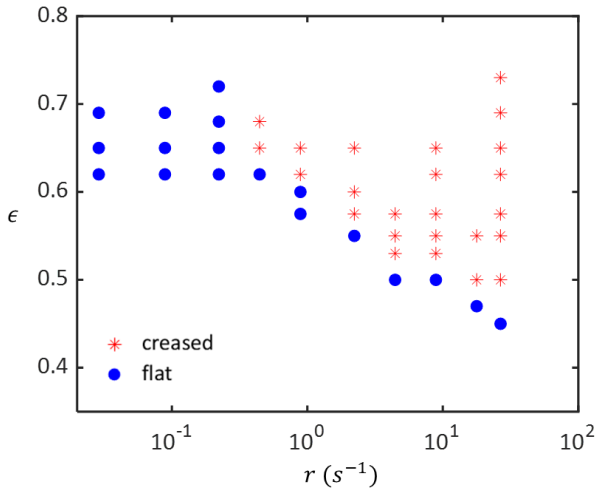

Figure 6.4. Map of viscoelastic creasing determined experimentally.

In this study, experimental compression rates range from 0.02 s^{-1} to 30 s^{-1}, and crease appear only at rates exceeding 0.4 s^{-1}. From Fig. 6.2, in the frequency range from 0.02 rad/s to 30 rad/s, the shear modulus $G{\sim}10kPa$ or higher. The surface tension of PIB [81] is $\gamma{\sim}$0.03 N/m, and hence the elastocapillary length γ/G is on the order of 1 μm. Therefore at our sample thickness of $H{\sim}$1mm, γ/GH is on the order of 10^{-3}. At such small values of $\gamma G/H$, elastocapillary effect has negligible influence on $\epsilon_{wrinkle}$ and ϵ_{crease}. Accordingly, $\epsilon_{wrinkle}$ =0.46 and ϵ_{crease}=0.35 will be assumed. Indeed Fig. 6.4 shows that at high strain rate ($r{\sim}10^2\ s^{-1}$), the transition between crease states and flat states happens between $\epsilon_{wrinkle}$ and ϵ_{crease}. This is in agreement with our hypothesis that viscoelastic liquid behaves like elastic material when strain rate is sufficiently high.

6.2 Theoretical model

The goal of this section is to develop a viscoelastic creasing criterion, i.e. a prediction for the critical strain $\epsilon_{c,ve}$ for creasing that depends on the compression rate. In viscoelastic liquids such as Oppanol B15 and Silly Putty, only a part of the deformation is elastic. We hypothesize that only this elastic part of the deformation controls creasing behavior. In this section we first develop a constitutive model that is equivalent to the upper-convected Maxwell model commonly used for viscoelastic liquids [82], but in a form suitable for crease analysis. Then we derive a viscoelastic creasing criterion based on the model.

The total deformation of a material can be represented by a deformation gradient $\mathbf{F}$ that maps from an unperturbed reference state to the deformed current state. For a viscoelastic liquid, part of the deformation is elastically recoverable, while the rest of the deformation is an unrecoverable viscous flow. Consequently $\mathbf{F}$ can be decomposed into the elastic and the viscous part as $\mathbf{F} = \mathbf{F}_e\mathbf{F}_v$, Fig.6.5B. Here $\mathbf{F}_e$ represents the elastic deformation, which microscopically corresponds to stretching the polymer chains without shifting the relative positions between chains. $\mathbf{F}_v$ represents the viscous flow, which microscopically corresponds to the relative sliding between the polymer chains without deforming them.

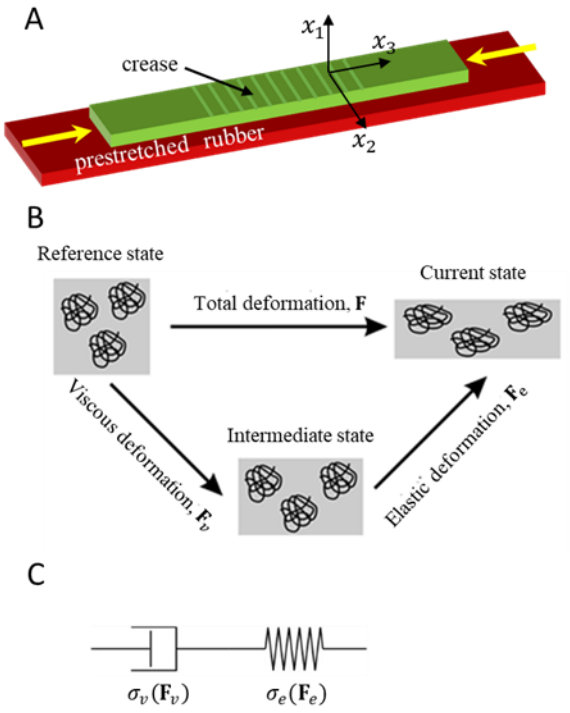

Figure 6.5 A. 2D schematic of the experimental system, and the coordinate directions used in the model. The x_2 direction is taken as out-of-plane of this diagram. B. The deformation of a polymer melt or polymer solution can be decomposed into the viscous part and the elastic part. The viscous part consists of the relative sliding between neighboring polymer chains without deforming the chains. The elastic part consists of stretching the polymer chains while keeping the relative positions of the chains fixed. C. A Maxwell model where the viscous deformation F_v generates a viscous stress and the elastic deformation F_e generates an equal elastic stress.

As a simple viscoelastic material model, we assume that the elastic deformation $\mathbf{F}_e$ stretches each chain affinely and each polymer chain behaves like a Gaussian chain under stretch. Consequently, the elastic deformation generates a stress according to the neo-Hookean model[83]:

$$\boldsymbol{\sigma}_e = NkT(\mathbf{F}_e\mathbf{F}_e^T - \mathbf{I}) \tag{6.1}$$

Here N is the number of polymer chains per volume, k is the Boltzmann constant, and T is the thermodynamic temperature. In the intermediate state in Fig. 6.5B, polymer chains are in their stress-free relaxed state. For the viscous deformation $\mathbf{F}_v$, we assume that the sliding between chains generates a stress following Newton's law of viscosity:

$$\boldsymbol{\sigma}_v^* = NkT\tau\left(\dot{\mathbf{F}}_v\mathbf{F}_v^{-1} + \mathbf{F}_v^{-T}\dot{\mathbf{F}}_v^T\right) \tag{6.2}$$

Here τ is the relaxation time of the polymer chain, and the quantity $NkT\tau$ is the viscosity. Note that a polymer chain has a distribution of relaxation times[83], whereas we only consider a single relaxation time in our model. The stress in Eq. 16 corresponds to the intermediate state. Transforming it to the current state[84]:

$$\boldsymbol{\sigma}_v = NkT\tau\mathbf{F}_e\left(\dot{\mathbf{F}}_v\mathbf{F}_v^{-1} + \mathbf{F}_v^{-T}\dot{\mathbf{F}}_v^T\right)\mathbf{F}_e^T \tag{6.3}$$

We assume that the viscous and the elastic parts of the deformation interact as in a Maxwell model, Fig. 6.5C, which gives the microscopic force balance:

$$\boldsymbol{\sigma}_v = \boldsymbol{\sigma}_e \tag{6.4}$$

The Supplementary Material shows that Eqs. 11-14 constitute a nonlinear viscoelastic model equivalent to the upper-convected Maxwell model.

Upon substituting $\mathbf{F}_v = \mathbf{F}_e^{-1}\mathbf{F}$, Eqs. 11-14 can be combined to obtain a first order ordinary differential equation for the evolution of the elastic part of the deformation:

$$\mathbf{F}_e\mathbf{F}_e^T - \mathbf{I} = \tau\left(\mathbf{F}_e\dot{\overline{\mathbf{F}_e^{-1}}}\mathbf{F}_e\mathbf{F}_e^T + \mathbf{F}_e\mathbf{F}_e^T\dot{\overline{\mathbf{F}_e^{-T}}}\mathbf{F}_e^T + \dot{\mathbf{F}}\mathbf{F}^{-1}\mathbf{F}_e\mathbf{F}_e^T + \mathbf{F}_e\mathbf{F}_e^T\mathbf{F}^{-T}\dot{\mathbf{F}}^T\right) \tag{6.5}$$

For any given deformation history $\mathbf{F}(t)$, this equation can be solved to obtain $\mathbf{F}_e(t)$.

Before proceeding, we note that Eq. 19 has a single material parameter characterizing the time dependence, the relaxation time τ. Since the deformation of interest in this research is uniaxial compression at rate r, we can immediately render this rate non-dimensional as $w = r\tau$

where w is the Weissenberg number. The limiting cases of $w \ll 1$ and $w \gg 1$ correspond to viscous-dominated and elastic-dominated regimes respectively.

Following the geometry and coordinate system of Fig. 6.5A, the material is uniaxially-compressed in the x_3 direction. The corresponding deformation gradient $\mathbf{F}$ is:

$$\mathbf{F}(t) = \begin{bmatrix} (1-\epsilon)^{-\frac{1}{2}} & 0 & 0 \\ 0 & (1-\epsilon)^{-\frac{1}{2}} & 0 \\ 0 & 0 & 1-\epsilon \end{bmatrix} \tag{6.6}$$

where $\epsilon = 1 - e^{-rt}$ relates the nominal strain to the time. Note that Eq. 20 and all subsequent equations are written in terms of nominal strain ϵ, and hence $\epsilon \to 1$ corresponds to an infinite degree of compression. Substituting Eq. 20 into Eq. 19, and integrating the resulting ODE (see Appendix E) yields $\mathbf{F}_e$ as a diagonal matrix with diagonal components $(\lambda_{e1}, \lambda_{e2}, \lambda_{e3})$ where:

$$\lambda_{e1} = \lambda_{e2} = \left(\frac{1 - w(1-\epsilon)^{\frac{1-w}{w}}}{1-w} \right)^{\frac{1}{2}} \tag{6.7}$$

$$\lambda_{e3} = \left(\frac{1 + 2w(1-\epsilon)^{\frac{1+2w}{w}}}{1+2w} \right)^{\frac{1}{2}} \tag{6.8}$$

These λ_e values represent the elastic portion of the stretches experienced by the viscoelastic fluid.

Insight into the viscoelastic creasing can be obtained by examining the elastic energy density U stored in the material under uniaxial deformation:

$$U = \frac{1}{2} NkT(\lambda_{e1}^2 + \lambda_{e2}^2 + \lambda_{e3}^2 - 3) \tag{6.9}$$

Fig. 6.6 plots the evolution of elastic energy density with applied strain for various values of Weissenberg number. For the elastic limit of $w \to \infty$, Eqs. 15 and 16 approach $\lambda_{e1} \to$

$(1-\epsilon)^{-1/2}$ and $\lambda_{e3} \to 1-\epsilon$, which are simply the values of the uniaxial stretches applied on the sample. In this elastic limit therefore, Eq. 23 approaches the familiar expression defining the strain-energy relationship of incompressible neo-Hookean solid. In the other extreme of $w \to 0$, the λ_e values obtained from the left hand side of Eqs. 15 and 16 approach 1, and hence $U \to 0$ for all strains. This is consistent with the idea that no elastic energy is stored during low-rate deformations. For intermediate values of w, two behaviors are possible. For $w > 1$, the elastic energy density increases monotonically with strain. For $w < 1$, the elastic energy increases, and then approaches a limiting value which can be obtained by setting $\epsilon \to 1$ (i.e. infinite compression) into Eq. 21 and 22. Fig. 6.6 therefore provides the following physical explanation as to why viscoelastic creasing is rate-dependent. At sufficiently low values of w, no matter how large the applied strain, the viscoelastic material accumulates only a finite level of elastic deformation which may not be sufficient to cause creasing. At sufficiently high w values, the elastic energy increases without bound and hence all elastic phenomena, including creasing, must appear upon sufficient compression.

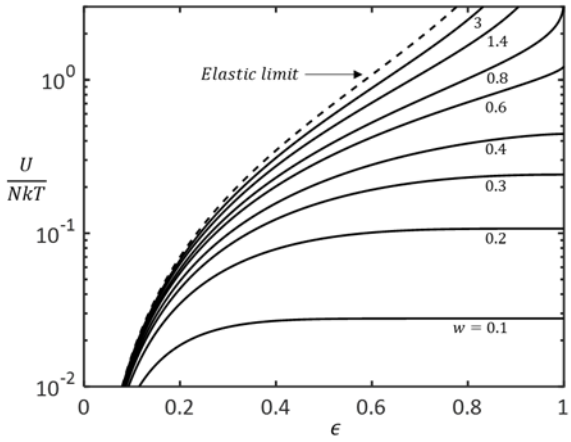

Figure 6.6. Evolution of normalized elastic energy U/NkT during compression at various values of Weissenberg number w.

Although Fig. 6.6 provides physical insight into why creasing occurs, the energy analysis does not directly predict the critical strain $\epsilon_{c,ve}$ for creasing. For a uniformly deformed incompressible neo-Hookean material, the creasing criterion is given by [19,69]:

$$\frac{\lambda_3}{\lambda_1} < \left(1 - \epsilon_{c,e}\right)^2 \tag{6.10}$$

Here λ_1, λ_2, λ_3 are the principal stretches of elastomer, and the crease is aligned parallel to the x_2 direction as illustrated in Fig. 6.5A. $\epsilon_{c,e}$ is the critical strain to induce creasing of a neo-Hookean elastic material under plane strain conditions. As discussed in the Introduction, the limiting values of $\epsilon_{c,e}$ are $\epsilon_{c,e} = \epsilon_{wrinkle}$ for a defect-free sample, and $\epsilon_{c,e} = \epsilon_{crease}$ for a sample with relatively large defects.

We hypothesize that only the elastic deformation of a viscoelastic liquid is responsible for crease formation. Consequently, the crease criterion for the Maxwell fluid would be applying Eq. 16 using λ_e's:

$$\frac{\lambda_{e3}}{\lambda_{e1}} < \left(1 - \epsilon_{c,e}\right)^2 \tag{6.11}$$

The left hand side of Eq. 23 is an explicit analytical function of ϵ and w, and hence Eq. 15 is the desired criterion for rate-dependent creasing. At any specified value of w, a viscoelastic fluid develops creases at the strain $\epsilon_{c,ve}$ at which Eq. 23 is first satisfied during compression.

The application of Eq. 23 to obtain the critical condition for creasing is illustrated in Fig. 6.7A. The solid green curve is $\lambda_{e3}/\lambda_{e1}$ drawn at a fixed Weissenberg number ($w = 2$ is shown in Fig. 6.7A for illustration). The horizontal lines correspond to the limiting cases of $(1 - \epsilon_{wrinkle})^2$ and $(1 - \epsilon_{crease})^2$. The intersection of the green curve with these horizontal lines identifies the creasing strain for the viscoelastic fluid in the wrinkle and crease limit respectively. Repeating this calculation at various values of w yields the two curves marking the lower and upper bounds for crease formation, shown by the dashed and solid black curves in Fig. 6.7B.

In the limit of high w, Eq. 25 reverts to the limit of a neo-Hookean solid in uniaxial compression, for which creases appear between a compressive strain of 0.56 (wrinkle limit) and 0.44 (crease limit), in agreement with existing literature.[19] For w below a certain critical value of w_c, Eq. 25 cannot be satisfied at any strain and hence creases cannot appear. The critical value, w_c, can be obtained by letting nominal strain approach 1 in Eq. 25, which corresponds to compressing the material to an infinite extent. The limiting values for w_c are found to be 0.78 (wrinkle limit) and 0.61 (crease limit).

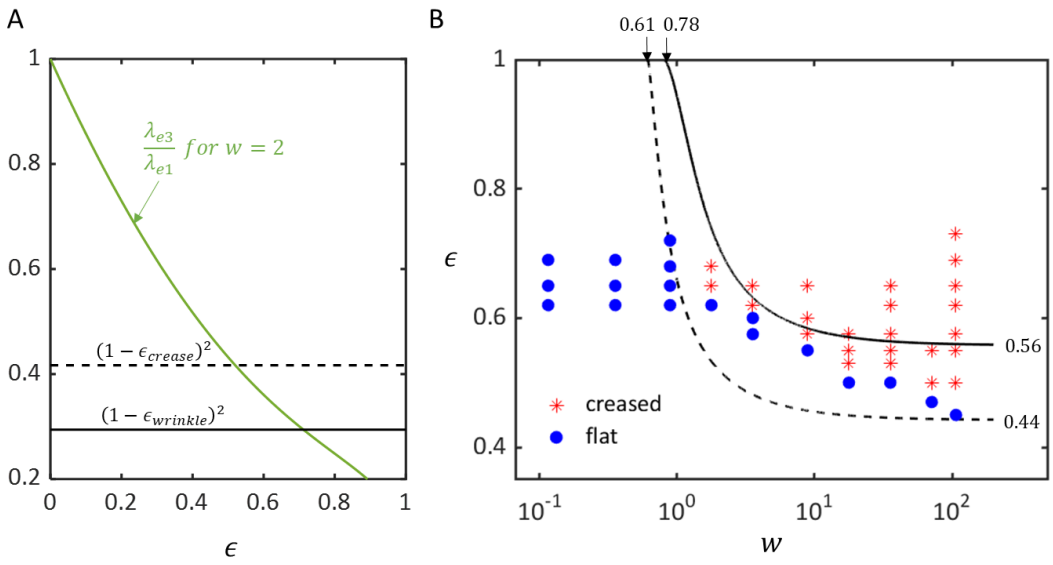

Figure 6.7. A. Solid green line is the evolution of $\lambda_{e3}/\lambda_{e1}$ for the selected value of $w = 2$. The inersections of the green line with the two horizontal lines are the critical strains $\epsilon_{c,ve}$ for viscoelastic creasing based on setting $\epsilon_{c,e}$ to either $\epsilon_{wrinkle}$ or ϵ_{crease}. B. Map of viscoelastic creasing. Solid and dashed curves are $\epsilon_{c,ve}(w)$ as per the creasing or the wrinkling criterion. Points are the same experimental data as Fig. 6.4, made non-dimensional using $\tau = 5s$.

A comparison between the theoretical prediction and the experimental data requires choosing a relaxation time τ to render the experimental measurements non-dimensional. We use the time $\tau = 5\ s$ associated with the crossover in G' and G'' from Fig. 6.2. With this choice and no fitting parameters, Fig. 6.7B shows that the experimentally measured transition between wrinkle and crease falls entirely between the wrinkle limit and the crease limit predictions. Indeed with any choice of τ ranging from 2.5 s to 5.2 s, the experimental data fall between the two theoretical limits.

6.3 Conclusion

In summary, we have examined the crease in a homogenous viscoelastic liquid under uniaxial steady-rate compression. The creasing instability has been well-studied for fully-elastic solids such as rubbers or crosslinked gels, but heretofore, the creasing behavior of a viscoelastic liquid was altogether undocumented. Experiments were conducted using a molten (i.e. solvent-free) polymer as the viscoelastic fluid. The strain required for creasing was found to increase as the compression rate reduced. In the limit of high rate, the creasing strain was found to be comparable to that for a purely-elastic solid.

We have developed an analytical model for viscoelastic creasing in which an upper-convected Maxwell liquid is subjected to uniaxial compression at a fixed rate. The total deformation of the viscoelastic material was decomposed into a viscous part and an elastic part. The creasing criterion known from the past literature for elastic solids was applied to the elastic portion of the deformation. This yielded an analytical criterion in which the strain for viscoelastic creasing increased with a decrease in Weissenberg number. Notably, the model predicts that creasing is not possible at all if the Weissenberg number is below some critical value.

7.0 Future Works

In this chapter, we will discuss some ideas or directions that were attempted during the thesis research, but some of them are not taken to completion.

7.1 Elastoviscous length

In chapter 5, we discussed the dominant parameters which can affect the buckling behavior of thin film floating on viscous liquid. For example, wrinkles are favorable under high compressive rate or thick liquid thickness while localized ridges are more favorable under low compressive rate or thin liquid thickness. Similarly, a long film can easily buckle or show localized ridges when a short film can hardly buckle. However, all parameters mentioned above are considered individually and never combined. Thus, we considered defining a combination of parameters , the elastoviscous length. Then we assigned a symbol ℓ to the elastoviscous length.

$$\ell = \left(\frac{B}{\eta\dot{\varepsilon}}\right)^{\frac{1}{3}} \tag{7.1}$$

where bending stiffness $B = \frac{1}{12}Eh^3$

. T eq. above implicitly assumes that the film can be treated as a 2D membrane and defined by a single parameter B (rather than modulus E and thin film thickness h separately).

This is justified because In experiments or simulations, the thickness of thin film is much smaller than liquid, I.e. $H_0/h \gg 1$, and further, the reciprocal of the curvature of the film is always much smaller than the thickness h. Then for infinitely long films, there are only two lengthscales in the problem: ℓ and H_0. H_0/ℓ is now a dimensionless parameter which may be regarded as a non-dimensional liquid thickness

$$non - dimensional\ liquid\ thickness = \frac{H_0}{\ell} = \frac{H_0}{\left(\frac{B}{\eta\dot{\varepsilon}}\right)^{\frac{1}{3}}} = H_0\left(\frac{\eta\dot{\varepsilon}}{B}\right)^{\frac{1}{3}} \tag{7.2}$$

For infinitely long films, no other parameters are possible, thus the entire buckling process should be captured by this single parameter! Obviously, this approach has merit only if we think of the film as a membrane without any gradients in the thickness direction.

To test the idea that this single parameter can capture the entire buckling process, we conducted three sets of simulations which varied the rate, the liquid thickness while holding fixed H_0/ℓ values. The corresponding profiles are shown in the following figure.

H_0/ℓ = 0.27 is defined as thin liquid layer. These simulations show ridge localization under some circumstances. H_0/ℓ = 0.81 is defined as intermediate liquid layer. No ridge localization is seen.

H_0/ℓ = 2.4 is treated as thick liquid layer. No ridge localization is seen, but the profiles become a bit irregular at long times. But these are rather high strains and it might also be due to wrinkle coalescence, so we should probably not focus on these irregular profiles.

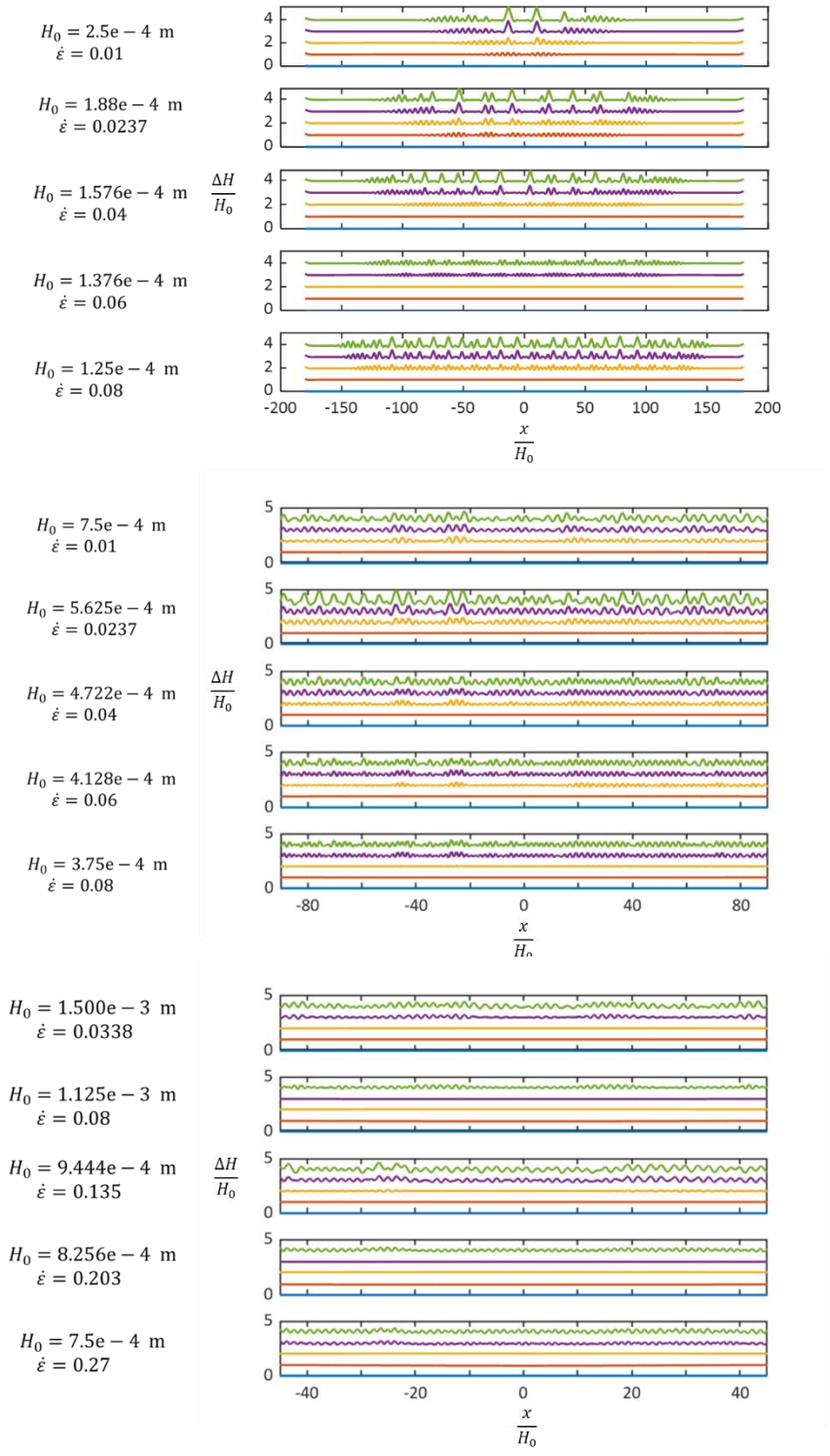

Figure 7.1: Buckling profile when $\frac{H_0}{\ell} = 0.27, \frac{H_0}{\ell} = 0.81, \frac{H_0}{\ell} = 2.4$. Each plot is made at strain $\epsilon = 0, 0.19, 0.38, 0.56, 0.75$, from bottom to top.

As expected, the effect of increasing rate is qualitatively similar to that of increasing H_0. Either a large H_0 value or a large $\dot{\epsilon}$ will make the dimensionless parameter larger and the film will likely buckle into wrinkles. On the other hand, a small H_0 value or a small $\dot{\epsilon}$ will make the dimensionless parameter smaller and the film will likely buckle into localized ridges. This is consistent with the observations from experiments and simulations.

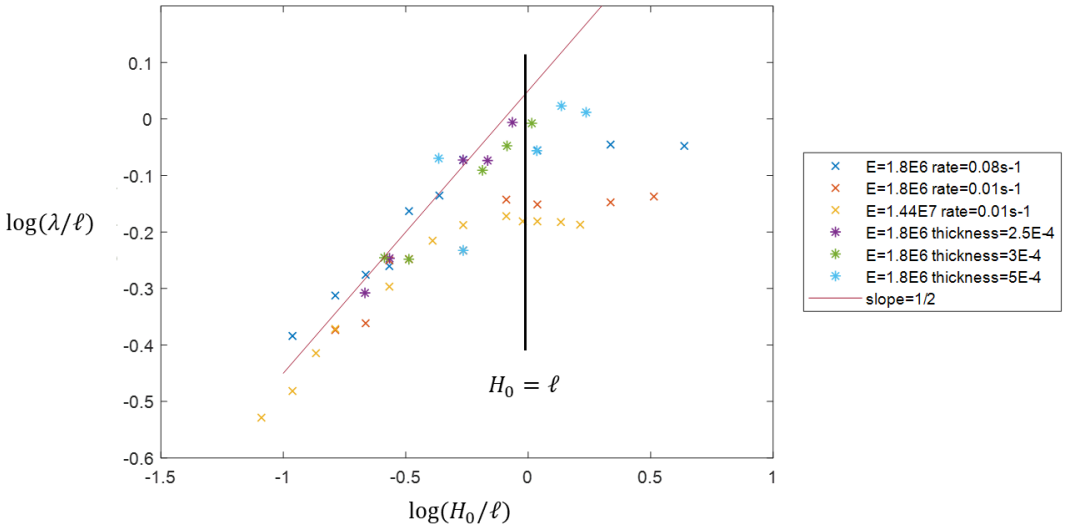

Figure 7.2: The relationship between normalized wavelength and liquid thickness.

Fig 7.2 is a plot of wavelength vs. liquid thickness across a wider range of simulations which vary rate, thickness, and film modulus to access a wider range of elastoviscous lengths . When $H_0 \ll \ell$, I.e. thin liquid limit, the fitting slope is approximately 0.5, which indicates that $\frac{\lambda}{\ell} \sim \left(\frac{H_0}{\ell}\right)^{0.5}$. Then λ will be proportional to $\beta^{-\frac{1}{6}} H_0^{\frac{1}{2}}$, which is close to Dr. Cerda's prediction[68] ($\lambda \sim \beta^{-\frac{1}{8}} H_0^{\frac{3}{8}}$). obtained by an entirely different approach. $H_0 \gg \ell$ (thick limit), we expect that the buckling behavior will not depend on the liquid thickness However, this expectation is not met $\frac{\lambda_{OBJ}}{\ell}$ still depends somewhat on liquid thickness.

In conclusion, the scaling for wavelength from thin limit simulations are not too far with Dr. Cerda's theory[68]. More importantly, at least in the thin limit, data from different simulations collapse onto each other approximately suggesting that $\frac{H_0}{\ell}$ is a reasonable parameter to capture the buckle wavelength in the thin limit. However, this approach did not lead to any other good insights beyond that yet. Certainly except for wavelength, the remaining buckling characteristics are not preserved even when $\frac{H_0}{\ell}$ is held fixed. It seems that the ratio of liquid thickness and elastoviscous length is not the right dimensionless parameter controlling the buckling behavior.

The failure of this approach is puzzling. For thin films which may be treated as membranes with a bending modulus, dimensional analysis does not permit any variable other than $\frac{H_0}{\ell}$ to be defined. The fact that the buckling data do not collapse may be an indication that behavior of the film prior to buckling may have large effects. Specifically, the critical strain cannot be predicted by treating the film as a membrane, and this may affect buckling behavior significantly.

More simulations need to be conducted to assess whether elastoviscous length is the appropriate dimensionless parameter that controls the buckling behavior under any conditions.

7.2 Further simulations with defects

In Section 3.3, along with Fig. 3.5, we proposed that buckle packets behave as defects that can then transform into ridges. Further we proposed that ridges lower the energy compared

to wrinkles. A partial test of this was provided in Section 4.2.5. Here we will test this further by simulations.

As in Section 4.2.5, we created several "defects" by reducing the modulus of corresponding elements by 1% in the middle section of thin film. The distance between defects is close to interridge distance of Fig. 5.3. Then two simulations are conducted, one with $0.005s^{-1}$ compressive rate and one with $0.04s^{-1}$. The profile and normalized horizontal velocity are plotted below in Fig. 7.3. It is shown that the defects are "ignored" when compressive rate is high enough. On the other hand, the ridges will localized in the initial defects if compressive rate is low enough. This simulation strongly supports the idea that development of ridges vs wrinkles is driven entirely by kinetics. At sufficiently high rate, the pre-existing defects – even though they are at the spacing suitable for forming ridges – do not permit ridge development. In contrast at low rate, ridges can form.

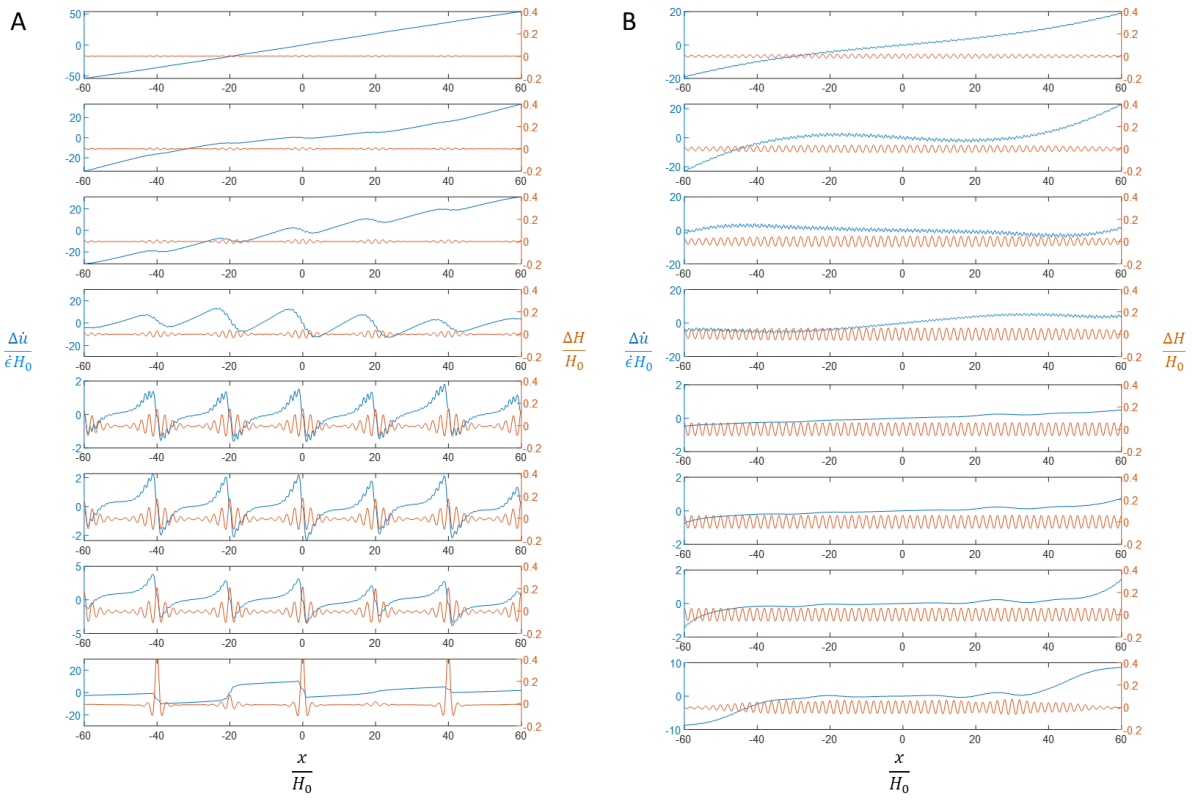

Figure 7.3: Evolution of profile and velocity. (A) $\dot{\epsilon} = 0.005s^{-1}$ (B) $\dot{\epsilon} = 0.04s^{-1}$. From top to bottom, strain is 0.03, 0.06, 0.09, 0.10, 0.12, 0.13, 0.14, 0.15.

A second application of defect simulations is to examine the quiescent evolution of buckles seen in section 4.2.5. We first apply a compressive strain of 0.05 all along the film by compression at a relatively high rate. This strain is lower than the critical strain for this film and hence the film is still flat at the end of the compression. Then we stop the compression and create several defects in the middle section of film by reducing modulus of film by 1%. As in Section 4.2.5, in one simulation, the distance between defects is set to be the wavelength of buckled film in Fig. 5.2A. In the second simulation, the distance between defects is set to be the wavelength of buckled film in Fig. 5.2B. As expected, the first simulation buckles into uniform wrinkles at the assigned wavelength and the second one into localized ridges at the assigned interridge spacing.

Different from all other simulations in this paper, this buckling occurs under quiescent conditions. The time-evolution of amplitude profile and normalized horizontal velocity profile of the two simulations are plotted below in Fig. 7.4.

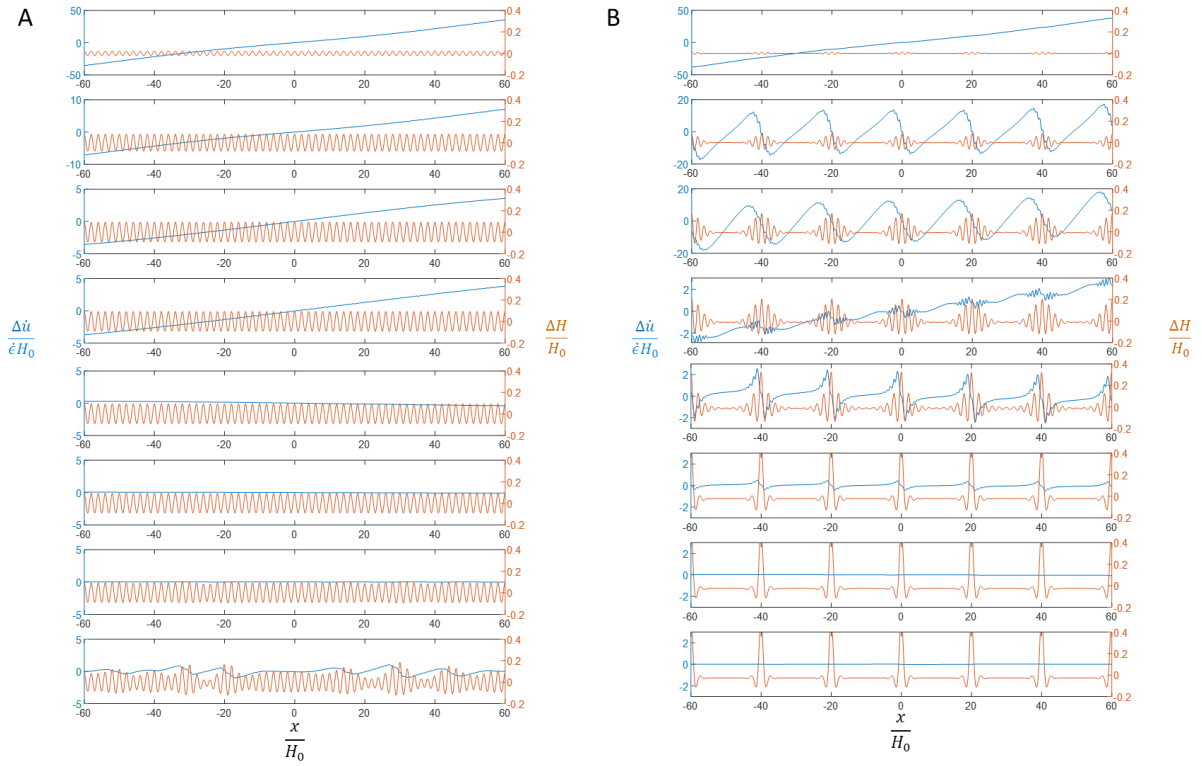

Figure 7.4: Evolution of profile and normalized horizontal velocity in 0.1, 0.2, 0.3, 0.5, 1.5, 3, 6, 9 second after buckling. (A) "Wrinkling" simulation (B) "localized ridge" simulation.

We now compare the film energy following the two pathways in in Fig. 7.5. The solid line is the total energy output by Abaqus. The dot-dash bending energy is calculated from integrating $\kappa^2 ds$ over middle one-third of the film length $\epsilon^2 ds$ following Eq. 4.11 and Eq. 4.12 As expected, the sum of these two agrees with the energy output by abaqus (solid line), lending confidence to the energy calculations. The vertical black lines are the timepoints at which the profiles were plotted in the previous two slides. During loading, the in-plane energy increases

quadratically as expected. After stopping, both simulations rapidly (within 0.3 seconds) reduce their total energy. This decrease comes because their in-plane strain energy reduces.

At the end of this rapid drop, the bending and in-plane energy are comparable to each other. Beyond this point, the energy in the wrinkling film reduces very gradually and the ridge-forming film however has a second significant decrease over the next 1-2 seconds. The physical picture therefore is that short-wavelength wrinkles appear at short times because they allow rapid decrease in energy. But wrinkles get arrested because the only way to reduce energy is through wrinkle coalescence, which is difficult (especially in a plane-strain simulation where there are no "Y-defects".).

The ridge mode offers the advantage of letting long segments of the film relax their in-plane strain to very low levels (although not zero). But developing ridges takes time, which is why short-wavelength wrinkles appear first. Though the relation of film energy and buckling behavior is roughly discussed in this section, more detailed simulations or experiments using this defect approach may be very fruitful to get a deeper understanding of "energy favorable" buckling mechanisms.

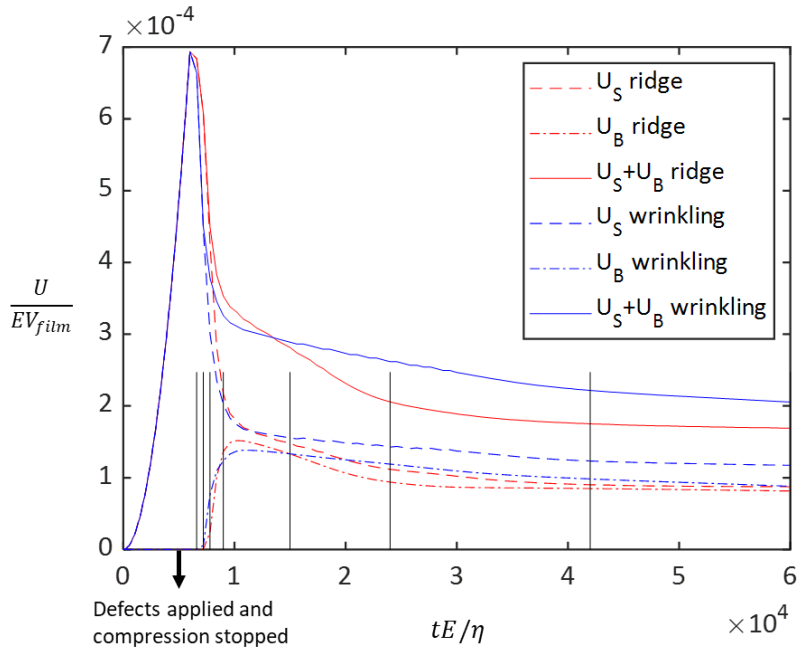

Figure 7.5: Film energy of wrinkling simulation and localized ridge simulation. The vertical solid lines are $t = 0.1, 0.2, 0.3, 0.5, 1.5, 3, 6, 9$ second after buckling

7.3 Improvement in creasing experiments

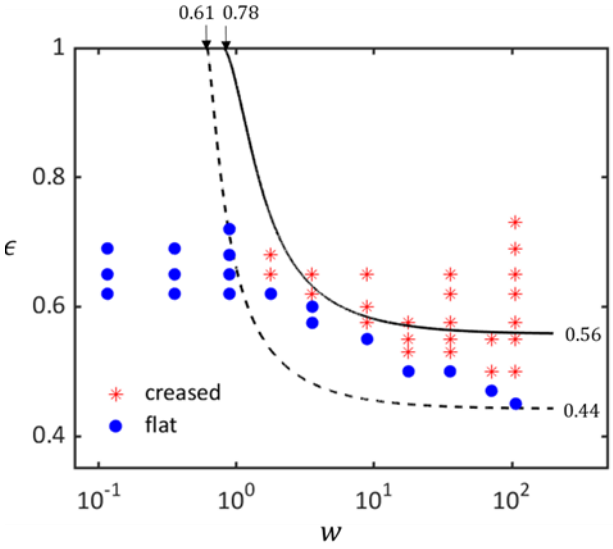

Figure 7.6: Map of viscoelastic creasing determined experimentally with theorical prediction.

The creasing research is based both on experiments and theoretical analysis. Fig 7.6 is the experimental result obtained using B15 as the viscoelastic liquid. The theoretical model is based on a single relaxation time whereas B15 has a broad spectrum of relaxation times. This set of experiments can be improved by using another viscoelastic liquid rather than B15. Thus, a more critical test of the theory could be done by selecting a fluid that has a much narrower distribution of relaxation times, e.g. a molten polymer with a narrow polydispersity. Further B15 has a smooth surface without defects. Another critical test of the theory would be to create defects by adding a small amount of particles into B15, and testing whether we the critical strain to approach the lower dashed line in Fig. 7.6.

Appendix A Advantages of using a high viscosity liquid

The experiments in this research used a fluid with much higher viscosity fluid than our previous experiments[10]. The reasons are as follows. Previously we showed[10] that with the lubrication assumption in the liquid layer, prior to buckling, the in-plane displacement of the film propagates diffusively through the film with a diffusivity given by $\frac{EhH_0}{\eta}$ where H_0 is the initial liquid layer thickness, h is the film thickness, E is the film modulus, and η is the liquid viscosity. The compression imposed by relaxation of the prestretched rubber appeared as a "source term" in the diffusion equation for the displacement, whereas the free ends served to relax the displacement. Upon solving the resulting diffusion equation, we showed that the compressive stress profile evolves from an initial zero stress (prior to the deformation) to a parabolic profile over a diffusion time-scale given by

$$\tau = \frac{4L^2}{\pi^2 h H_0}\frac{\eta(1-\nu^2)}{E} \tag{S1}$$

If not interrupted by buckling, the maximum strain of the parabolic profile would be

$$\epsilon_{f,max} = \frac{L^2}{2hH_0}\frac{\eta\dot{\epsilon}(1-\nu^2)}{E} = \frac{\pi^2}{8}\tau\dot{\epsilon} \tag{S2}$$

For the conditions used in our previous experiments[10], $\tau \sim 0.005\ s$ and $\epsilon_{max} \sim 10^{-3}$. Wrinkles were found to appear at times much longer than τ indicating that the wrinkles initiated from a strain state that was non-uniform. Further, due to the rapid relaxation from the film ends, only a few buckles appeared. Both these reasons make these experimental conditions undesirable: It would be better if the strain was uniform prior to buckling, and if the film were sufficiently long

that end-effects could be ignored. As apparent in the above equations, τ and ϵ_{max} can both be increased by changing various material and geometric parameters. Of all the parameters, η is the most convenient to induce significant changes in τ and ϵ_{max} since fluids with viscosities spanning several orders of magnitude are readily available.

The fluid in this research (see rheology in Fig. 6.2) has a viscosity that is about 1000-fold larger than our previous experiments, which offers numerous advantages. First, it proportionately increases τ and the maximum strain. Second, buckles appear at a time much shorter than τ suggesting that they appear from a more-or-less homogeneous strain state. Third, due to the much slower end-relaxation, there are typically over 25 wrinkles over the sample length, thus reducing end effects. Yet, even with this high viscosity, at the lowest rates or highest thicknesses used in our experiments, end relaxation may still play a role. Fourth, rates of all processes slow down. For instance, experiments which need high rate compression, and hence would need a high speed camera to resolve the development of folds. Further, the liquid can recede rapidly from the film edge. Increasing viscosity mitigates all these problems. Finally, the high viscosity allows the liquid to be coated in the form of a layer on a flat rubber strip without significant spreading due to gravity or surface tension effects. This was not possible previously and required an elastomeric tray.

A final advantage of a high viscosity of a liquid is that gravitational effects are negligible. To verify this, small cylinders of the B15 fluid, roughly 1-3 mm in diameter, were placed on the surface of a 0.25 mm thick layer of B15 and video-recorded over time. There was no visible sagging over 60 minutes. In fact, the folds are even smaller than these cylinders. Thus we conclude that gravity does not affect buckling behavior, neither during compression (where the longest experimental times are on the order of 250 s) or the quiescent evolution of buckles.

Appendix B Effect of sample width

Here we tackle the first key question listed in the Introduction: Does the width of the film play a role in fold localization? Some effects of sample width are associated with the edge, e.g. recession of the liquid. Other effects may be related to how the width compares with the other relevant dimensions such as film thickness, liquid thickness, and the wavelength.

Fig. S1 shows the results of experiments on films of various widths, all with a liquid layer thickness of H_0=0.38 mm, with each clamp moving at a speed of 1 mm/s, giving rates of roughly $\dot{\epsilon} = 0.011$ s^{-1}. These experiments were conducted in a different experimental jig which has translational clamps (whereas the jig used in the main text uses rotating drum clamps) and relatively low quality visualization. In cases Fig. S1A-D, the widths of the rubber strip and of the liquid layer are both ~11 mm, and hence the liquid extends far beyond the side-edge of the film (schematics on the right hand side in Fig. S1). In Fig. S1E&F, the film, liquid, and rubber all have approximately the same width.

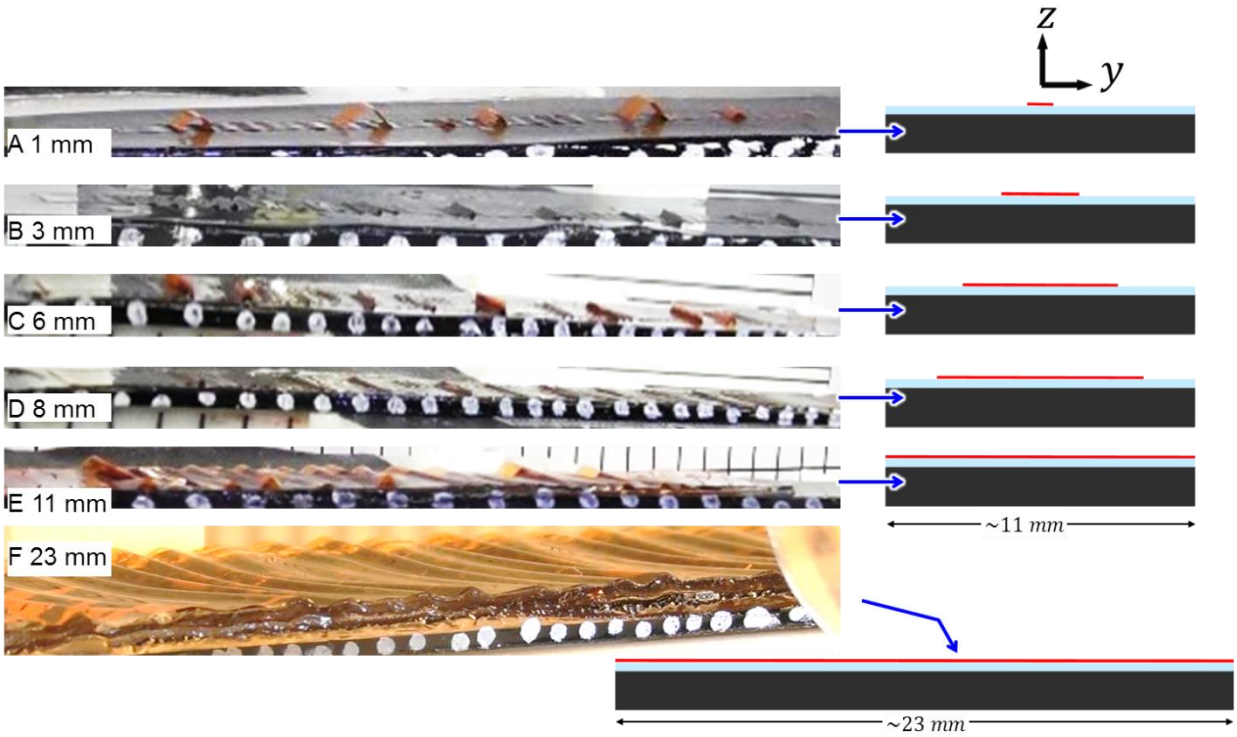

Figure. S1: Effect of film width on fold localization. In A-E, the relaxed rubber width is ~11 mm, and the film width is as noted in each figure. In F, the rubber strip and the film are both ~23 mm wide. The compression rates range from $\dot{\epsilon}$ =0.0104 s-1 to 0.012 s-1. The schematics to the right are approximately-to-scale views of the cross section indicating the relative widths of the rubber strip (black), the liquid layer (blue), and the film (red). These experiments were conducted with the help of two undergraduate students Anantha Sarma and Eshwar Hamesh in the Velankar research group.

Films of width 3 mm, 6 mm, and 8 mm (Fig. S1B,C,D) show qualitatively similar behavior: wrinkles develop at small strain, followed by fold localization. Most of the folds span the width of the film. For these film widths, a 2D view of buckling may be justified. The behavior at 1 mm width (Fig. S1A) is quite different: as the wrinkles grow in amplitude, the film delaminates off the liquid. This may be regarded as interfacial/adhesive failure at the film/liquid

interface. In fact, delamination was sometimes observed in wider films as well, and may be attributable to imperfections (e.g. a small blister between the film and the liquid layer at or near the film edge). Visually at least, this appears similar to the delamination from a winkled state for a film bonded to a soft solid substrate, although our substrate is a viscoelastic liquid. If the liquid has a much lower viscosity, Fig. S1B-F already showed that for narrow films, the liquid recedes and air invades under the peaks of the wrinkles. Although this can sometimes visually resemble delamination, it is not true delamination since there is no separation of the film from the liquid. Instead the liquid remains attached to the film (as well as to the rubber strip).

Both of these behaviors of narrow films have a common cause which can be understood as follows. The large curvature of a fold implies a large elastic energy penalty. One way to reduce this curvature is to simply widen the fold, but this requires increasing the volume under the fold. Delamination and fluid flow are the two ways whereby the surrounding medium (air in this case) can occupy the space under the folds, thus allowing them to become wider. For wide samples, both these mechanisms are slowed down, thus allowing the behavior to become nearly independent of width effects.

Fig. S1E shows a film width of ~11 mm, which is the same width as the rubber substrate and the liquid layer. In most such situations, the wrinkles and folds are more irregular, presumably because the film edge is now affected by imperfections at the side-edge of the liquid. Such imperfections are unavoidable with our sample fabrication procedure. Indeed at some locations, the film might even slightly overhang the liquid. Such samples often showed sets of folds with larger amplitude on opposite edges Fig. S2, rather than buckles that spanned the width of the sample. Clearly, a 2D view is not justified here.

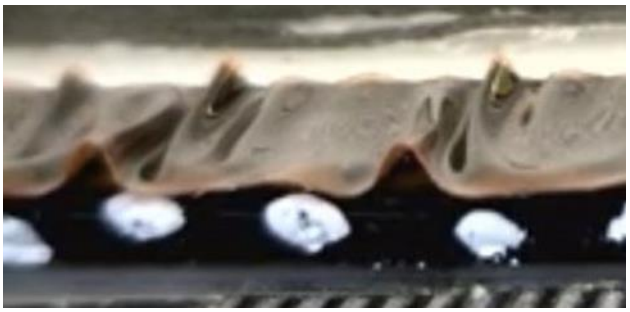

Figure. S2: Sets of folds with larger amplitude on opposite edges. In this case, the width of the film, the liquid layer, and the rubber, are all nearly equal.

Finally, Fig. S1F shows the width of ~23 mm, the widest samples examined in our research. Similar to Fig. S1E, the film, the liquid layer, and the rubber strip, all have approximately equal width. Fig. S1F shows that such wide samples curl around the compression direction. The reason for this is the Poisson effect: as the rubber strip retracts, its width increases. The film resists this width expansion (i.e. a tensile stress develops in the film along the width direction). The sample can resolve this width mismatch in at least two ways illustrated in Fig. S1. The first is via shear in the liquid layer (Fig. S1B), which allows the rubber width to increase, but the film width to remain the same. This is expected for relatively thick or stiff rubber films which resist bending. As per this mechanism, even if the film and the rubber have the same width at the beginning of the experiment, at the end of the experiment, the rubber would be wider. Such shear must also reduce the liquid thickness near the edge since some of the liquid that was covered by the film would end up outside of the film edge. The second is “curling” around the length direction (Fig. S1C), which would be expected if the rubber is relatively thin or soft. For narrow films, the shearing mechanism (Fig. S1B) can relieve the width mismatch almost completely and hence curling is not evident, whereas significant curling is evident in wide samples. Such curling

could be suppressed by conducting experiments with a thicker or stiffer rubber strip, although this would require a more robust stretching apparatus to handle larger tensile forces.

Even if curling can be suppressed completely, Poisson expansion of the rubber along the width direction necessarily induces width-direction tension in the film. Since tension can itself induce buckles in thin films, it is possible that for large sample widths, this film tension encourages buckling.

In summary, the effects of sample width are much more complex than recognized in our previous research. (1) For very narrow film widths, the edge allows at least two kinds of failure. One resembles true delamination off a solid substrate. Since this requires violating the no slip boundary condition at the film-liquid interface, we speculate that it is only possible if the liquid is viscoelastic, and may not appear if the fluid is truly Newtonian. In the second kind of failure, the liquid/air interface recedes inwards, thus allowing air to invade the space under the peaks of the buckles. (2) Very wide films show width-direction curling. (3) If curling is not visually evident, there must be width direction shear to accommodate the Poisson expansion of the rubber width. Such shear must induce variations in liquid thickness between the edge vs the rest of the film. (4) Poisson expansion must also induce width-direction tension in the film. (5) Finally, the sample edge may contribute imperfections that affect the buckling process. The experiments in the main text of this research use a film width of 8 mm, keeping the rubber and the B15 liquid both significantly wider. Since the liquid extends far beyond the film in all directions, this situation may be regarded as a strip of film floating on a sea of liquid. This width was chosen as a reasonable compromise between the above complexities. Further, this width is at least two-fold larger than the wrinkle wavelengths seen in all our research.

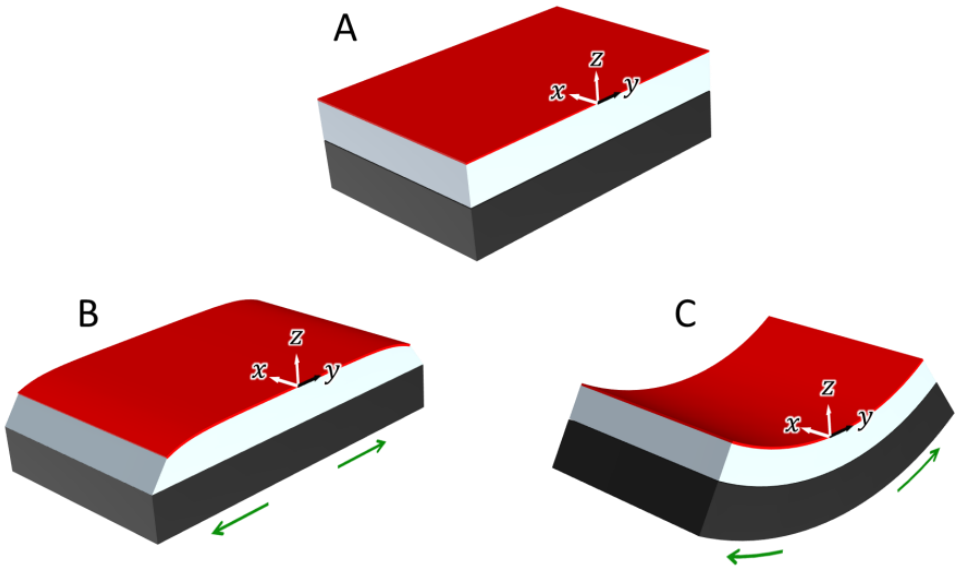

Figure. S3: Effect of Poisson expansion of the rubber strip along the width direction. A. Initial configuration wherein the black rubber layer has been stretched along the x-direction, whereas the red film is stress-free. B. Upon unstretching the rubber along the x direction, Poisson expansion along the y-direction (green arrows) is accommodated by shear. There is slight bending of the film near the edges. C. Upon unstretching the rubber, Poisson expansion along the y-direction (green arrows) is accommodated by bending around the x-axis.

Appendix C Additional information for Chapter 4

Figure. S4: Uniform wrinkles and localized ridges observed by Chatterjee et al[10]. An elastic polyester film rested on a liquid layer (molten polystyrene), which was itself coated onto a rubber strip. The rubber strip was released to induce wrinkles. The liquid polystyrene was cooled rapidly to vitrify it so that these buckled structures could be "frozen" before imaging. Figure reproduced from citation 50 with permission from the Royal Society of Chemistry.

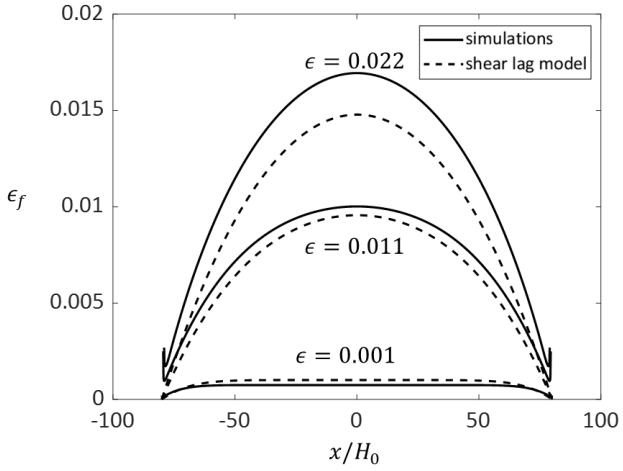

Figure. S5: Comparison with the film strain reported by simulations vs predictions from Eq. 4.2, the shear lag model for $L/H_0 = 80$.

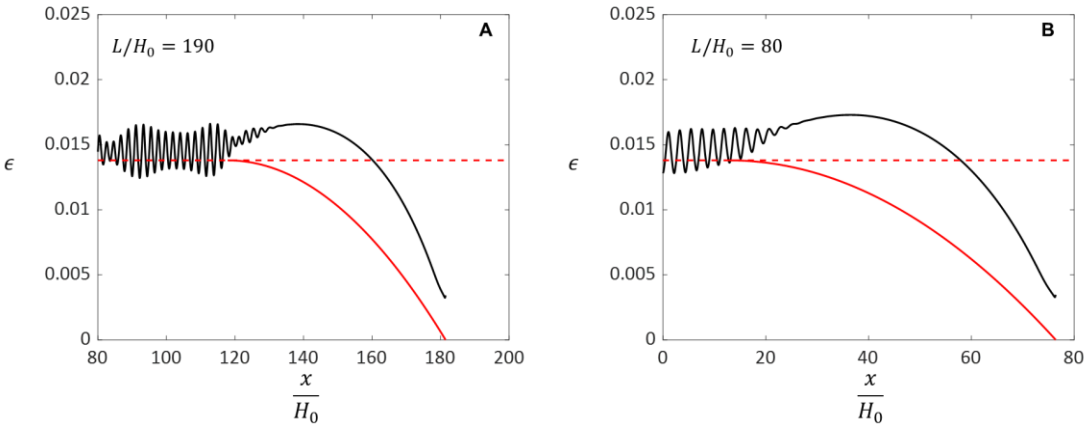

Figure. S6: Black curves are the strain profiles from simulations at a strain of $\epsilon = 0.05$. The L/H_0 values are mentioned at the top left. Dashed red lines is the value of $\langle \epsilon_{pb}^{f} \rangle$. Solid red line is prediction of Eq. 6, with using $L = L_{flat}$ as obtained from Eq. 4.7.

Appendix D Reproducibility for simulations from Chapter 5

Due to the large number of individual interridge distances, it is difficult to show multiple experiments on a single plot without crowding the points in Fig. 5.5A. Yet, such a reproducibility check is provided in Fig. S7.

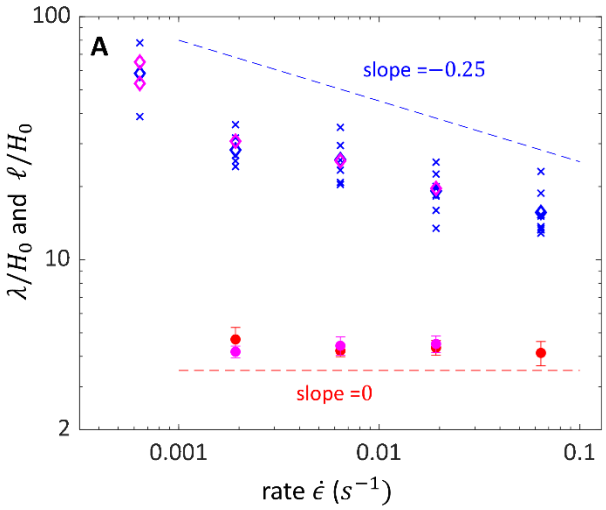

Figure. S7: The reproducibility check on the experimental data points on Fig. 5.5A.

Appendix E: Solving for the elastic portion of the deformation of the viscoelastic material

The following equation for $\mathbf{F_e}$ was derived in the main text:

$$\mathbf{F}_e\mathbf{F}_e^T - \mathbf{I} = \tau\left(\mathbf{F}_e\dot{\overline{\mathbf{F}_e^{-1}}}\mathbf{F}_e\mathbf{F}_e^T + \mathbf{F}_e\mathbf{F}_e^T\dot{\overline{\mathbf{F}_e^{-T}}}\mathbf{F}_e^T + \dot{\mathbf{F}}\mathbf{F}^{-1}\mathbf{F}_e\mathbf{F}_e^T + \mathbf{F}_e\mathbf{F}_e^T\mathbf{F}^{-T}\dot{\mathbf{F}}^T\right) \tag{S3}$$

where τ is the viscoelastic relaxation time of the material. Given the total deformation applied to the material $\mathbf{F}$, Eq. S3 can be solved to give $\mathbf{F}_e$ as follows.

The viscoelastic model is uniaxially compressed with a steady true strain rate r, so

$$\begin{bmatrix}\dot{x_1}\\ \dot{x_2}\\ \dot{x_3}\end{bmatrix} = \begin{bmatrix}\frac{1}{2}r & & \\ & \frac{1}{2}r & \\ & & -r\end{bmatrix}\begin{bmatrix}x_1\\ x_2\\ x_3\end{bmatrix} \tag{S4}$$

where the x_1, x_2, x_3 directions are defined by Fig. 5A in the main text.

Integrating Eq. S4:

$$\begin{bmatrix}x_1\\ x_2\\ x_3\end{bmatrix} = \begin{bmatrix}e^{rt/2} & & \\ & e^{rt/2} & \\ & & e^{-rt}\end{bmatrix}\begin{bmatrix}x_1'\\ x_2'\\ x_3'\end{bmatrix} \tag{S5}$$

where $x_i' = x_i(t=0)$. From this, $\boldsymbol{F}$ can be calculated:

$$\mathbf{F} = \begin{bmatrix}\lambda_1 & & \\ & \lambda_2 & \\ & & \lambda_3\end{bmatrix} = \begin{bmatrix}\frac{dx_1}{dx_1'} & \frac{dx_2}{dx_1'} & \frac{dx_3}{dx_1'}\\ \frac{dx_1}{dx_2'} & \frac{dx_2}{dx_2'} & \frac{dx_3}{dx_2'}\\ \frac{dx_1}{dx_3'} & \frac{dx_2}{dx_3'} & \frac{dx_3}{dx_3'}\end{bmatrix} = \begin{bmatrix}e^{rt/2} & 0 & 0\\ 0 & e^{rt/2} & 0\\ 0 & 0 & e^{-rt}\end{bmatrix} \tag{S6}$$

and

$$\dot{\mathbf{F}} = \begin{bmatrix} \dot{\lambda}_1 & & \\ & \dot{\lambda}_2 & \\ & & \dot{\lambda}_3 \end{bmatrix} = \begin{bmatrix} \frac{r}{2}e^{rt/2} & & \\ & \frac{r}{2}e^{rt/2} & \\ & & -re^{-rt} \end{bmatrix} \tag{S7}$$

Further, since $\mathbf{F}_e$ has no shear components, we assume the diagonal form:

$$\mathbf{F_e} = \begin{bmatrix} \lambda_{e1} & & \\ & \lambda_{e2} & \\ & & \lambda_{e3} \end{bmatrix} \tag{S8}$$

where $\lambda_{e1} = \lambda_{e2}$ because the deformation is uniaxial.

Combining Eqs. S1, S5, and S6 leads to two uncoupled first order differential equations:

$$\lambda_{e1}^2 - 1 = -2\tau\lambda_{e1}\dot{\lambda}_{e1} + r\tau\lambda_{e1}^2 \tag{S9}$$

$$\lambda_{e3}^2 - 1 = -2\tau\lambda_{e3}\dot{\lambda}_{e3} - 2r\tau\lambda_{e3}^2 \tag{S10}$$

These can be rearranged as:

$$\dot{\lambda}_{e1} = \frac{(1 - r\tau)\lambda_{e1}^2 - 1}{-2\tau\lambda_{e1}} \tag{S11}$$

$$\dot{\lambda}_{e3} = \frac{(1 + 2r\tau)\lambda_{e3}^2 - 1}{-2\tau\lambda_{e3}} \tag{S12}$$

Integrating Eqs. S9 and S10 with initial condition $\lambda_{e1}(t = 0) = \lambda_{e3}(t = 0) = 1$ we get:

$$\lambda_{e1} = \left(\frac{-r\tau e^{-t\left(\frac{1}{\tau} - r\right)} + 1}{1 - r\tau} \right)^{\frac{1}{2}} \tag{S13}$$

$$\lambda_{e3} = \left(\frac{2r\tau e^{-t\left(\frac{1}{\tau} + 2r\right)} + 1}{1 + 2r\tau} \right)^{\frac{1}{2}} \tag{S14}$$

Then λ_{e1} and λ_{e3} can be expressed in term of w and ϵ

$$\lambda_{e1} = \left(\frac{1 - w(1-\epsilon)^{\frac{1-w}{w}}}{1-w} \right)^{\frac{1}{2}} \tag{S15}$$

$$\lambda_{e3} = \left(\frac{1 + 2w(1-\epsilon)^{\frac{1+2w}{w}}}{1+2w} \right)^{\frac{1}{2}} \tag{S16}$$

where $w = r\tau$ is the Weissenberg number, and $\epsilon = 1 - \exp(-rt)$.

The criterion for viscoelastic creasing adopted in the main text is that creases appear when

$$\frac{\lambda_{e3}}{\lambda_{e1}} < \left(1 - \epsilon_{c,e}\right)^2 \tag{S17}$$

where the limiting values for $\epsilon_{c,e}$ are $\epsilon_{wrinkle}$ and ϵ_{crease}. Substituting Eq. S15 and S16 into Eq. S17, the creasing criterion is given explicitly as:

$$\left(\frac{1-w}{1+2w} \times \frac{1 + 2w(1-\epsilon)^{\frac{1+2w}{w}}}{1 - w(1-\epsilon)^{\frac{1-w}{w}}} \right)^{\frac{1}{2}} < \left(1 - \epsilon_{c,e}\right)^2 \tag{S18}$$

The strain at which Eq. S18 is first satisfied is taken as $\epsilon_{c,ve}$. The critical value, w_c, of Weissenberg number below which Eq. S18 cannot be satisfied can be obtained by letting strain approach 1 in Eq. S18 to obtain

$$\left.\frac{\lambda_{e3}}{\lambda_{e1}}\right|_{\epsilon \to 1} = \left(\frac{1-w_c}{1+2w_c} \right)^{1/2} < \left(1 - \epsilon_{c,e}\right)^2 \tag{S19}$$

The application of Eqs. S18 and S19 is illustrated in Fig. S5. The various curves in Fig. S5 correspond to the strain-evolution of the left hand side of Eq. S18 for a variety of w values. The dashed horizontal line corresponds to the right hand side of Eq. S18 with $\epsilon_{c,e} = \epsilon_{crease}$. With

this choice of $\epsilon_{c,e}$, Eq. S19 gives the $w_c = 0.605$ which is the critical Weissenberg number in the creasing limit. The dot-dashed red line in Fig. S5 shows the evolution of $\lambda_{e3}/\lambda_{e1}$ for this critical value. A similar diagram with $\epsilon_{c,e} = \epsilon_{wrinkle}$ (not shown) can illustrate the calculation of w_c in the wrinkle limit.

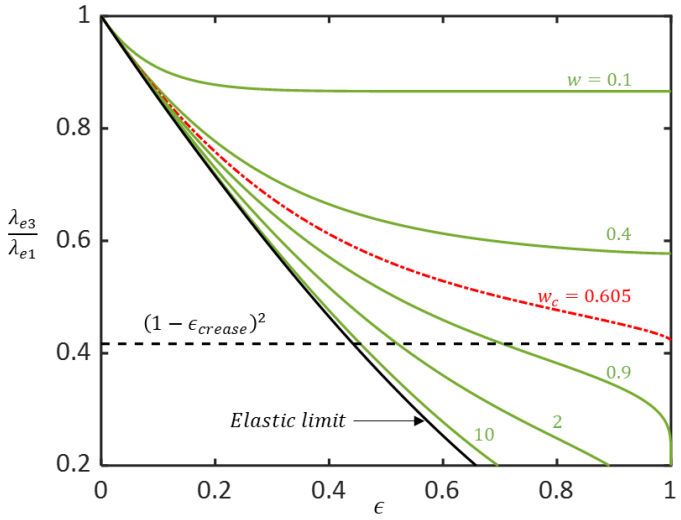

Figure. S8. A. The stretch ratio $\lambda_{e3}/\lambda_{e1}$ vs. strain ϵ at various Weissenberg numbers. The dashed black line indicates $(1-\epsilon_{crease})^2 = 0.42$. The intersection between each green line and the dashed black line gives the critical strain for creasing at the corresponding w value. No intersection is possible for $w < w_c$.

Appendix F: The equivalency of nonlinear viscoelastic model to the upper-convected Maxwell model relevant to Chapter 6

Define $\mathbf{B}_e = \mathbf{F}_e\mathbf{F}_e^T$, and note that $\boldsymbol{\nabla}\mathbf{v} = \dot{\mathbf{F}}\mathbf{F}^{-1}$. Accordingly, Eq. S3 becomes:

$$(\mathbf{B}_e - \mathbf{I}) = \tau\left(\mathbf{B}_e\dot{\overline{\mathbf{B}_e^{-1}}}\mathbf{B}_e + (\boldsymbol{\nabla}\mathbf{v})\mathbf{B}_e + \mathbf{B}_e(\boldsymbol{\nabla}\mathbf{v})^{\mathbf{T}}\right) \tag{S20}$$

Since $\mathbf{B}_e\mathbf{B}_e^{-1} = \mathbf{I}$, $\dot{\mathbf{B}}_e\mathbf{B}_e^{-1} = -\mathbf{B}_e\dot{\overline{\mathbf{B}_e^{-1}}}$, we have:

$$(\mathbf{B}_e - \mathbf{I}) = \tau\left(-\dot{\mathbf{B}}_e + (\boldsymbol{\nabla}\mathbf{v})\mathbf{B}_e + \mathbf{B}_e(\boldsymbol{\nabla}\mathbf{v})^{\mathbf{T}}\right) \tag{S21}$$

Use $\boldsymbol{\tau}_e = NkT(\mathbf{B}_e - \mathbf{I})$ to cancel out $\mathbf{B}_e$

$$\boldsymbol{\tau}_e = \tau\left(-\dot{\boldsymbol{\tau}}_e + (\boldsymbol{\nabla}\mathbf{v})\boldsymbol{\tau}_e + \boldsymbol{\tau}_e(\boldsymbol{\nabla}\mathbf{v})^{\mathbf{T}}\right) + NkT\tau\left((\boldsymbol{\nabla}\mathbf{v}) + (\boldsymbol{\nabla}\mathbf{v})^{\mathbf{T}}\right) \tag{S22}$$

Rearranging terms gives the common form of the upper convected Maxwell model:

$$\boldsymbol{\tau}_e + \tau\left(\dot{\boldsymbol{\tau}}_e - (\boldsymbol{\nabla}\mathbf{v})\boldsymbol{\tau}_e - \boldsymbol{\tau}_e(\boldsymbol{\nabla}\mathbf{v})^{\mathbf{T}}\right) = NkT\tau\left((\boldsymbol{\nabla}\mathbf{v}) + (\boldsymbol{\nabla}\mathbf{v})^{\mathbf{T}}\right) \tag{S23}$$

Bibliography

(1) Park, S. K.; Gao, X. L. Bernoulli–Euler beam model based on a modified couple stress theory. *Journal of Micromechanics and Microengineering* **2006**, *16*, 2355-2359.

(2) <IntroductionToAbaqus-ILT-Lectures-Abq614.pdf>.

(3) Liang, J.; Huang, R.; Yin, H.; Sturm, J.; Hobart, K.; Suo, Z. Relaxation of compressed elastic islands on a viscous layer. *Acta Materialia* **2002**, *50*, 2933-2944.

(4) Huang, R.; Im, S. H. Dynamics of wrinkle growth and coarsening in stressed thin films. *Physical Review E - Statistical, Nonlinear, and Soft Matter Physics* **2006**, *74*, 026214.

(5) Brau, F.; Vandeparre, H.; Sabbah, A.; Poulard, C.; Boudaoud, A.; Damman, P. Multiple-length-scale elastic instability mimics parametric resonance of nonlinear oscillators. *Nature Physics* **2011**, *7*, 56-60.

(6) Cao, Y.; Hutchinson, J. W. Wrinkling Phenomena in Neo-Hookean Film/Substrate Bilayers. *Journal of Applied Mechanics-Transactions of the Asme* **2012**, *79*.

(7) Brau, F.; Damman, P.; Diamant, H.; Witten, T. A. Wrinkle to fold transition: influence of the substrate response. *Soft Matter* **2013**, *9*, 8177-8186.

(8) Takei, A.; Jin, L.; Hutchinson, J. W.; Fujita, H. Ridge Localizations and Networks in Thin Films Compressed by the Incremental Release of a Large Equi-biaxial Pre-stretch in the Substrate. *Advanced Materials* **2014**, *26*, 4061-4067.

(9) Ebata, Y.; Croll, A. B.; Crosby, A. J. Wrinkling and strain localizations in polymer thin films. *Soft Matter* **2012**.

(10) Chatterjee, S.; McDonald, C.; Niu, J.; Velankar, S. S.; Wang, P.; Huang, R. Wrinkling and folding of thin films by viscous stress. *Soft Matter* **2015**, *11*, 1814-1827.

(11) Holmes, D. P.; Crosby, A. J. Draping Films: A Wrinkle to Fold Transition. *Physical Review Letters* **2010**, *105*, 038303.

(12) Paulsen, J. D.; Hohlfeld, E.; King, H.; Huang, J. S.; Qiu, Z. L.; Russell, T. P.; Menon, N.; Vella, D.; Davidovitch, B. Curvature-induced stiffness and the spatial variation of wavelength in wrinkled sheets. *Proceedings of the National Academy of Sciences of the United States of America* **2016**, *113*, 1144-1149.

(13) Paulsen, J. D.; Demery, V.; Toga, K. B.; Qiu, Z. L.; Russell, T. P.; Davidovitch, B.; Menon, N. Geometry-Driven Folding of a Floating Annular Sheet. *Physical Review Letters* **2017**, *118*.

(14) King, H.; Schroll, R. D.; Davidovitch, B.; Menon, N. Elastic sheet on a liquid drop reveals wrinkling and crumpling as distinct symmetry-breaking instabilities. *Proceedings of the National Academy of Sciences of the United States of America* **2012**, *109*, 9716-9720.

(15) Timounay, Y.; De, R.; Stelzel, J. L.; Schrecengost, Z. S.; Ripp, M. M.; Paulsen, J. D. Crumples as a Generic Stress-Focusing Instability in Confined Sheets. *Physical Review X* **2020**, *10*.

(16) Wang, Q.; Zhao, X. Phase Diagrams of Instabilities in Compressed Film-Substrate Systems. *Journal of Applied Mechanics-Transactions of the Asme* **2014**, *81*.

(17) Gent, A.; Cho, I. Surface instabilities in compressed or bent rubber blocks. *Rubber Chemistry and Technology* **1999**, *72*, 253-262.

(18) Chen, D.; Cai, S.; Suo, Z.; Hayward, R. C. Surface energy as a barrier to creasing of elastomer films: an elastic analogy to classical nucleation. *Phys Rev Lett* **2012**, *109*, 038001.

(19) Cai, S. Q.; Chen, D. Y.; Suo, Z. G.; Hayward, R. C. Creasing instability of elastomer films. *Soft Matter* **2012**, *8*, 1301-1304.

(20) Yoon, J.; Kim, J.; Hayward, R. C. Nucleation, growth, and hysteresis of surface creases on swelled polymer gels. *Soft Matter* **2010**, *6*.

(21) Liu, Q.; Ouchi, T.; Jin, L.; Hayward, R.; Suo, Z. Elastocapillary Crease. *Phys Rev Lett* **2019**, *122*, 098003.

(22) Trujillo, V.; Kim, J.; Hayward, R. C. Creasing instability of surface-attached hydrogels. *Soft Matter* **2008**, *4*.

(23) Mora, S.; Abkarian, M.; Tabuteau, H.; Pomeau, Y. Surface instability of soft solids under strain. *Soft Matter* **2011**, *7*, 10612-10619.

(24) Yang, J.; Illeperuma, W.; Suo, Z. Inelasticity increases the critical strain for the onset of creases on hydrogels. *Extreme Mech Lett* **2020**, *40*, 100966.

(25) Tallinen, T.; Biggins, J. S.; Mahadevan, L. Surface Sulci in Squeezed Soft Solids. *Physical Review Letters* **2013**, *110*, 024302.

(26) Li, J.; Arora, N.; Rudykh, S. Elastic instabilities, microstructure transformations, and pattern formations in soft materials. *Current Opinion in Solid State and Materials Science* **2021**, *25*, 100898.

(27) Chen, D.; McKinley, G. H.; Cohen, R. E. Spontaneous wettability patterning via creasing instability. *Proc Natl Acad Sci U S A* **2016**, *113*, 8087-8092.

(28) Brau, F.; Damman, P.; Diamant, H.; Witten, T. A. Wrinkle to fold transition: influence of the substrate response. *Soft Matter* **2013**, *9*.

(29) Timounay, Y.; De, R.; Stelzel, J. L.; Schrecengost, Z. S.; Ripp, M. M.; Paulsen, J. D. Crumples as a generic stress-focusing instability in confined sheets. *Physical Review X* **2020**, *10*, 021008.

(30) Ebata, Y.; Croll, A. B.; Crosby, A. J. Wrinkling and strain localizations in polymer thin films. *Soft Matter* **2012**, 9086-9091.

(31) Velankar, S. S.; Lai, V.; Vaia, R. A. Swelling-induced delamination causes folding of surface-tethered polymer gels. *ACS Appl Mater Interfaces* **2012**, *4*, 24-29.

(32) Brau, F.; Vandeparre, H.; Sabbah, A.; Poulard, C.; Boudaoud, A.; Damman, P. Multiple-length-scale elastic instability mimics parametric resonance of nonlinear oscillators. *Nature Physics* **2010**, *7*, 56-60.

(33) Biot, M. A. Surface instability of rubber in compression. *Applied Scientific Research, Section A* **1963**, *12*, 168-182.

(34) Pocivavsek, L.; Dellsy, R.; Kern, A.; Johnson, S.; Lin, B.; Lee, K. Y. C.; Cerda, E. Stress and fold localization in thin elastic membranes. *Science* **2008**, *320*, 912-916.

(35) Rivetti, M. Non-symmetric localized fold of a floating sheet. *Comptes rendus mécanique* **2013**, *341*, 333-338.

(36) Takei, A.; Jin, L.; Hutchinson, J. W.; Fujita, H. Ridge localizations and networks in thin films compressed by the incremental release of a large equi-biaxial pre-stretch in the substrate. *Advanced Materials* **2014**, *26*, 4061-4067.

(37) Démery, V.; Davidovitch, B.; Santangelo, C. D. Mechanics of large folds in thin interfacial films. *Physical Review E* **2014**, *90*, 042401.

(38) Jin, L.; Auguste, A.; Hayward, R. C.; Suo, Z. Bifurcation Diagrams for the Formation of Wrinkles or Creases in Soft Bilayers. *Journal of Applied Mechanics* **2015**, *82*.

(39) Oshri, O.; Brau, F.; Diamant, H. Wrinkles and folds in a fluid-supported sheet of finite size. *Physical Review E* **2015**, *91*, 052408.

(40) Jambon-Puillet, E.; Vella, D.; Protière, S. The compression of a heavy floating elastic film. *Soft matter* **2016**, *12*, 9289-9296.

(41) du Roure, O.; Lindner, A.; Nazockdast, E. N.; Shelley, M. J. Dynamics of Flexible Fibers in Viscous Flows and Fluids. *Annual Review of Fluid Mechanics* **2019**, *51*, 539-572.

(42) Diamant, H.; Witten, T. A. Compression induced folding of a sheet: An integrable system. *Physical Review Letters* **2011**, *107*, 164302.

(43) Huang, J.; Davidovitch, B.; Santangelo, C. D.; Russell, T. P.; Menon, N. Smooth cascade of wrinkles at the edge of a floating elastic film. *Physical Review Letters* **2010**, *105*, 038302.

(44) Cao, Y.; Hutchinson, J. W. Wrinkling Phenomena in Neo-Hookean Film/Substrate Bilayers. *Journal of Applied Mechanics* **2012**, *79*, 031019.

(45) Auguste, A.; Jin, L.; Suo, Z.; Hayward, R. C. The role of substrate pre-stretch in post-wrinkling bifurcations. *Soft Matter* **2014**, *10*, 6520-6529.

(46) Demery, V.; Davidovitch, B.; Santangelo, C. D. Mechanics of large folds in thin interfacial films. *Physical Review E* **2014**, *90*.

(47) Huang, J.; Juszkiewicz, M.; De Jeu, W. H.; Cerda, E.; Emrick, T.; Menon, N.; Russell, T. P. Capillary wrinkling of floating thin polymer films. *Science* **2007**, *317*, 650-653.

(48) Cao, Y.; Hutchinson, J. W. Wrinkling Phenomena in Neo-Hookean Film/Substrate Bilayers. *Journal of Applied Mechanics* **2012**, *79*.

(49) Wang, Q.; Zhao, X. Phase Diagrams of Instabilities in Compressed Film-Substrate Systems. *Journal Applied Mechanics* **2014**, *81*, 0510041-5100410.

(50) Sridhar, N.; Srolovitz, D. J.; Suo, Z. Kinetics of buckling of a compressed film on a viscous substrate. *Applied Physics Letters* **2001**, *78*, 2482-2484.

(51) Chatterjee, S.; McDonald, C.; Niu, J.; Velankar, S. S.; Wang, P.; Huang, R. Wrinkling and folding of thin films by viscous stress. *Soft Matter* **2015**, *11*, 1814-1827.

(52) Yu, S. J.; Chen, M. G.; Zhang, Y. J.; Zhou, H.; Si, P. Z. An experimental study of the influence of film edges and imperfections on buckling morphologies of quenched iron films. *Thin Solid Films* **2011**, *519*, 7936-7939.

(53) Moon, M. W.; Jensen, H. M.; Hutchinson, J. W.; Oh, K. H.; Evans, A. G. The characterization of telephone cord buckling of compressed thin films on substrates. *Journal of the Mechanics and Physics of Solids* **2002**, *50*, 2355-2377.

(54) Tomotika, S. On the instability of a cylindrical thread of a viscous liquid surrounded by another viscous fluid. *Proceedings of the Royal Society of London* **1935**, 322-337.

(55) Haskell, R. W. Introduction to thermodynamics of spinodal decomposition. *Journal of the American Ceramic Society* **1973**, *56*, 355-360.

(56) Vrij, A. Possible mechanism for spontaneous rupture of thin free liquid films. *Discussions of the Faraday Society* **1966**, 23-&.

(57) Jiang, H. Q.; Zhang, J. P. Mechanics of Microtubule Buckling Supported by Cytoplasm. *Journal of Applied Mechanics-Transactions of the Asme* **2008**, *75*, 061019

(58) Huang, R.; Suo, Z. Instability of a compressed elastic film on a viscous layer. *International Journal of Solids and Structures* **2002**, *39*, 1791-1802.

(59) Liang, J.; Huang, R.; Yin, H.; Sturm, J. C.; Hobart, K. D.; Suo, Z. Relaxation of compressed elastic islands on a viscous layer. *Acta Materialia* **2002**, *50*, 2933-2944.

(60) Leal, L. G.: Chapter 5: The Thin-Gap Approximation – Lubrication Problems. In *Advanced Transport Phenomena*; Cambridge University Press: Cambridge, 2007.

(61) Jiang, H.; Khang, D.-Y.; Song, J.; Sun, Y.; Huang, Y.; Rogers, J. A. Finite deformation mechanics in buckled thin films on compliant supports. *Proceedings of the National Academy of Sciences* **2007**, *104*, 15607-15612.

(62) Cerda, E.; Mahadevan, L. Geometry and physics of wrinkling. *Phys Rev Lett* **2003**, *90*, 074302.

(63) Ma, Y.; Xue, Y.; Jang, K.-I.; Feng, X.; Rogers, J. A.; Huang, Y. Wrinkling of a stiff thin film bonded to a pre-strained, compliant substrate with finite thickness. *Proceedings of the Royal Society A: Mathematical, Physical and Engineering Sciences* **2016**, *472*, 20160339.

(64) Bowden, N.; Brittain, S.; Evans, A. G.; Hutchinson, J. W.; Whitesides, G. M. Spontaneous formation of ordered structures in thin films of metals supported on an elastomeric polymer. *Nature* **1998**, *393*, 146-149.

(65) Auguste, A.; Yang, J.; Jin, L.; Chen, D.; Suo, Z.; Hayward, R. C. Formation of high aspect ratio wrinkles and ridges on elastic bilayers with small thickness contrast. *Soft Matter* **2018**, *14*, 8545-8551.

(66) Cao, Y.; Hutchinson, J. W. From wrinkles to creases in elastomers: the instability and imperfection-sensitivity of wrinkling. *Proceedings of the Royal Society A: Mathematical, Physical and Engineering Sciences* **2012**, *468*, 94-115.

(67) Guan, X.; Sarma, A.; Hamesh, E.; Yang, J.; Nguyen, N.; Cerda, E.; Pocivavsek, L.; Velankar, S. S. Compression-induced buckling of thin films bonded to viscous substrates: Uniform wrinkles vs localized ridges (Submitted). *Int J Solids Struct* **2022**.

(68) Guan, X.; Nguyen, N.; Cerda, E.; Pocivavsek, L.; Velankar, S. S. Dynamics of wrinkling, ridge localization, and end relaxation of thin films bonded to viscous substrates (To be submitted to International Journal of Solids and Structures). **2022**.

(69) Hong, W.; Zhao, X.; Suo, Z. Formation of creases on the surfaces of elastomers and gels. *Applied Physics Letters* **2009**, *95*, 111901.

(70) Hohlfeld, E.; Mahadevan, L. Unfolding the Sulcus. *Physical Review Letters* **2011**, *106*, 105702.

(71) Kang, M. K.; Huang, R. Swell-induced surface instability of confined hydrogel layers on substrates. *Journal of the Mechanics and Physics of Solids* **2010**, *58*, 1582-1598.

(72) Diab, M.; Zhang, T.; Zhao, R.; Gao, H.; Kim, K.-S. Ruga mechanics of creasing: from instantaneous to setback creases. *Proceedings of the Royal Society A: Mathematical, Physical and Engineering Sciences* **2013**, *469*, 20120753.

(73) Wu, Z.; Bouklas, N.; Huang, R. Swell-induced surface instability of hydrogel layers with material properties varying in thickness direction. *Int J Solids Struct* **2013**, *50*, 578–587.

(74) Jin, L. H.; Suo, Z. G. Smoothening creases on surfaces of strain-stiffening materials. *Journal of the Mechanics and Physics of Solids* **2015**, *74*, 68-79.

(75) Stewart, P. S.; Waters, S. L.; El Sayed, T.; Vella, D.; Goriely, A. Wrinkling, creasing, and folding in fiber-reinforced soft tissues. *Extreme Mech Lett* **2016**, *8*, 22-29.

(76) Yang, S.; Chen, Y.-c. Wrinkle surface instability of an inhomogeneous elastic block with graded stiffness. *Proceedings of the Royal Society A: Mathematical, Physical and Engineering Sciences* **2017**, *473*, 20160882.

(77) Karpitschka, S.; Eggers, J.; Pandey, A.; Snoeijer, J. H. Cusp-Shaped Elastic Creases and Furrows. *Physical Review Letters* **2017**, *119*, 198001.

(78) Tang, S.; Gao, B.; Zhou, Z.; Gu, Q.; Guo, T. Dimension-controlled formation of crease patterns on soft solids. *Soft Matter* **2017**, *13*, 619-626.

(79) Ciarletta, P. Matched asymptotic solution for crease nucleation in soft solids. *Nature Communications* **2018**, *9*, 496.

(80) Huang, J.; Yang, J.; Jin, L.; Clarke, D. R.; Suo, Z. Pattern formation in plastic liquid films on elastomers by ratcheting. *Soft Matter* **2016**, *12*, 3820-3827.

(81) J. Brandrup, E. I., EA Grulke, A. Abe, and DR Bloch: Polymer Handbook. John Wiley & Sons, New York, 2005.

(82) Macosko, C. Rheology principles, measurements, and applications, VCH Publ. *Inc, New York* **1994**.

(83) Rubinstein, M.; Colby, R. H.: *Polymer physics*; Oxford university press New York, 2003; Vol. 23.

(84) Gurtin, M. E.; Fried, E.; Anand, L. In *Tilte*2010.